Department of Precision and Microsystems Engineering

Robotic Metamaterial with Odd Elasticity:
Design and testing of a Metamaterial with novel actuation and control method.

Rutger Naber

Report no	: 2022.033
Coach	: Jonas Veenstra Andres Hunt
Professor	: Hassan Hossein Nia Kani Corentin Coulais
Specialisation	: Mechatronic System Design
Type of report	: Thesis
Date	: July 25th, 2022

Contents

List of Figures

List of Tables

1

Introduction

Going beyond naturally occurring materials, Metamaterials exploit a design at the microscale resulting in macroscopic behaviour, to achieve different or even new properties that can have a wide range of applications. By incorporating sensors, actuators and control, Robotic Metamaterials can achieve even more extremely different behaviour such as odd elasticity. In this work, a new unit cell for a robotic metamaterial that achieves odd elasticity is designed, manufactured, and finally tested. This thesis report is divided into 3 main segments.

In Part I, an extensive literature review is done starting with chapter 2, to find out why research into odd elastic metamaterials is relevant. In chapter 3, the state of the art is analysed, to define the improvement scope for a newly designed unit cell. After the research goal is formulated, a further literature review is done in order to find solutions and manufacturing methods for the components of the unit cell. Before continuing to the design process, Chapter 7, concludes the literature review and summarizes the chosen concept.

Part II describes the process of converting this concept choice into a unit cell design consisting of the Mechanism (Chapter 8, an Actuator (Chapter 9) and a control system (Chapter 10). The performance of of these components is validated in chapter 11.

After the validation, experimental data was gathered to characterise the behaviour of the new unit cell in Part III. In this chapter, the limit cycle behaviour of a single unit cell is analysed (chapter 12) as well as the ability of the unit cell to locomote (Chapter 13). Finally, a lattice consisting of multiple lattices was built and characterised in chapter 14.

This report is the result of my thesis project that I have been working on for the past year. I would like to thank the following people: Hassan Hossein Nia Kani and Andres Hunt from the TU Delft and Corentin Coulais from the University of Amsterdam for their supervision during the year. Jonas Veenstra for his incredible support as a daily supervisor, without whom this work would not have been possible. Many thanks to Tjeerd Weijers, Kasper van Nieuwland and Daan Giesen and all other members of the Technology Centre of the University of Amsterdam for the technical advice and assistance. Finally, I would like to thank Laura, my family and friends for their support during my thesis and all years at TU Delft.

Part I

Literature study

2

Motivation

Naturally occurring materials are used in all fields of technology to create tools and they are selected for their properties. Aluminium is light and stiff, which is perfect for a bike, while glass can refract light and has a high hardness and is therefore perfect for a pair of glasses. Next to naturally occurring materials, a new class of materials has emerged: Metamaterials.
Metamaterials are materials that are exploiting a design at a micro-scale resulting in macroscopic behaviour and achieve properties that are different and usually more complex than the sum of bulk material parts. These metamaterials consist of structured patterns of unit cells. Already at the start of this century, metamaterials have demonstrated their functionalities in the fields of optics [1], acoustics [2] and thermal [3] fields, leading to new applications such as perfect lenses [4].
In more recent times, mechanical metamaterials have gained traction. These mechanical can have attributes such as negative-valued properties, unique dynamic responses, topological polarisation and non-reciprocity. An example of such a negative-valued property is for instance the work of Chen and Zhen, who proposed a metamaterial with a spatial varying Poisson's ratio between 0 and -7 [5].
In this thesis project, the focus will be on designing a metamaterial with the property "Odd elasticity", which is a material behaviour where there is linear conservation of momentum, but exhibit a non-reciprocal linear response, such as breaking the conservation of energy in angular momentum [6]. This can be achieved through non-reciprocal couplings, such as odd springs. In the coming sections, odd elasticity, metamaterials and the developments in their research field will be explained.

2.1. Non-reciprocity

Reciprocity is the physical principle that ensures that transmission between any two points in space is the same for opposite propagation directions, regardless of geometrical or material asymmetries. For instance, when person A gives a birthday gift to person B, he expects to receive one back on his birthday. In physics, this reciprocal behaviour is also explained by Newton's 3rd law stating that for each action there is an equal reaction in the exact opposing direction. Reciprocity is very important for many systems to function, but it can be advantageous to break this reciprocity (Non-reciprocity) for signal transmission, isolation and other functionality [7]. Non-reciprocity, in this case, would mean that person A keeps giving a gift on the birthday of person B, but never receives a gift back.
Although originally, breaking reciprocity was more commonly used in electromagnetic systems [8], it has recently started to be investigated by many more fields such as Optics [9], [10], Acoustics [11], [12] and Mechanics [13]–[15]. The possibility of having non-reciprocal behaviour in those fields can help develop devices or materials that can store, guide or dampen information or energy. This behaviour can be achieved with passive (Here no energy is added or removed) systems by making use of broken spatial inversion symmetry and nonlinearities, [15], [16] as well as with active (Here energy is added or removed through for instance actuation) systems that break time-reversal symmetry [12]. While both methods have resulted in strong non-reciprocal behaviour, they are only working in narrow frequency or magnitude ranges.
Solving the issue of a narrow working bandwidth, Brandenbourger et al. have created a robotic meta-

material that uses active control to break reciprocity [13], [17]. This is achieved by designing building blocks that use local sensing, communication, computation and actuation. These building blocks are mechanically coupled and communicate with their direct neighbours. Passive stiffness and active control are combined to result in unique asymmetric modes at all frequencies and large magnitudes, creating self-amplified and non-reciprocal mechanical wave transmission [13].

2.1.1. Odd spring

While the passive stiffness in the system from Brandenbourger et al. works like a normal spring, which is reciprocal and does not care from which side or direction it is compressed, the active control works as an odd spring. This odd spring uses a non-reciprocal coupling as shown in equation 2.1, where κ^a is the stiffness in N/m. Figure 2.1 shows that this odd spring results in a different response when pushed from point 1 in point 2, then when pushed at point 2 in point 1.

$$\tau_1^a = \kappa^a \delta\theta_2 \text{ and } \tau_2^a = -\kappa^a \delta\theta_1 \tag{2.1}$$

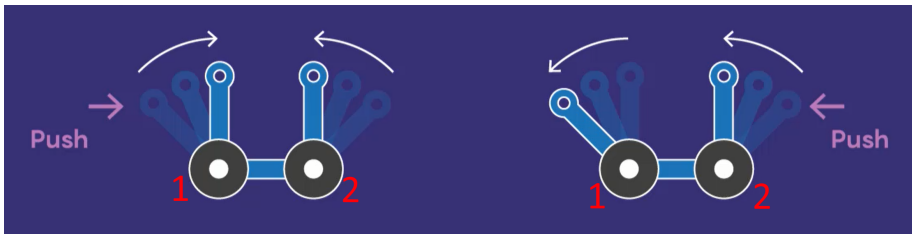

Figure 2.1: Schematic of a basic model consisting of two building blocks, showing the non-reciprocal response. [18]

2.1.2. Odd elasticity

For a material consisting of these odd springs, there is no longer a symmetric elastic response from the material and therefore additional terms are required to describe the relation between stress and displacement. For a 2D elastic material, the displacement gradients can be described with 4 modes: Dilation, rotation and shear modes S1 and S2, which are shown in figure 2.3. For a linear isotropic elastic material, only bulk modulus B and shear modulus μ are needed to describe these gradients. However, for an odd elastic material, two additional moduli are required to describe the full behaviour [6]. Firstly A is introduced to describe the coupling between compression and an internal torque density and secondly, K^0 leads to an asymmetrical coupling of internal shear modes.

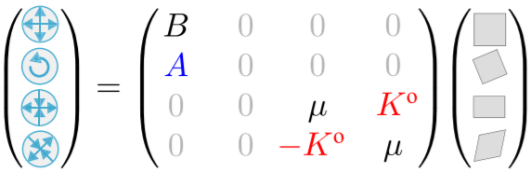

Figure 2.2: Generalized linear relation between stress and displacement for a 2D Odd elastic solid ($\sigma = K * \epsilon$) [6]

For a linear isotropic elastic material, the Young's modulus describes the relation between stress and strain in lengthwise direction: $E = \frac{d\sigma_{yy}}{du_{yy}}$ and the Poisson's ratio expresses the relation between this lengthwise deformation and the deformation perpendicular to this: $\upsilon = -\frac{du_{yy}}{du_{xx}}$.

Similarly, the bulk properties of an odd elastic material can be described. In the work of Brandenbourger et al. the odd modulus K^0 is calculated with $K^0 = \frac{d\sigma_{xy}}{du_{yy}}$, which is the amount of shear caused by a compression in direction y [17]. Additionally, parameter V^0 is used to describe the odd ratio, which is calculated with $V^0 = -\frac{du_{xy}}{du_{yy}}$, comparing the deformation in shear to the deformation in compression.

Here, the magnitude of this odd ratio describes how significant the odd elastic response is, while the sign describes the direction of this response.

2.1.3. Limit cycles

Dimensionless parameter ξ, as shown in equation 12.2, describes the ratio between the drive (k_a and Inertia (I), to the dissipation ( ) and restoring forces (k). When $|\xi| < 1$, the dissipation and restoring forces are too big and any oscillation will terminate. When $|\xi| > 1$ the system becomes unstable and for a linear system, an oscillation would start and grow infinitely large until the system would explode. However, for a non-linear system, some things could instead limit this oscillation to a finite amplitude such as non-linear stiffness, actuator saturation or even mechanical end stops. Figure **??** shows the response of the system shown in figure 2.1 for both cases of ξ. This cycle that is limited due to a non-linearity in the system is called the limit cycle. A limit cycle is a strictly non-linear behaviour that can not be explained with linear theory and is characterised by a constant amplitude and frequency.

$$\xi = k_a/\Gamma\sqrt{I/k} \tag{2.2}$$

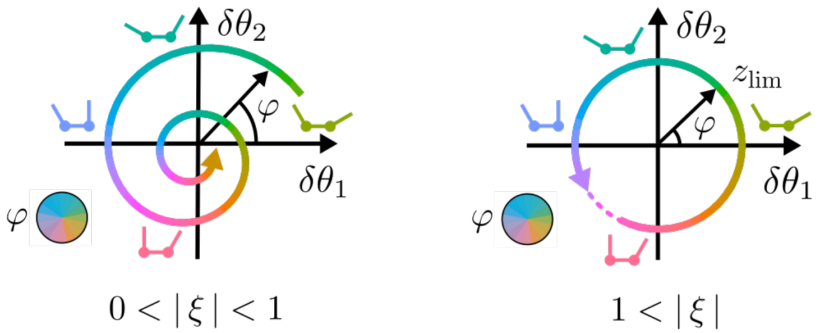

Figure 2.3: The dynamics of the 2 beam system. For $|\xi < 1|$, the system is stable and the oscillation will terminate. $|\xi > 1|$ will result in a limit cycle at finite amplitude [17].

In a further study, the building blocks from [13] were consequently coupled together creating structures such as hexagonal unit cells or large rings [17]. Due to the non-reciprocal coupling between the building blocks, the system shows a tendency to cycle. These rings are not mounted on a platform and can move freely on a horizontal plane. This increased the overall degrees of freedom for the system and these cycles give rise to complex behaviours such as locomotion. Similar to the basic 2-vertex mode, the cycles are Limit cycles since they are self-sustained and have a constant amplitude due to a non-linear limit, in this case, actuator saturation.

2.2. Meta Material

Robotic matter is a system that consists of a large number of small-scale components that can autonomously change their properties and shape. Further research from Brandenbourger et al. took an even further step towards an actual metamaterial consisting of a pattern of many unit cells. This was done by combining hexagonal unit cells into a honeycomb lattice, forming a two-dimensional wall. Due to the active robotic behaviour of each building block in these hexagonal unit cells, the material has a non-symmetric elastic tensor, ie., odd elasticity. With the local control in the building blocks resulting in a change of mechanical properties, this lattice is a Robotic metamaterial with Odd elasticity.

An example of the material response is the impact of a projectile on this two-dimensional wall. As explained in [17] and shown in figure 2.4, A rotation and deflection of the projectile is noted to the right (left) for negative (positive) κ^a/κ. Next to this, the material itself is compressed and experiences vibrations asymmetrically.

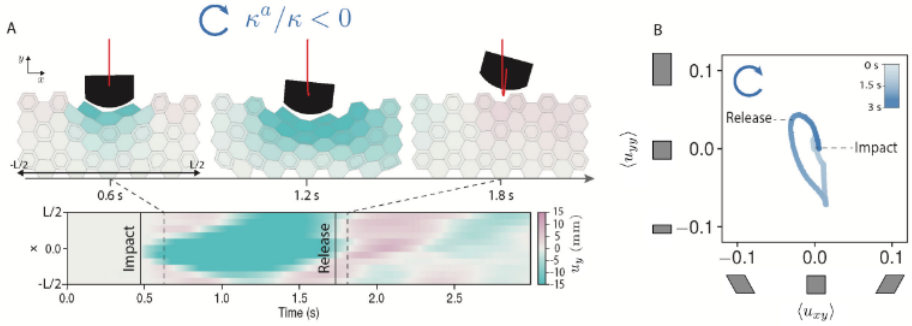

Figure 2.4: Response of odd elastic Honeycomb lattice structure to external impact adding rotation and deflection. [17]

This discrete behaviour is similar to that of a continuum solution with an odd elastic modulus. This means that instead of modelling each individual unit cell, the full system can be described with a set of differential equations, which have been used to simulate the dynamic behaviour of lar[17].

Before using odd elastic materials in real applications, it should first be fully understood and for this, research is done at the University of Amsterdam. The current system of [17] is limiting the scope of this research as explained in chapter 3 and a new unit cell design could open up opportunities to investigate the material properties as explained in section 2.3. Further understanding of this odd elasticity and the current design could eventually lead to many real-world applications as described in section 2.4.

2.3. Research field

The understanding of the limit cycles in an odd elastic material is still only limited and is mostly based on simulation models. While there is a good understanding of the behaviour in 1D, the 2D behaviour of this material is yet to be fully understood, with things such as the synchronization of unit cells leading to a single mode in the material. Through this synchronisation, a material consisting of many unit cells that have behaviour on a microscale could show behaviour on a macro scale such as locomotion. An example of such locomotion is shown in figure 2.5, where a 2D disk consisting of many unit cells can locomote. A test setup with more unit cells would greatly contribute to the progress in the experimental validation of these simulations.

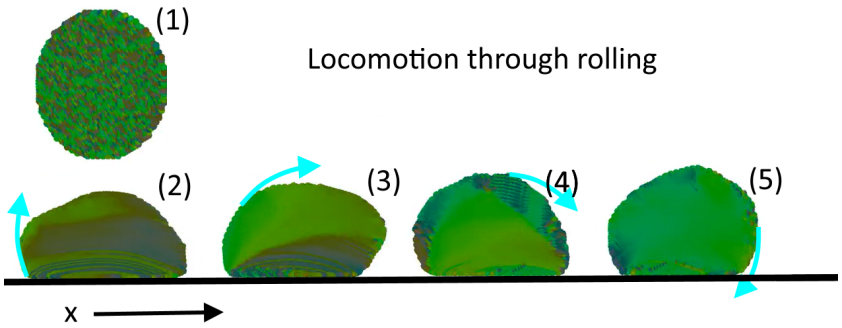

Figure 2.5: Simulation of a cylindrical lattice consisting of many hexagonal unit cells, which will start rolling due to the synchronized limit cycles. [19]

A further step toward applicable materials would be investigating the odd elastic behaviour in 3-dimensional space. While it is not possible to create a 3-dimensional material that has isotropic odd elasticity, many 3 Dimensional structures are possible. This could lead to actual meta-devices such as a stacked 2D structure that responds asymmetrically to impact, a cylinder formed from a rolled-up lattice plane, or

could even be combined in a truncated icosahedron forming a ball (shown in figure 2.6) that would have odd elastic properties.

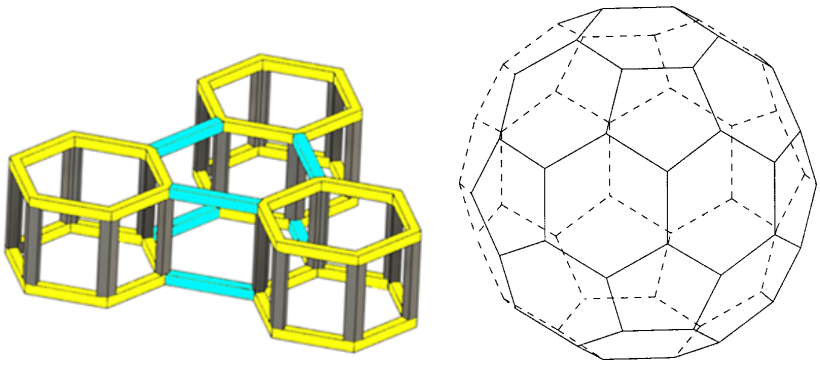

Figure 2.6: Left figure shows an example of stacked unit cells (yellow), coupled in plane with the turquoise joints and vertically with the grey joints. Right figure shows an example on how hexagons can be combined into a 3D Structure, in this case a ball.

To be able to advance this research toward large lattices or 3-dimensional systems, there is a need for an improved design of the unit cell with improvements for the mechanical couplings, size, mass and strength. This problem will be analysed in chapter 3, in which the state of the art is discussed and the problem scope is outlined.

2.4. Real world applicability

This thesis will focus on the design of a unit cell that could be used to create a material with odd elastic properties such as a coupling between compression and shear. After fully understanding the behaviour of this material, there would be many potential real-world applications. Since all computation is done locally and the synchronization of the system happens naturally as shown in the simulations from [20], more unit cells will require more components and energy, but will not increase the complexity of each control system. This autonomous nature of the unit cell means that there is no limit to the scale, both in size and number of individual unit cells, of the material.

Firstly, this active property could be used in structures that need vibration isolation, impact damping, amplification of motion, or even the harvesting of energy from inputs into the material. Secondly, the non-reciprocal nature also means that the material could be used as a general-purpose material for any device that needs wave manipulation.

A futuristic view on an application could for instance be making the sole of a running shoe out of an odd elastic material, which would give the runner a push forwards after compression of the sole during the landing results in shear and therefore a force vector propelling the shoe forwards. While this application is for now purely hypothetical, other metamaterials are already experimented with and followed with great interest [21]–[23].

Due to the limit cycles with a preprogrammed angular direction based on the sign of the gain, the material can also be used for locomotion [17]. The Autonomous nature of this locomotion and the robust and adapting response to various types of terrain make this a unique property that has large potential in various applications. Many robotic systems struggle with locomotion in real-world environments due to changing and uncontrolled conditions. Even though using a very simple control strategy, the wheel used in this research can traverse rough terrain as seen in figure 2.7. The autonomous nature of this behaviour means that it will adapt itself even to unknown and unexpected conditions, while for conventional systems the behaviour has to be preprogrammed or tuned actively.

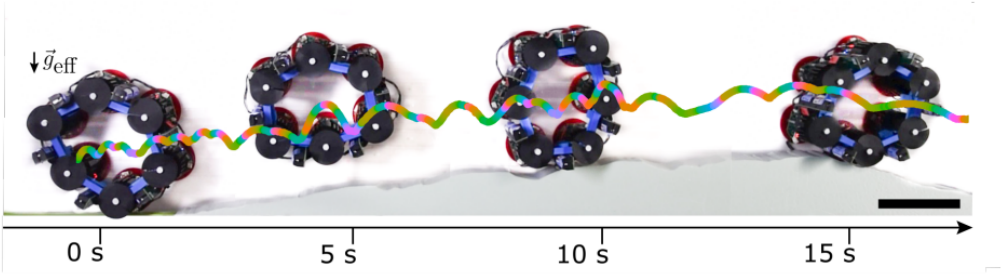

Figure 2.7: Locomotion over complex terrain [17]

Potentially a robot could be equipped with wheels made from an odd elastic material, which would be able to move over any type of terrain. With many actuators, the system could even work after some of the actuators fail, which is a large advantage over a conventional wheel, which has with an axle and motor multiple single points of failure.

3

State of the art analysis

As explained in chapter 2, there is a large scope for further research into odd elasticity in a robotic metamaterial. However, to advance in this research, the design of the unit cell should be improved. By analysing both the current system [17] and its functions, this chapter aims to first find areas for improvement and then create a list of specifications that can be used as a guideline for the design of a new, improved unit cell.

3.1. Unit cell analysis

Similar to how crystalline materials consist of repeated arrays of atoms, Metamaterials often have lattice structures that consist of a recurring pattern. A unit cell is the smallest set of components used for the pattern in the full system. The lattice structure is created by the repetition of the unit cell as many times as defined by the boundaries/size of the system. The unit cells of Brandenbourger et al. [17] consist of six identical vertices, coupled together with flexible joints and couplings to other unit cells with rigid joints, creating a lattice with active and passive hexagons as shown in figure 3.1. Figure 3.2 shows that the unit cell also consists of half (orange) rigid joints.

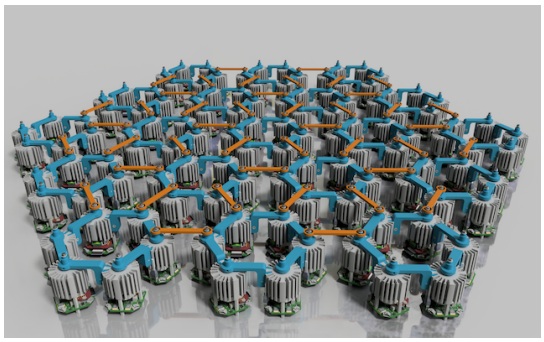

Figure 3.1: 2D Metamaterial consisting of hexagonal unit cells with active vertices coupled with flexible (blue) joints and rigid (orange) joints coupling the unit cells together [24].

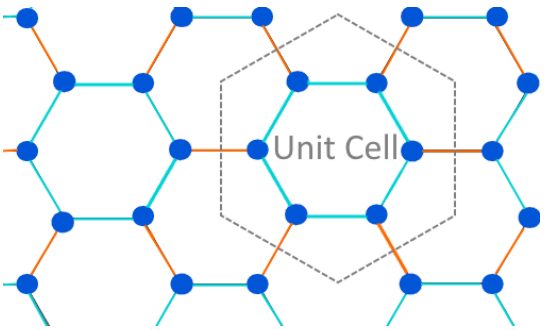

Figure 3.2: Schematic view of 2D metamaterial, outlining the unit cell

3.1.1. Vertices

To understand the unit cell, first, the individual building blocks have to be understood. For an odd elastic system, a combination of springs and odd springs is needed. The building blocks that form this combination for the system of Brandenbourger et al. are firstly the vertices that are actively controlled and secondly, the flexible links coupling these vertices together [13], [17]. As explained in section 2.1.1, coupling 2 of these vertices together with flexible links can already have a non-reciprocal coupling.

The flexible links are elastic bands that act as spring with angular stiffness $\tau_{1(2)} \approx -\kappa\delta\theta_{1(2)}$, where κ

is a torsional spring constant and $\delta\theta_{1(2)} = \theta_{1(2)} - \theta^0_{1(2)}$. This means that rotation in any direction will result in a restoring force in opposite direction.

The vertices act as odd springs and are fitted with a DC motor for actuation, an angular sensor, and a custom-designed control board for both computation and communication with other vertices. Again, for a 2 vertex system, the odd coupling is achieved with the programmed feedback shown in equation 3.1. This means that deformation in a positive direction on vertex 1, will lead to a negative torque on vertex 2, but a direction for vertex 2 will lead to a positive direction on vertex 1 as visualized in figure 2.1.

$$\tau^a_1 = \kappa^a \delta\theta_2 \text{ and } \tau^a_2 = -\kappa^a \delta\theta_1 \tag{3.1}$$

Because there is no equilibrium for the active forces and $\xi > 1$, a limit cycle emerges, only to stabilize in magnitude due to nonlinearities. In the current system of Brandenbourger et al. [17], this non-linearity is caused by the saturation of the torque delivered by the rotational actuator. Each vertex has a maximum torque of $12\,mNm$ and a mass of $0.2\,kg$, which means that the dissipation Γ has to be very low for $\xi > 1$. Because of this, surface friction is required to be removed by levitating the components on a custom-made low friction air table.

3.1.2. Hexagon

By coupling six building blocks with the flexible links, a hexagonal shape is achieved. The hexagon has three independent deformation modes: two shear modes S1 and S2 and one breathing mode B. When $\xi > 1$, a limit cycle occurs after perturbation, which cycles between shear modes S1 and S2 as shown in figure 3.3. This cycle has a direction that is dependent on the sign of the gain k^a and is described with the ratio between active and passive stiffness $\kappa^a/\kappa > 0 || \kappa^a/\kappa < 0$. This means that it is not only possible to control the cycle amplitude by changing the non-linear limit, but also the direction.

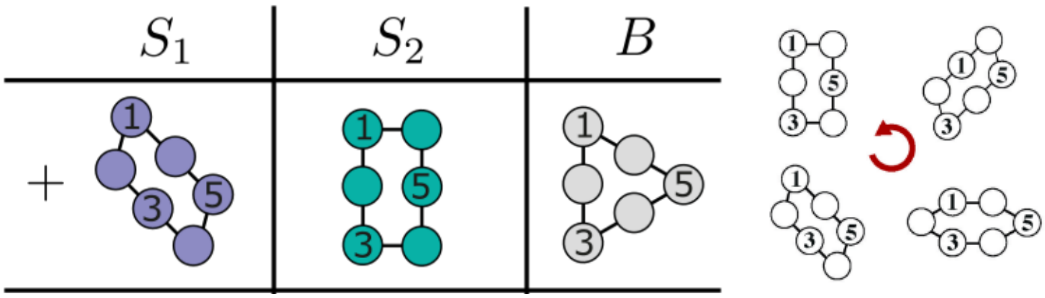

Figure 3.3: The 3 modes of the unit cell and how it cycles through the first 2 [17]

3.2. Functional Analysis

The system from [17] is modular on a vertex level, which allows customizing the system shape from 1D lines to full hexagonal lattices. In order to enable further research into the limit cycles of odd elastic metamaterials, this thesis will focus on designing a new and improved odd elastic unit cell. The first step in the design process is understanding the functional requirements. After that, an analysis of the current system will be done, to find areas where the most improvement is possible. When looking at the functions that together create this required non-reciprocal and actively controlled behaviour, the following list can be created:

- Have with 2 shear and 1 compressing mode a total of 3 Degrees of freedom.
- Contain joints with a passive stiffness.
- Measure to know the value of each degree of freedom.

- Actuate to change each degree of freedom individually.
- Have the energy to allow for non-conservative cycles.
- Control to create odd elastic behaviour

This means that with 6 actuators and sensors to control these 3 degrees of freedom, the system is currently over-actuated and mechanical frustration could reduce the system efficiency. Next to this over-actuation, other improvements for scale, strength and other fields are needed. Firstly, To determine what would be an optimal design, the system specifications have been defined in section 3.3 and secondly, from these specifications a research scope is chosen. Finally, Guided by this scope, targeted literature research has been completed to acquire knowledge on the subsystems; Resulting in a final overall concept choice.

3.3. Specifications

During this thesis project, a unit cell will be designed that has the functions described in the previous section. The next step is to form requirements the design has to comply with as well as set some wishes, which should then result in an optimal design. To create this list of requirements and wishes, the system has been characterised by the following list of specifications:

- Scale
- Strength/weight ratio
- Level of odd elasticity
- Displacement size ratio
- Bandwidth
- Modularity
- Control
- Dimensionality

In the following subsections, these specifications are explained and the influencing factors, as well as their influence on other specifications, are detailed.

3.3.1. Scale

An important attribute of a metamaterial is the scale of the individual parts of the lattice structure. While in the design of Brandenbourger [17] a hexagon has a diameter of $150\,mm$ (and the unit cell which includes the rigid joints is even $300\,mm$), there are examples of active metamaterial unit cells as small as 20µm [25]. One of the identified goals is to decrease the size of the unit cell and this section aims to explain why this is beneficial and identifies the effects of this change of scale.

In the field of passive metamaterials, the scale can be directly related to the frequency bandwidth of the material through phenomena such as Bragg scattering, or local resonances [26]. This dependency is not present in an active metamaterial such as the design of Brandenbourger and therefore, the scale is freely decided based on other influences.
While on a macro-scale, metamaterials can be categorized as robots or mechanisms, they have the unique potential to be scaled down to a level where they instead now exist as a close relative to biologically existing materials. Instead of using a layer of rubber for vibration isolation in an engine mount, a thin layer of a new active metamaterial consisting of micro or even nanoscale unit cells could be used. Bauer et al. for instance developed a metamaterial consisting of nanoscale lattice honeycomb structures with a very high specific strength of 1.2 GPa at 0.6 g cm−3 [27]. When scaled down far enough, metamaterials could just become materials with an arbitrary property designed to the needs of the end-user.
A more practical reason for scaling down is the ability to fit more unit cells in the same size experimental setup. While the current setup consists of a 2D wall with 17 hexagonal unit cells [17], scaling down the unit cell 10 times, would allow fitting 100 times as many unit cells in the same setup. This would enable

further research and scaling down could decrease the cost of such a setup.
Even with a similar geometrical design, scaling affects the functions and properties of a unit cell. It was found that for Bauer's glassy carbon nanolattices that smaller scale of the same unit cells increased stiffness at a higher rate than the density and therefore lower scale was preferred for maximizing the specific stiffness [27]. In a wider review, Bauer [28] also explains the importance of production methods that enable lattice structures to be created at a continuously decreasing scale as shown in figure 3.4.

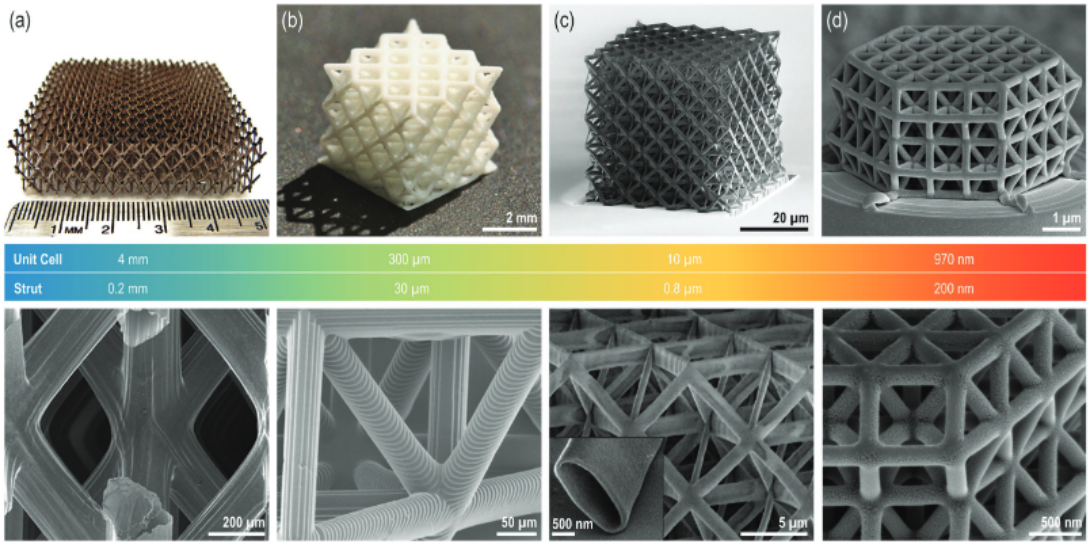

Figure 3.4: Similar Lattices decreasing from the millimeter- to the nanoscale, detailed with both unit cell and strut size. [28]

A good example of how scale affects structural properties is the stiffness of a cylindrical rod in bending. The stiffness will scale with:

$$k \propto \frac{r^4}{L^3}, m \propto r^2 L \tag{3.2}$$

where r is the radius and L is the length of the rod and k and m are the stiffness and mass respectively.

When calculating the effect of scale on the ratio between the mass and stiffness of the material, we can set scaling parameter a and an aspect ratio of $r = L * a$ for the cylinder. Taking into account the mass of the material results in the specific bending stiffness D, which will increase exponentially at a smaller scale, for any aspect ratio a. Similarly, the stiffness of the designed unit cell will be significantly influenced by the effect of scale.

$$D = \frac{k}{m} \propto \frac{r^4}{L^4 r^2} \propto a^2 L^{-2} \tag{3.3}$$

Since the natural frequency of a system is calculated by $\omega = \sqrt{(k/m)}$ and lower scale results in a higher specific stiffness, the natural frequency is also expected to increase.
Aside from calculating the effect of scale, based on a physics law, it is also possible to check the effect of scale by investigating existing systems. An example of this is the investigation of Dermitzakis et al. on actuators [29], which found that the maximum delivered force scales isometrically with the motor mass. This method is very useful for comparing existing full system solutions, without needing in-depth calculations.
Scaling laws not only affect the unit cell but also its manufacturing methods. Production methods that focus on high precision or small scale are less common and usually more complex. Therefore, the assumption is made that the cost of a system will only decrease for a decreasing scale as long as the manufacturing process remains similar. When more complex methods are needed, it could increase in price. While scale is important, manufacturing methods are also dependent on material properties and geometry as further explained in section 5.4.
To conclude, the scale has a significant influence on the performance of the system. A smaller scale

is shown to be advantageous due to higher specific stiffness, lower mass and resulting higher natural frequency. The cost per unit cell is expected to be lower and finally better usability in a test setup. The limiting factor for scaling down will most likely be manufacturing methods as well as the availability of components at a smaller scale.

3.3.2. Strength/weight ratio

When considering any type of material, specific stiffness $\frac{E\,[Pa]}{\rho\,[kg/m^3]}$ and specific strength $\frac{\sigma_{F\,[Pa]}}{\rho\,[kg/m^3]}$ are important for material selection in engineering. Since the unit cell has an active and a passive component, these properties are linked to each other. Increasing the specific stiffness, will for instance enable the material to support its weight passively under gravity without large deformations. However, increasing the stiffness will also require a higher actuator force for the same motion.
Similar to the specific strength, the strength/weight ratio $\Delta[\frac{N}{kg*m/s^2}]$ defines how many times the unit cell can lift its weight. For example, an ant can carry up to 20 times its weight, so $\Delta = 20$. The specific load case for the system is shown in figure 3.5, where the system has been simplified to a mass-spring system with an actuator and an external gravitational force. The system should firstly compensate for its own gravitational force, but secondly, also provide additional force and deformation required for the odd spring.

$$\Delta = \frac{F_{Actuator}}{F_{Gravity}} = \frac{F_{Actuator}}{mg} \tag{3.4}$$

For the system designed by Brandenbourger et al., $\Delta = 0.3$, meaning it cannot support itself under full gravitational load [17].

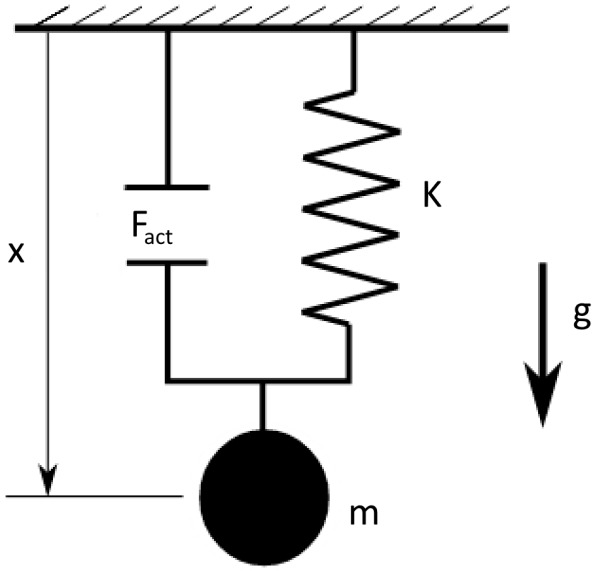

Figure 3.5: Deforming of a simplified mass spring system due to gravity.

To be able to have n vertically stacked layers of hexagons, it is essential that $\Delta > n_{Layers}$. On top of that, when the material would be used for impact handling, the material should be strong enough to slow down and support the material.
The passive stiffness is affected by both geometry and material properties. Similarly, active actuation

is dependent on power and force density. However, both methods are also dependent on each other. A higher passive stiffness directly requires a stronger actuator for the same deformation, but a stronger actuator will be heavier and therefore require a higher passive stiffness.

The choice of the actuator will play an important role in the process of increasing the Strength/weight ratio. Passive mass of components such as the arms, micro-controllers and an energy source will also affect this ratio.

3.3.3. Level of odd elasticity

Section 2.1.2 explained that for odd elastic materials, there are the additional moduli K^0 and V^0, which describe how the material responds asymmetrically.

Because the goal of this thesis is to design and build a unit cell with odd elasticity, the goal will be to maximize the magnitudes of K^0 and V^0. By changing the active feedback term K^a from equation 3.1, it is possible to affect them, but there are limits to this such as the saturation levels of the actuator. However, it is possible that with the same stiffness and actuator, different implementations of odd elasticity will lead to a higher or lower K^0 and V^0 and this will be an important metric to choose the best mechanism.
In Chapter 4, different implementations to achieve odd elasticity will be discussed and compared for their mechanical efficiency and odd moduli.

3.3.4. Displacement size ratio

As described in the functional analysis, the unit cell has 3 degrees of freedom, which are all able to be actuated. The magnitude of this actuation, the displacement, is a key characteristic of the unit cell. To remove the effect of scale, this displacement has been calculated as a ratio of displacement compared to the unit cell size, the displacement size ratio $[\lambda]$. This is very similar to strain ϵ and can be calculated with:

$$\lambda = \frac{\delta}{L_0} \tag{3.5}$$

When looking at the unit cell from Brandenbourger, a maximum motion of 35 mm (contraction of two opposing unit cells) leads to an $\lambda = 35/150 = 0.23$. This high displacement ratio can be beneficial in cases such as impact handling where the acceleration of the impact should be minimized for things such as airbags, or a crumple zone of a car. Also, other applications of an odd elastic material such as actuation, locomotion and energy transfer will benefit from a larger displacement.
The larger displacement however also comes at a cost of either power or lower stiffness. When the stiffness of the material remains equal, a larger displacement requires a higher peak force of the actuator. This and higher movement speed due to the increased travel for the same natural frequency will increase the maximum power exponentially for a simplified system:

$$P = F * V = K * f * x^2 \tag{3.6}$$

Where $k\,[N/m]$ is the stiffness, $f[Hz]$ is the frequency and $x[m]$ is the amplitude of the cycling system. This influence of the power, force or frequency of the system can determine the choice for the actuator. Additionally, the displacement also defines the amount of space in the middle of the unit cell that can be filled with incompressible components, such as the actuator. This has been visualized in figure 3.6. Finally, the absolute displacement of the joints has to be large enough to allow for accurate measurements.

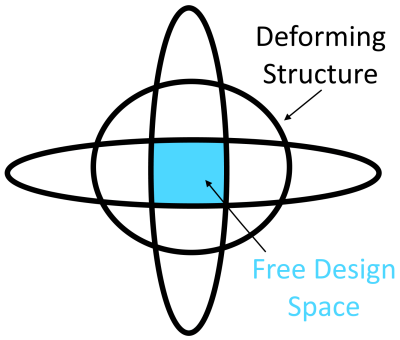

Figure 3.6: Deformation of cylinder and the resulting free design space for incompressible components

3.3.5. Bandwidth

The bandwidth or frequency response of a system describes the relation between input and output for varying frequencies. An example is the passive non-reciprocal materials that showed no transmission (no output for any input) for a certain bandgap. As discussed in section 3.3.1, the active component of the unit cell causes there to be no minimum achieve-able frequency. The upper limit could, however, be limited when using a spring, which at frequencies higher than its natural frequency increasingly decreases the possible transmission between input and output.
This means that for the same amount of movement, a significantly larger force is needed when moving faster. Due to the limited maximum force of the actuator, movement speeds faster than the natural frequency will result in significantly lower motion. For this system, the upper limit of the bandwidth has been defined with the half-power point (-3dB).
Since the natural frequency of the mass-spring system is dependent on the stiffness and mass through $f = \frac{k}{m}$, options to change the bandwidth are changing the mass, or stiffness of the system. This could be done conventionally, by decreasing the overall mass or increasing the passive stiffness. Alternatively, gravity compensation [30] could decrease the effective mass, or a 0 stiffness joint [31] could even remove the natural frequency altogether.
To characterise the frequency response of the hexagonal unit cell from Brandenbourger [17], a model was built in MATLAB Simscape Multibody. This model is a simplified representation of a single unit cell with rotational actuators in each vertex, that are each constrained on a ground plane without any friction. The control function of each vertex can be described as shown below:

$$\tau_i = k_{spring} * \delta\Theta_i - (k_{motor} * (\delta\Theta_{i+1} - \delta\Theta_{i-1}) \tag{3.7}$$

Although this is an over-actuated system, it represents the current existing unit cell and therefore, combined with its specifications such as stiffness and weight, a representative model was created. This model was simulated and shows the following frequency response for a gain of 0.72.

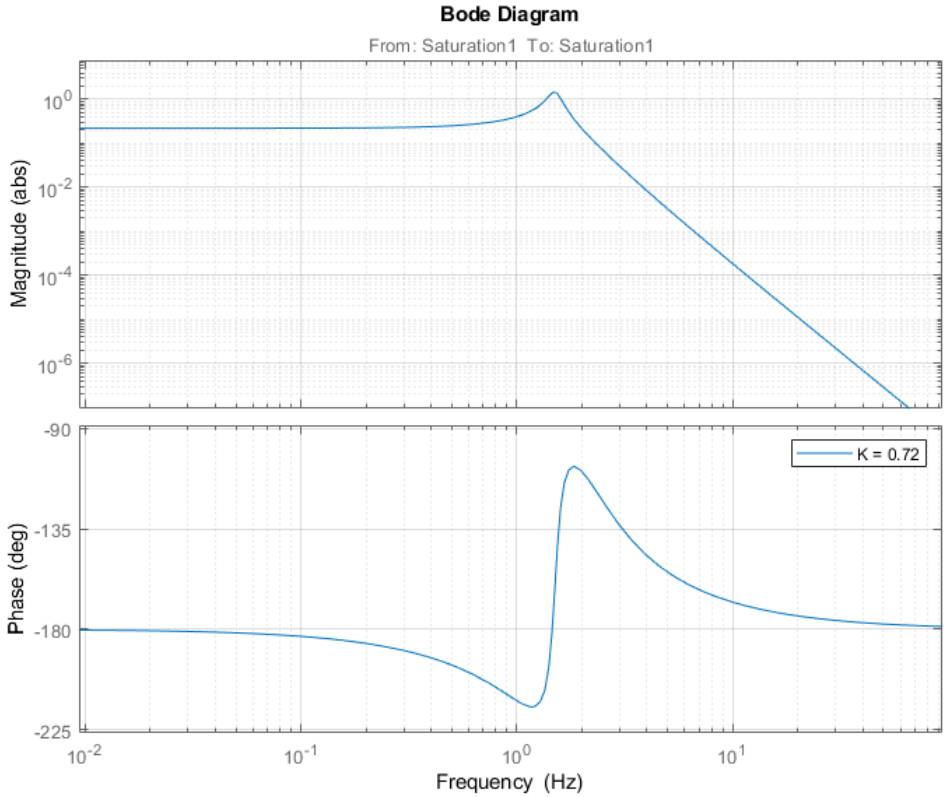

Figure 3.7: Bode plot of the system as designed by Brandenbourger [17]

The limit cycle frequency is equal to the resonance peak and as shown in the Bode plot is $1.5\,Hz$. This frequency is independent of the Gain, or the maximum torque of the actuator, which also means that the designed frequency is not possibly changed by software. While an increased bandwidth due to a higher possible frequency can be an advantage for the response to high-frequency external inputs and therefore could help with impact handling, it also leads to a higher limit cycle frequency. As explained in the previous section, this higher frequency will also lead to the increased power consumption of the system. Research could still be done into improving the control system, for instance by applying filtering to create artificial peaks in the frequency response at other than the resonance frequency, creating a programmable limit cycle frequency. If that would be possible, it would be optimal to have a bandwidth as large as possible.

Next to the mechanical response, the bandwidth of the design is also defined by the frequency of the control system. The Nyquist frequency dictates a sampling frequency of minimum double the frequency at which the system oscillates to avoid aliasing. Furthermore, a common rule of thumb is to use a control system frequency of $f_{control} = 10 * fi$, meaning that if the resonance frequency is 10 Hz, the control system should run at a minimum frequency of $100Hz$.

3.3.6. Modularity

The original system by Brandenbourger et al. [13] had a great benefit of being modular and therefore re-configurable into straight lines, Hexagonal unit cells, or even circular unit cells with many more vertices. This was ideal as a tool for research into the odd elasticity when very little was known and the research direction was not yet set. However, the downside is that the vertices are quite heavy and not easily scaled down. From this, it can be concluded that the level of modularity is an important characteristic of the unit cell, where a lower degree of modularity can improve the performance, but at a cost of flexibility in application.
When looking at the top-level design of the unit cell, there are 3 options for modularity:

- Fully modular on vertex level
- Modular on a Unit cell level
- Not modular, manufactured as a bulk metamaterial

Next to these levels of modularity, another option would be to add modularity on a sub-component level. For instance, a frame with passive stiffness could be produced for a full metamaterial and coupled to ”Active” Unit cells which are modular. During the design of the unit cell, multiple options for this will be investigated.

3.3.7. Control

The active behaviour of the unit cell is created by coupling measurements to actuation in a closed-loop control system. For this, a controller is needed, which was solved in the current unit cell by adding a microcontroller in each vertex. This microcontroller receives inputs from its neighbour vertices and with the odd control function converts this into a signal to actuate the rotational motors. Next to the control of the cycle, other control functions such as turning the system on and off are also done by these microcontrollers with the use of Wi-Fi communication.
When decreasing the size or mass of the system, it becomes apparent that electronics will become a limiting factor. This can be solved by changing the controller to be centralized for each unit cell, removing the need for inter vertex communication. A further step could be to completely remove programmable electronics and instead run a control loop with hardware electronics. Although these options could significantly decrease the size of the controller, they come at the cost of losing the option for reprogramming and therefore design freedom.

3.3.8. Dimensionality

The initial odd elastic behaviour was proven in 1D movement space [13], before moving to a 2D space, where the behaviour is yet to be fully understood [17]. Naturally, there is interest in having the odd elastic behaviour in full 3D movement space, which could show interesting behaviour and is closest to actual real-world applications.
Since this movement space has a major influence on the shape and functions of the unit cell, it should be decided early on in the process. To decrease the level of complexity, when moving to 3D movement space, an intermediate concept could be implemented, where 2D Layers are stacked and elastically coupled. This would mean that the odd elastic property is active in 2D, but the material constitutes a 3D space and due to the elastic couplings, the behaviour is not rigidly coupled and each layer can deform independently. This concept is called 2.5D and has as advantage that it would be possible to use the design of a 2D unit cell with some minor alterations.

3.4. Project scope

As described in chapter 2, the motivation for redesigning the unit cell is to create an improved platform for the University of Amsterdam to continue its research into the active odd elastic metamaterials. Therefore, the targeted specifications of the system and their trade-offs were discussed with the stakeholders in this project. From this, it was concluded that both Scale and Strength/weight ratio are the most important specifications to achieve this improvement:

Wishes

1. **Scale:** Scaling down has been identified to be the most important goal of this thesis project. While a smaller scale is better, the minimum size will be limited by the available production methods, the cost per unit cell and the complexity of the design.
2. **Strength/weight ratio:** After identifying that the strength/weight ratio, Δ, was limiting the use of the current unit cells, the decision was made to significantly improve Δ, to allow for vertical stacking as well as handling of external loads.

Next to these optimization targets, various specification requirements have been defined, which will

limit the design scope:

Requirements

1. **Modularity:** The system should be modular on a unit cell level, to allow for different geometrical shapes of the metamaterial and in this way also keep open the possibility for 2.5 D or curved planes.
2. **Control:** Because of the modularity at the unit cell level, it is possible to centrally control the unit cells. To study the effect of control gains, or even add complexity to the control system with for instance filtering, or the logging of data, some communication is required, which preferably would be wireless to allow for quick reprogramming of multiple unit cells.
3. **Dimensionality:** To limit the scope, an initial target has been set for 2D movement, with the option to move towards 2.5D Designs, when the time frame would allow.
4. **Displacement size ratio:** While functionally the motion of the unit cell is not yet defining a minimum displacement, a minimum λ of 10% has been required. In this way, there is significant motion allowing for higher accuracy measurements and the system is more representative for potential future applications.
5. **Allowing manual repairs:** Although not yet discussed, it is very important that the setup can be used extensively and is possible to be repaired manually. This means that microscopically small systems are out of the research scope.

By combining these wishes and requirements with the functional requirements that have been defined in section 3.2, the project scope is clear and the problem statement has been defined:

The design, manufacturing and testing of a mesoscale, 3 DOF unit cell with odd elasticity caused by active closed-loop control and actuation. This unit cell should be as small, strong and light as possible while meeting all other set requirements.

3.4.1. Design Targets

While some of these requirements are not directly measured, others can be directly used for a theoretical calculation of the design parameters of the system as explained in Appendix B. As input for these calculations, a target scale, deformation and Strength/weight ratio have been defined:

- **Scale:** resulting in 10 times the amount of Unit cells in the same amount of 2D Space, a decrease in size of $\sqrt{10} = 3.1$ has been targeted. This means that each hexagon has a maximum size of 48 mm.
- **Strength/weight Ratio:** When 5 layers of hexagons would be stacked on top of each other, a square vertically self-supporting metamaterial with 25 hexagons could be realized. Therefore a Strength/weight Ratio target of 5 has been set. This is combined with a target mass of $5g$.
- **Deformation:** In order to have significant deformation during the limit cycles, a target of more deformation larger than 10% of the unit cell size was set

By using these inputs, the corresponding targets are calculated with the model explained in appendix B. this results in the following design targets:

Requirement	Target value
Passive stiffness	$5.1\frac{mNm}{rad}$ ($77.1\,N/m$ Linearized)
Actuator peak force	$0.78N$ *
Hexagon deformation (Actuator stroke)	$5mm$ (10%)
System mass	$5g$
Natural frequency	$27Hz$
Hexagon size	$< 48mm$

Table 3.1: Table containing main design targets

These Design targets will not be final, but give a good indication of the design scope in which solutions should be found. In chapter 5, 4 and 6, solutions for things such as manufacturing, implementations of odd elasticity and potential sub-components are discussed.

**This is the actuator force needed for 1 diagonally connected linear actuator per hexagon. Other concepts requiring torque would need a different requirement that is linearly related to this requirement, but since this is the final chosen concept it is displayed like this.*

4

Achieving Odd Elasticity

As explained in chapter 2, odd elasticity can only occur in a non-conservative system. To break the energy conservation, external energy should be converted into motion through actuation or vice-versa. This chapter aims to investigate how odd elasticity can be achieved with actuators. Different actuation methods with their most suitable control function are compared through metrics such as complexity and mechanical efficiency.
While the original concept of Brandenbourger [17] used a rotational actuator in each joint, it was already previously noted that only 3 actuators are needed for a hexagonal unit cell to create a coupling between compression and shear. Through both calculations and modelling unit cells in MATLAB Simscape Multibody, three different concepts for actuation have been investigated. Appendix D explains in more detail how the simulation is set up. For each considered concept, the base model consists of a mechanism with rotational joints with a passive stiffness coupled with rigid arms.
In order to estimate the mechanical efficiency and compare the different actuation strategies, the ratio between the required force and stiffness of the joint is calculated. A higher required force means that the same amount of movement requires more energy, which is undesired.
After discussing 3 initial concepts, a very different concept with variable length links and a concept with actuators divided over multiple hexagons are discussed.

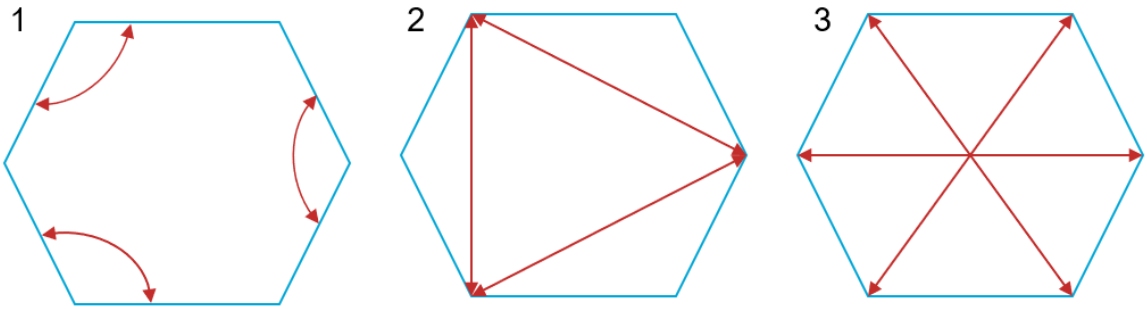

Figure 4.1: The different actuation methods. (1) is the rotational actuation, (2) is the Linear next nearest neighbours actuation and (3) are the Linear Diagonal Actuators.

4.1. Rotational Actuation

The first concept is very similar to the system of Brandenbourger [17] and consists of 3 rotational actuators as shown in figure 4.1. The control function of this unit cell is identical to the function from [17], although the actuators are now not coupled to their direct, but the next nearest neighbours.

$$\tau_i = k_{spring} * \delta\theta_i - k_a * (\delta\theta_{i+1} - \delta\theta_{i-1}) \tag{4.1}$$

However, a bigger challenge would be the integration of a rotational actuator at a small scale. Next to this, force densities of rotational actuators at this scale could be different to linear actuators. For sufficient motion, a force to stiffness ratio can be calculated as if there is always a perpendicular force on the neighbouring joint with $F = \frac{\tau * \delta\theta}{L_{arm}}$ resulting in a force/stiffness ratio $\frac{N}{rad}$ of 133 is needed (Figure 4.2).

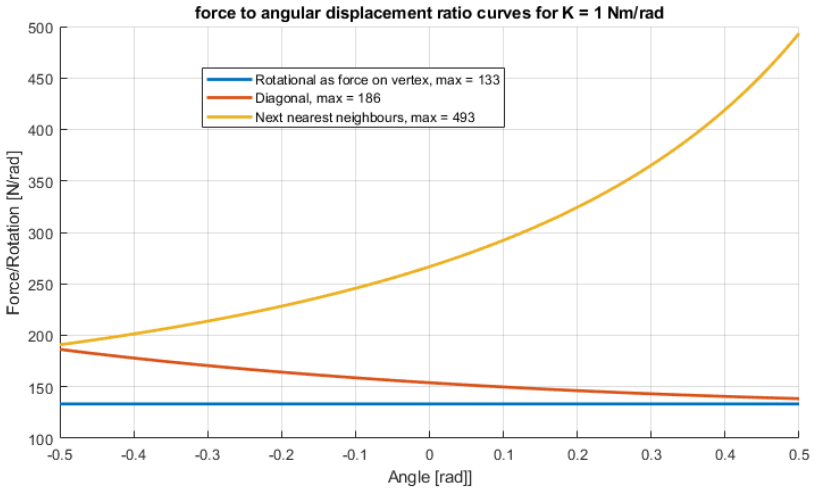

Figure 4.2: Relation between Force/stiffness ratio and the required deformation angle

4.2. Linear next-nearest-neighbour actuation

Looking at linear actuators, the first option is to use an actuator that couples both neighbouring joints of a joint that is wished to be rotated. This method is shown in figure 4.1 and allows for easy conversion from the length of the actuator to the angle of the enclosed joint. Therefore, the same above-described control function could be used. However, because this relation is not linear, the ideal control function is more complex:

$$F_i = \frac{\tau_i}{L_{arm} * cos(\theta i/2)} = \frac{k_{spring} * \delta\theta_i - k_a * (\delta\theta_{i+1} - \delta\theta_{i-1})}{L_{arm} * cos(\theta i/2)} \tag{4.2}$$

Using the next-nearest-neighbour method also causes two further problems:

1. **Force loss**: At the stable position, the angle of $120°$ results in $F_{moment} = F_{actuator} * cos(\frac{\pi}{2}) = 0.5 * F_{actuator}$. Due to this, a strain force on the joint and its arms, which is essentially stretching the arm of $F_{strain} = F_{actuator} * sin(\frac{\pi}{2}) = 0.87 * F_{actuator}$ is also present. This can have negative effects on the performance of for instance compliant joints.
2. **Saturation force**: While the actuator can only achieve a maximum force, the effect of this force on the maximum angle is non-symmetrical and therefore again for maximum control accuracy, a saturation limit of $F_{max} = \frac{cos(\frac{\theta}{2})}{F_{max} * cos(pi/3 + (\delta\theta_{max})/2)}$ where $\delta\theta_{max}$ is the maximum rotation, for instance $\frac{\pi}{6}$.

As can be seen in figure 4.2, simulating the system for a deflection of 0.5 rad, shows that a maximum force/stiffness $\frac{N}{rad}$ ratio of 489 is required, which is 3.7 times higher than for the rotational actuators. These problems could be solved by using stronger actuators and flexures that have low bending-, but high tensile stiffness.

4.3. Linear Diagonal actuators

A different method of using linear actuators is to connect them diagonally with the opposing joint as shown in figure 4.1. Due to a more complex relation between the length of the actuators and the angles of the passive joints, where the relation between the lengths and angles cannot be decoupled

to individual pairs of angles and lengths. Therefore, a different control function was determined where the odd elasticity is based on the lengths of the neighbouring actuators:

$$F_i = k_{spring} * \delta\Theta_i - k_a * (\delta L_{i+1} - \delta L_{i-1}) \tag{4.3}$$

As shown in figure 4.2, a force/stiffness $\frac{N}{rad}$ ratio of 186 is required, meaning it is less efficient than the rotational actuators. However, it is already much more efficient than the next-nearest-neighbour method and due to the diagonal connection, a larger actuator can be used without clashing with the hexagon perimeter.
As described, the ratio between maximum force and stiffness and the required rotational angle is not linear for the linear actuators, due to the changing angle between the force and the direction of the moment arm. This is visualized in figure 4.2, which highlights the importance of the required movement of the actuator. However, it also shows that even at equilibrium, there is a significant difference between both methods that use linear actuators.

4.4. Variable link length Actuators

A different method that could be used is changing from rotational joints to hexagons with stiff corners and variable-length links due to a parallel spring and actuator in direction of the link. This would change the number of degrees of freedom for a single hexagon to 4, which means there are more modes than required and the system is underconstrained. An alternative could be using a triangular lattice structure with variable length links and flexible joints resulting in 3 DOF for individual triangles and 2 DOF per triangle in a full lattice. There is not yet a known advantage of using this different design, but the method could be investigated through similar modelling methods as used for the hexagonal structures.

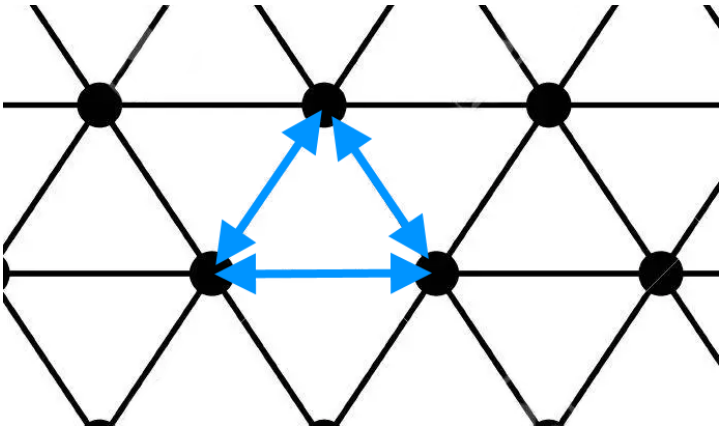

Figure 4.3: Triangular lattice with variable link length actuators (Blue).

4.5. Divided actuators

Through the Kutzbach Criterion, we can conclude that a single hexagon has 3 degrees of freedom: $N_{DOF} = 3 * (L - 1) - 2 * J = 3 * (5) - 2 * 6 = 3.$, Where L is the number of links and J is the number of joints. However, when combining this hexagon into a lattice structure, there is an average of 3 links and 2 joints per hexagon leading to $N_{DOF} = 3 * (2) - 2 * 2 = 2DOF$ as visualized in figure 4.4.

Figure 4.4: Hexagon enclosed in honeycomb structure, with only 3 individual links (Lines) and 2 joints (Circles).

Because there are only 2 DOFs for the enclosed hexagons, having 3 Actuators per hexagon is over-actuated, resulting in possible frustration of mechanical forces and therefore lower mechanical efficiency. A solution for this could be decreasing the number of actuators per hexagon and therefore would need a different principle of odd elasticity. The above-described methods of actuation still hold with the concept of divided actuation, but the odd elasticity can no longer be achieved on the level of just 1 hexagon. One of the possible methods could for example be as shown in figure 4.5, with the same control function as for the diagonal actuators, but now spaced out over 3 hexagons:

$$F_i = k_{spring} * \delta\Theta_i - k_a * (\delta L_{i+1} - \delta L_{i-1}) \tag{4.4}$$

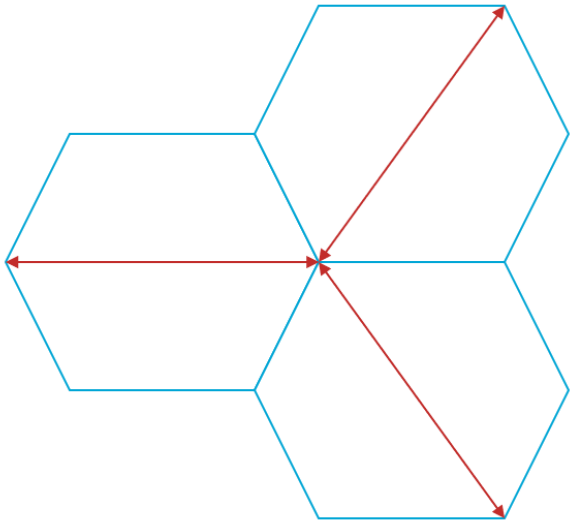

Figure 4.5: 3 Hexagons with only 1 actuator in the distributed actuation method.

Next to avoiding mechanical frustration, another more practical advantage is the amount of available design space for the actuator. For the other linear actuator designs, there will be very limited design space for each actuator, or they will have to be stacked vertically. Stacking vertically might become a challenge when using electromagnetic actuators and the static attraction of magnets.
For a classic mechanism with zero modes, the divided actuator concept would be under-constrained,

due to only controlling 1 of the 2 degrees of freedom. However, as stated in section 3.4.1, each joint will have a passive stiffness and simulation shows that the required mode shapes have a significantly lower frequency than other modes. This will be further explained in part II, where the design and manufacturing process is explained.

Comparing the odd moduli

In order to compare the lattice of Brandenbourger et al [17] and a lattice with the divided linear actuators, it is important to calculate the odd bulk moduli. Guido Baardink from the Souslov Lab at the university of Bath has calculated the odd ratio $v^0 = \frac{K^0}{\mu}$ for both as shown in figure 4.6 and the corresponding equations for [17] 4.5 and the divided concept 4.6. Here, $\tilde{\kappa}_a = \frac{\kappa_a}{\kappa}$, $\tilde{k}_a = \frac{k_a}{\kappa/\ell^2}$ and $\tilde{k} = \frac{k}{\kappa/\ell^2}$. From these equations, we can conclude that both lattices have odd elasticity, but when assuming that the links are fully rigid, a higher odd ratio can be achieved with the lattice from brandenbourger et al.

$$v^0 = -\frac{\sqrt{3}}{3}\tilde{\kappa}_a \left[1 + \frac{3}{\tilde{k}}\left(2 + \frac{(\tilde{k}+6)(\tilde{k}+4)}{(\tilde{k}+3)^2}\tilde{\kappa}_a^2\right)\right]^{-1} \rightarrow \lim_{\tilde{k}\to\infty} = -\frac{\sqrt{3}}{3}\tilde{\kappa}_a \tag{4.5}$$

$$v^0 = -\frac{\sqrt{3}}{8}\tilde{k}_a \left(1 + \frac{2}{\tilde{k}}\right)^2 \left[1 + \frac{3}{\tilde{k}}\left(2 + \frac{\left(\tilde{k}^2+6\tilde{k}+6\right)\left(\tilde{k}^2+9\tilde{k}+10\right)}{8\tilde{k}^2(\tilde{k}+3)^2}\tilde{k}_a^2\right)\right]^{-1} \rightarrow \lim_{\tilde{k}\to\infty} = -\frac{\sqrt{3}}{8}\tilde{k}_a \tag{4.6}$$

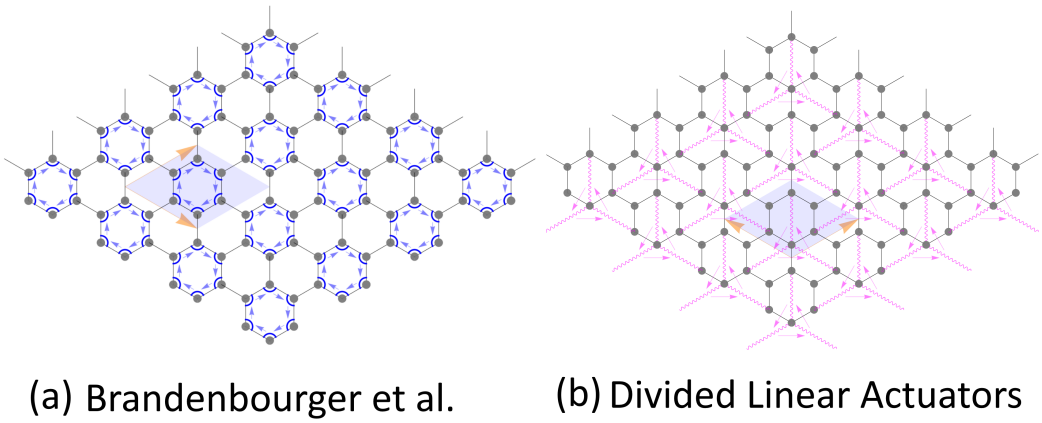

Figure 4.6: Visualization of lattice consisting of both concepts for an odd unit cell. [32]

This chapter has highlighted various options for achieving odd elasticity through actuators and concluded that the Divided Actuator principle with diagonal actuation is the most efficient mechanically. While the odd ratio that can be achieved with the newly proposed unit cell design is lower than the work from [17], the strength to weight ratio is expected to be much higher due to the application of linear actuators. The placement of the actuator is advantageous and it is expected that unwanted modes due to the underconstrained system will not occur. Therefore, it was decided to choose the divided actuation method going forward in the design.

5

Mechanical metamaterials

In the following sections, different types of metamaterials are investigated that could highlight useful technologies or insights. These could aid the redesign of the active non-reciprocal unit cell. Firstly, some working principles of (non-robotic) mechanical metamaterials will be investigated. Although they are passive, they give a great insight into the available mechanism possibilities such as slender elements or elastic beams which could be used in an active configuration as well. Secondly, literature on active materials such as robotic metamaterials is investigated.
One of the main reasons that enabled the development of these new materials is recent developments in manufacturing technologies with techniques such as Additive Manufacturing (AM). Section 5.4 describes these methods and their advantages as well as limitations.
In chapter 6, the subsystems of the unit cell will be discussed and result in possible solutions for each. While this section describes what is possible, Chapter 7 will summarize the literature study and formulate the concept choice.

5.1. Mechanism requirements

In section 3.2, a list of functions has been defined of which some will be full-filled by the mechanism. The mechanism has to allow for 3 degrees of freedom; 2 shear and 1 compressing mode. Simultaneously, the mechanism should in some way create a passive stiffness for the odd elasticity. This stiffness can also be used to saturate the actuators, providing the non-linear limit required for the limit cycle.
Next to the mentioned top-level functions, the mechanism also is responsible for acting as a frame. This means that everything should be physically connected, while still able to actuate the degrees of freedom. This will be a challenge, considering that the computational elements will have a significant mass and therefore should be constrained, but should not affect the dynamic behaviour of the unit cell. While the requirement for the active part is to be modular on a Unit Cell level, it is not specifically required that the mechanisms are modular. A non-modular mechanism design could allow for higher accuracy and faster-manufactured mechanisms. However, this can only work when a good method is found for connecting the active parts to a passive frame.

5.2. Mechanism styles

A mechanism is a system with designed zero modes and therefore degrees of freedom. They usually consist of a combination of rigid bodies coupled together with hinges that allow for free motion. Alternatively, compliant joints can be used to create metamaterials, using slender beams that with low-energy deformation in certain directions approach the free motion of hinges. This allows the design of soft metamaterials that undergo shape changes very different to normal elastic media [33]–[35].
Another field that makes use of local much lower stiffness is origami-based metamaterials, where plates are linked together by flexible hinges. Because of their folding motions with a single degree of freedom, they enable designing multi-shape materials, which can be produced from 2D Sheets. These famous patterns and shapes have been used in engineering already a long time with, for example, the solar

panel on a spacecraft [36] and usually make use of existing folding patterns such as the Miura-ori [37]. Recently, more complex materials that for example have multiple shapes [37], programmable modes [38] or even active behaviour [25].
Kirigami-inspired metamaterials are related to origami-based materials because they are also created from thin sheets of material, but this time by creating designed patterns of cuts. These cuts are designed to significantly change the elastic properties or shape of the material. This can lead to flexibility in otherwise rigid materials for instance a lithium-ion battery [39] or complex designed out of plane deformations [40]. The fields of Kirigami and Origami can also be combined and create all kinds of complex 3D materials from a flat sheet [41].

Figure 5.1: The large negative Poisson ratio material from Wang [34]

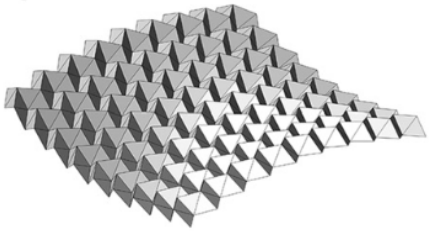

Figure 5.2: one of the modes of the Kirigami shape created by Schenk [37]

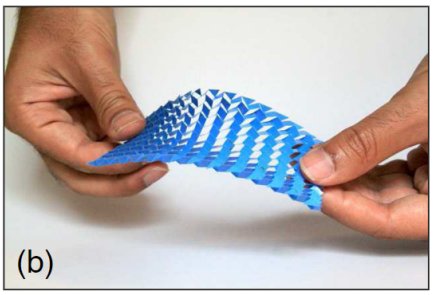

Figure 5.3: bending mode of the Kirigami material made by Rafsanjani from a sheet of only 127µm thickness [40]

New manufacturing and modelling methods are opening up many possibilities for more complex and better-understood materials. After creating these mechanisms the next step is to overcome the energy dissipation in these materials with for instance actuators. As stated by Bertoldi, this could lead to true smart materials.[33]. Another important factor in this is the scale of these materials, which varies from macro- to nanoscale as discussed in chapter 3.3.1.

5.3. Integrated materials

Many of the mechanisms shown in section 5.2, are functioning with conservative, passive work cycles. However, to create the asymmetrical behaviour, non-conservative work cycles and therefore, a form of actuation is necessary. Adding extra functionality to the unit cell of a material can be done in various ways, from using thermally responsive materials to fully autonomous robotic materials. This section aims to show these different levels of integration in metamaterials.
Field responsive materials will change their physicochemical properties as a response to their environmental conditions such as electric fields, magnetic fields, thermal gradient, light, pH, and Ionic strength [42]. As shown with Hydrogels, this field responsive behaviour can act as a way of actuation. These gels use the simple act of swelling or shrinking due to a change in their respective response field to create complex movements that can be used for locomotion and other purposes [43]. Another purpose for this field responsiveness is shape recovery or even transformation [44], [45].
Field responsive materials such as piezoelectric actuators can also be used as actuators in lattice structures that are controlled actively. A difference with materials that will respond to their environment, is that these could also be controlled at higher frequencies and with more complexity. In the case of Anibogu, a lattice structure was made consisting of local resonators that each contain an electromagnetic actuator that can extract energy from the system, making the system non-conservative [46]. Although this system contains actuators, the system is only reacting passively to its perturbations.
The next step is to actively control the properties of the material on a system level as shown in the system from Liu et al. [47], which is similar to [46], but now its properties are actively controlled through the actuator. Material vibration damping or even general spatial movement with one or multiple actuators and sensors with a central goal and computation are also seen in designs such as this pneumatic actuator [48].
While the above-described materials have an actively controlled property or movement, they are controlled from a central location and are therefore hard to scale up to an actual material. This is where

robotic or autonomous metamaterials could have a major advantage. While the size or function can still differ significantly, the key aspect is that sensing, computing and actuation are done locally for each unit cell and therefore create a certain autonomy for the material. An example can be a material consisting of a lattice of mini-robots that have been programmed to have a designed property such as reduced Poisson's ratios [49], or of course, the material from Brandenbourger et al. [17]. From this we can conclude that beyond passive materials, there are many gradations of integrated behaviour, requiring just a material type all the way to fully autonomous micro-scale robots. As this thesis aims to design an autonomous unit cell that could be combined into a robotic matter, it will be useful to investigate the used solution in the field of these fully integrated materials.

5.4. Manufacturing methods

As explained in section 3.3.1 and shown in figure 3.4, a smaller scale is only possible with new and improved production methods. These production methods often go hand in hand with the type and scale of material and this means any type of mechanism, actuator, sensor or even full assembly choice will have to be paired with a manufacturing method. In this section, the possible manufacturing methods and their characteristics are analysed. The mechanism will have a size in the millimetre range, which is therefore also the manufacturing scale that has been investigated. More conventional production methods such as Milling, lathing or even benchwork are not included in this chapter, but will not be excluded as potential manufacturing methods.

For all of these methods, it is important to note that not everything will be available to use for this thesis and therefore the concept choices will only regard production methods that are possible to use.

5.4.1. Additive Manufacturing

In the field of metamaterials, the scale and understanding at which things can be designed greatly surpass the knowledge about production at this scale and complexity. Developments in Additive manufacturing are decreasing this gap and enabling the design of smaller and more complex structures. There are many different Additive (3D Printing) methods, which have been listed below:

- **Extrusion (FDM)**
  This method deposits layers of molten filament (plastic mixtures) onto a substrate and in this way builds up a structure. Commercially available solutions have extrusion sizes up to 0.1 mm, limiting their level of detail. Advantages of this method are the fabrication speed, cost-effectiveness as well as the availability of different filament materials with for instance added metallic powders or mixtures [50]. Ref [51] showcases the possibility of decreasing the extrusion size to 80 µm.
- **Inkjet printing**
  Inkjet printing is a method that uses micron-sized nozzles to deposit droplets of ink in stacked 2D layers that are cured layer by layer, similar to conventional lithography/etching methods. This process is slower than FDM but can reach much higher accuracy levels. While it is possible to combine different materials into a print, the curing methods can be very different and therefore cause harm to a previous layer.
- **Vat polymerization**
  Vat polymerization is a collective name for methods that use a liquid photopolymer resin stored in a vat.
  Steriolithography (SLA) is the most common method, which is based on curing the resin layer by layer with UV light. The addition of for instance ceramic particles into the resin can lead to specific material properties. Layer thicknesses and resolutions are possible up to 10µm [52]. More practical is the example of the Formlabs Form 3 printer that is available at the lab of the UVA, which can handle resolutions of around 25µm [53].
  Multi-Photon polymerization (MPP) is another Vat polymerization technique, that only cures the material at the focal point of a Near-infrared (NIR) laser. Because of this local curing, the production can be truly 3D and allows for high freedom in designing at incredibly small scales up to sub-100-nm and is therefore highly promising for small scale metamaterials [54]. Structures containing metallic particles or even pure metals can be fabricated when using tricks in the fabrications such as thermal treatment. Through a very similar process called *direct laser writing (DLW)*,

Bauer et al. [27] have achieved incredibly high specific stiffness at low-density nanolattices.

There are many other 3D printing methods, such as *Laser chemical vapour deposition (LCVD)*, *Powder bed fusion* and *Aerosol jet printing*, which are promising, but currently not producing better or more interesting results than the above-mentioned methods. A comparison of additive methods against their lattice size constant is shown in figure 5.4

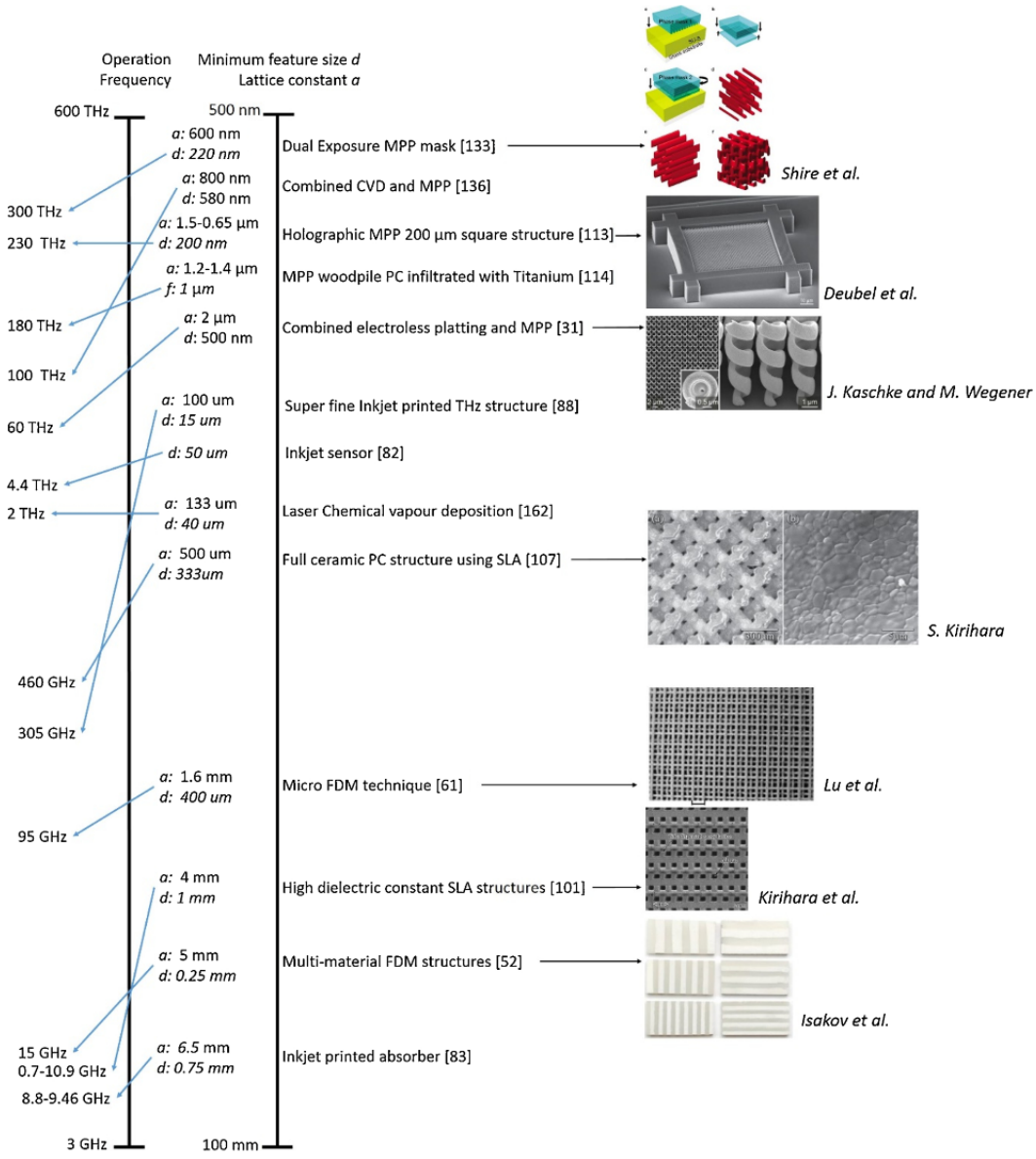

Figure 5.4: Structures created with additive methods sorted by lattice size as shown in [55]

5.4.2. Injection Moulding

Injection moulding is the process of heating particles of a material, usually plastic or rubber, and then injecting this into a mould. The cooled-down material then will have the inverse shape of the mould and with this, a geometry has been produced. Injection moulding works very well for producing micro-parts with tolerances in the range of 10-100 microns[56].

A challenge for injection moulding can be the need for venting in the mould as well as the production of the mould due to the high needed tolerances and therefore special required production methods. However, injection moulding could be a solution for using different materials or working with things such as thin walls that would fail on a 3D print.

5.4.3. Micro cutting

Next to 3D production methods, which focus on the addition of materials, the removal of material is an alternative production method that can be used for micro-scale manufacturing. Next to the previously discussed bulk machining, both laser and water jet cutting have been proven to work very well in 2.5D manufacturing at scales down to 4 micrometres [56]. An advantage of this removal process is that it is suited for a wide range of materials. Challenges that come with water and laser cutting such as cutting angles and material properties changing due to local temperature rises.
While macro-scale cutting is available widely at both university labs, micro-cutting is something that is only available at the TU Delft and requires further investigation before use.

To conclude, there are many potential manufacturing methods for producing a metamaterial. By comparing the required accuracy, material properties, duration and availability, the best production method can be selected for each component in the assembly of the unit cell. In Part II, the manufacturing methods that were selected for each component are discussed.

6

Subsystems

To successfully meet the set requirements and functions as detailed in section 3.2, subsystems such as actuators and sensors are needed. This section aims to highlight the essential components that are required for the full system to work and will discuss solutions for each of those subsystems.

6.1. Actuators

The implementations of odd elasticity that were studied in chapter 4, require an actuator that delivers this torque or force. In this section, suitable means of actuation are discussed. The limit cycles require relatively fast control at a micro-scale. Combined with the knowledge available in the research group, this search for an actuator will focus on electrical and electromagnetic actuation. Only DC Actuators have been considered to avoid the need for complex control systems.
From the design targets that were calculated in Chapter 3, a force target of $1.2\,N$ and stroke of $5\,mm$ have followed. These requirements will form the basis for selecting an actuator but could be changed due to factors such as cost, mass and manufacturing.

6.1.1. Electromagnetic

Electromagnetic actuators use magnetic fields and convert electrical energy into mechanical energy. Many of these actuators use the principle of Lorentz force: When a current-carrying conductor is placed in a magnetic field, it will experience a resultant force. The magnetic field could be created with a permanently magnetized material such as Neodymium, or an actively generated field by an electromagnet. There are many different applications of electromagnetic actuators such as rotational DC and AC motors as well as linear actuators in the shape of solenoids or Voice Coils.

$$\mathbf{F}_e = q\mathbf{E} = n\mathbf{I}\ell \times \mathbf{B} \tag{6.1}$$

When calculating the force that is acting on the current-carrying conductor, the above formula can be derived, where n is the number of conductors, I is the current in Ampere, ℓ is the length of the conductor in the magnetic field and **B** is the strength of the applied magnetic field in Tesla. It is important to note that the strength of this magnetic field is not only dependent on the strength of the source (for example the permanent magnet) but also the Reluctance of the magnetic circuit caused by for instance the air gap between the conductor and the source.
This Reluctance in the magnetic field causes a force in the air gap that works to close this gap, increasing quadratically with a closing gap. Both the Solenoid as well as the Reluctance actuator use this magnetic force instead of the Lorentz force.

DC Motor
A DC motor is a rotational motor that uses the current conductor in a magnetic field to cause a moment around an axis as can be seen in figure 6.1. There is a local equilibrium, where the conductor is exactly in the middle of 2 poles and once this has happened, the direction of the current can be changed, causing a new equilibrium position to occur which leads to a motion in the direction of the switching field. When switching fast enough and increasing the number of magnetic poles per rotation, a smooth rotation and torque can be created. The switching of the field can either be done by a control system, or through a commutator. Advantages of a DC motor are the unlimited stroke due to the rotation, low cost and high possible rotation speeds. Disadvantages are a low torque $[1e-3Nm]$ and the friction of a commutator and cooling issues when applying torque at low speed. An example of a small-scale DC motor could be [57]

Servo
A Servo motor is a DC motor but is now connected to a gearbox for higher torque. Next to this, as shown in figure 6.2, Servo motors usually have integrated control electronics for position control by using a rotation sensor. This means that for the odd elasticity, which is based on a force output, extra control or a simplification of the Servo motor is required. The advantages of servos are a high torque $[1Nm]$ and low cost due to applications in the RC industry [58]. A disadvantage is that the addition of a gearbox adds friction and backlash and that there is no direct method for force control.

Solenoid
Next to rotational actuators, there are also linear electromagnetic Actuators. As shown in figure 6.3, a solenoid is a combination of a coil that acts as an electromagnet, a ferromagnetic core that can slide in and out of this coil and a spring that pulls this core in the opposite direction of the force from the electromagnet. Once energised, the coil magnet attracts the core, also called a plunger, and pulls it out of the natural position with a reluctance force that is inversely quadratically scaled with the gap between the core and the magnetic field. Advantages of a solenoid are the low cost due to not needing a magnet and the high force close in its energised position. A disadvantage is a significantly lower force in its most outward position and the non-linear force to stroke relation [59].

Reluctance
Similar to the solenoid, a reluctance actuator is a linear actuator consisting of a coil and a ferromagnetic core (figure 6.4. The force in a Reluctance actuator is caused by an air gap in the magnetic circuit and is again inversely quadratically scaled with the length of this air gap. Due to the closed magnetic circuit except for the air gap that causes the force, a reluctance actuator is very efficient for small strokes and can reach very high force densities. Because this attraction force is only in one direction, a common setup is to place 2 opposing reluctance actuators. This could be beneficial, because now the peak force is highest at the extremes of the actuator strokes, matching the expected maximum demand from the odd elastic function. However, the main disadvantage is that it is an expensive actuator that is not readily available at this scale.

Voice Coil
A voice coil actuator uses a magnet and a coil that conducts a current through the magnetic field to create a Lorentz force. This force is dependent on the strength of the magnetic field and when the magnet and coil are equally long, the force will decrease proportionally with the out-of-centre position. However, when the coil is longer than the magnet (over hung) or vice versa (under hung), this effect is no longer present and the actuator has a constant force in a limited stroke. A disadvantage of the voice coil actuator is the need for a magnetic circuit and application mostly in the high tech industry, which increases the cost significantly [60].

6.1.2. Piezo
Next to electromagnetic actuators, it is possible to use piezoelectric materials, that are capable of creating electrical energy from mechanical stress and the other way around. A Voltage over the piezoelectric material is proportionally linked to the expansion of the material. There are methods to decrease the required voltage by stacking piezoelectric materials as well as mechanical amplifiers as shown in figure 6.6. However, even with this, the main disadvantage is the small stroke of the actuator $[\ 1e-5m]$ [61].

Using bending piezoelectric materials and coupling those to a mechanism that achieves large amplification of motion is something that has already been shown in small-scale robotics [62], [63]. This means that a potential mechanical design could allow for the required motion with the use of these piezo actuators, but this will need further design and investigation. Another disadvantage specifically for the odd elastic application is that the voltage is linked to a displacement and not a force, which would require a more complex control system.

6.1.3. Capacitance

Another method of actuation is through capacity, also called electrostatic actuators. This type of actuation is commonly used at a very small scale in the shape of Comb-drives (figure 6.7) and the force is inversely proportional to the gap between the two plates. While this method of actuation is easy to implement and has a low cost (At large production volumes), it is most probably not suitable due to the stroke range $[1e-5m]$ versus what is required in the unit cell [64]. A solution could be coupling many of these comb-drive actuators in series, resulting in a large stroke. However, this would require nanoscale production methods for unit cells that furthermore can be produced with much larger scale methods.

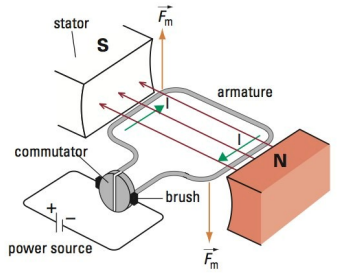

Figure 6.1: DC Motor [65]

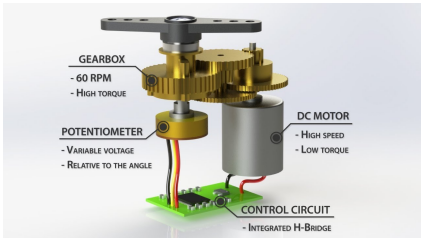

Figure 6.2: Servo Motor [66]

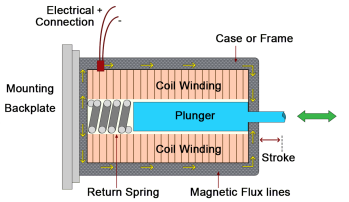

Figure 6.3: Solenoid Actuator [67]

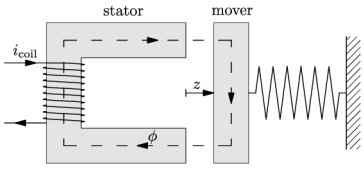

Figure 6.4: Reluctance Actuator [68]

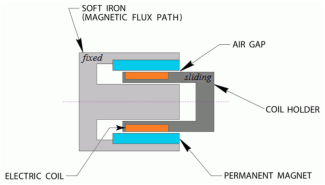

Figure 6.5: Voice Coil Actuator [69]

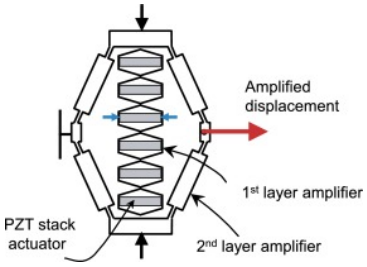

Figure 6.6: Amplified Piezo Actuator [70]

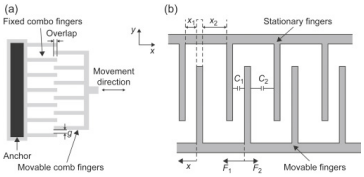

Figure 6.7: Capacitive Actuator (Comb Drive) [71]

6.1.4. Overview

In the previous subsections, multiple options have been considered for their working principle, advantages and disadvantages. To get a concrete overview of the potential specifications of these actuators, off-the-shelf solutions have been found and are shown in table 6.1.

From this table, it was concluded that the ideal rotational actuator would be a servo motor, which ideally would be changed to a force-controlled system. For a Linear actuator, a further comparison can be done between the Solenoid, Reluctance and Voice Coil actuators, where their force is compared over a stroke of 6 mm as shown in figure 6.8. These values are based on calculations based on various

Actuator	Actuation	Stroke	Peak Force order	Control method	Force/stroke relation
DC motor	Rotation	infinite	1e-3 Nm	Force Control	Constant
Servo	Rotation	360 degrees	1 Nm	Position Control	Constant
Solenoid	Linear	1 mm	1 N	Force Control	Quadratic inversely proportional
Reluctance	Linear	0.1 mm	10 N	Force Control	Quadratic inversely proportional
Voice Coil	Linear	1 mm	1 N	Force Control	Constant
Piezo	Linear	0.01 mm	10 N	Position Control	Constant
Capacitance	Linear	0.01 mm	0.01 N	Force Control	Linear inversely proportional

Table 6.1: Table with specifications of the various actuators

assumptions as explained in appendix A. From this figure, it shows that a Voice Coil actuator would be preferred, due to its constant force curve that is still high enough to deliver the required force. The choice between an off-the-shelf actuator and a custom design will be discussed in chapter 9.

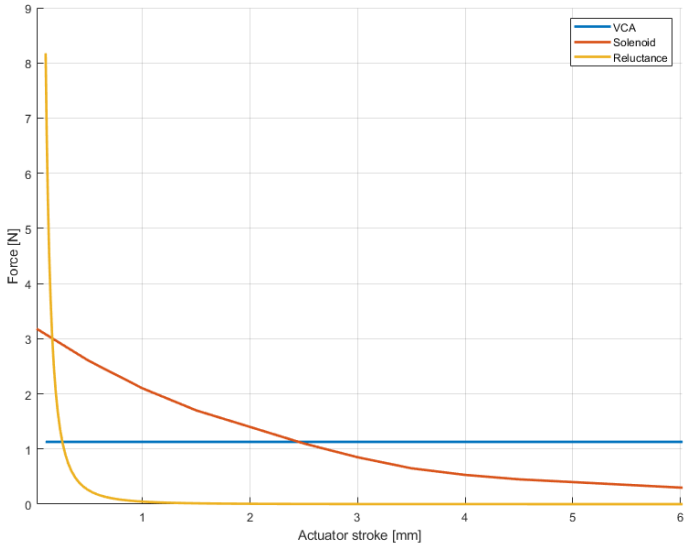

Figure 6.8: Comparison between Actuators force over their stroke range

6.2. Sensors

As explained in the functional analysis in chapter 3.2, a position measurement is needed for the odd elastic formula. This position measurement can either be angular or linear and, dependent on the method of actuation, it can be used directly or through extra calculations. Below, six methods for the measurements are discussed that should meet the requirements for the unit cell:

1. Measure a range of 5 mm
2. Allow for fast and accurate measurements
3. Measure locally to allow for autonomous unit cells
4. Minimize friction and therefore required energy of the system.

6.2.1. Hall effect

A hall effect sensor uses the Hall effect where the induced voltage over a current-conducting strip of metal due to a change in a magnetic field is measured. This method is commonly used in rotary position measurements, but can also be used for linear sensing. The main advantages of this sensor method are the low cost and available sensor packages that could directly be integrated into the electronics [72]. Next to this, the measurement is contactless and therefore does not add any friction. With the potential use of electromagnetic actuators, it should be investigated if the change in the field from these

actuators could distort the measurement. However, literature shows promising results for using a Voice Coil Actuator in this motion range [73], [74].

6.2.2. Encoder

An encoder uses a reader head that moves over a scale and in this way converts the position to a signal readout. These reading heads use many different methods such as optics, magnetic and inductive readings and can reach micrometre accuracy measurements level [75], [76]. The disadvantages of using encoders are the cost and size of these systems. Therefore, an encoder is only a suitable sensor option, when very high accuracy measurements are needed to achieve the odd elasticity.

6.2.3. Potentiometer

A potentiometer consists of a resistive element and a moving end terminal, leading to a linear relation between the resistance over the circuit and the position of the end terminal. Due to the low cost and easy electronic implementation, it is a widely used sensor method in things such as servos and user interfaces. The accuracy of a potentiometer is dependent on the quality of the resistor and other components and for potential off-the-shelf sensors smaller than 5% [77]. A disadvantage of using potentiometers is the contact resistance, which increases the required force for the actuator.

6.2.4. Capacitive

Through measuring the capacitive coupling, a capacitive sensor can measure almost anything moving through space that is either conductive or just has a different dielectric than air. One of the main applications of these technologies is the touchscreen in many of the phones produced today, but it could also be used as a position sensor in the unit cell. Through an electronic circuit, an oscillation can be generated in which the frequency is influenced by the measured capacitance, resulting in an accurate measurement. The advantage of a capacitive sensor is that by only needing a varying capacitance, it is easy and flexible to integrate into a unit cell as shown in the MetaSense sensors [78]. However, the fact that almost anything can be measured is also a big source of errors in the measurement. Moving components such as a human hand or even an electromagnetic actuator will cause significant measurement errors, especially without the presence of grounded shielding.

6.2.5. Strain Gauge

Similar to a potentiometer, a strain gauge works through varying resistance. In the case of a Strain gauge, a carefully designed conductive geometry is placed onto a surface. This geometry will deform together with the surface and through the deformation, the resistance of the strain gauge change, resulting in a measurement of the strain of this surface. While usually used to estimate the stress in a location, especially when coupled to a well-known surface, they can also be used for position measurement. When placed on a part that has significant deformation, such as the rotary springs in the unit cell, this could result in a position measurement. The main advantage of this strain sensor would be that there is no additional friction and there is no large space occupied by the sensor. The disadvantages however are the high cost of strain gauges, and their limited strain before breaking which is close to 5% [79]. Next to this, the deformation of the measured surface needs to be predictable and significant for a good measurement.

6.2.6. Self Sensing

Certain Actuator types such as piezo-electric and servo's are displacement controlled and therefore do not need an additional displacement measurement. Furthermore, even the force-controlled actuation methods have the potential for position measuring without the use of additional sensors. When looking at voice coil actuators or DC motors, an unwanted effect is the self-induction of the windings. An equation of the electrical circuit can be given by the following relation from [80].

$$V_{ss} = R_i I_a + L_i \frac{dI_a}{dt} + \alpha \frac{dx}{dt} \tag{6.2}$$

Where V_{ss} is the voltage measured over the coil terminals, R_i is the resistance of the coil, I_a is the current through the coil, L_i is the inductance of the coil, α is the motor constant and $\frac{dx}{dt}$ is the velocity of the actuator. By rewriting this equation and measuring both the current through the coil and the

terminal voltage over the coil, it is possible to then estimate the position:

$$x = \frac{1}{\alpha} \int (V_{SS} - R_i I_a - L_i \frac{dI_a}{dt}) \tag{6.3}$$

By starting at a known equilibrium position, a position measurement can now be known through the integration of the velocity [80]–[82]. The main advantage of this method is that it does not require any physical sensors anymore. However, the accuracy of this method is highly dependent on the magnitude of this voltage, which will decrease at lower speeds and thus might not be suitable for semi-static applications.

6.2.7. Overview

Now that various options for position sensing have been discussed, this section aims to create a comparison between them. Firstly the sensors should meet the criteria and from table 6.2, we can directly conclude that the Strain and Capacitive sensor ranges are expected to be too small for this application. Next to this, the high cost of the Encoder friction and low accuracy of the Potentiometer makes them not suitable for this application.
While the Self-sensing application would be ideal, further research should show if this is a viable solution. If not, the Hall effect sensor has proven in the literature to work in this environment and range and will be a good alternative.

Sensor	Working principle	Friction	Range	Accuracy	Cost
Hall effect	Change in magnetic field	Contactless	Medium	Medium	Low
Encoder	Chip reads indexed scale	Contactless	Unlimited	High	High
Potentiometer	Variable resistance moves with travel	Contact measurement	High	Low	Medium
Capacitive	Measure capacitive coupling	Contactless	Small	Low	Low
Strain sensor	Change in resistance due to change in geometry	No friction, but stiffness	Small	Medium	High
Self sensing	Measure induced voltage from actuator speed	-	Linked to actuator	Medium	Low

Table 6.2: Table with specifications of the various sensors

6.3. Control

In order to achieve the autonomous behaviour of each unit cell, a control system that converts the measurements into actuation is needed. Next to actively controlling, this system should also be able to be reprogrammed as stated in chapter 3.2. The exact specifications of this system are highly dependent on the specific type of sensor and actuator and therefore it has been chosen to only define a set of requirements for the control system:

1. **Read 3 signal inputs**, which can be done by reading voltages with potential additional circuits such as Wheatstone bridges for resistance measurement
2. **Control 3 DC actuators**, which can be done with pulse-width-modulation and potential additional feedback through a current sensor.
3. **Convert input to output**, which can be done with a microcontroller or other logic electronics.
4. **Allow for reprogramming**, which can be done by a physical connection, but ideally would be done wireless to allow for faster reprogramming of multiple unit cells.

Since the control electronics do not directly add to the value of this thesis project, it would ideally be outsourced and therefore, further research into the possible solutions has not been done.

6.4. Energy source

One of the criteria for odd elasticity is that it is a system that is not in equilibrium and therefore non-conservative. This means that a source of energy is required, which results in electrical energy. When looking at the specifications of the actuators, it can quickly be noted that the peak power requirements per actuator of the system are relatively high for the size of the system. For the final system, the maximum power can be approximated:

$$P = I^2 * R = 0.5^2 * 3.2 = 0.8Watt \tag{6.4}$$

Due to the autonomous nature of the unit cells and the fact that in a final application there would be a large number of unit cells, the energy source would ideally be situated within the unit cell. Local energy source would allow for an almost infinite scaling of the system but is far from trivial. The storage of this energy is a challenge, which could be solved for instance with a micro-scale lithium polymer cell. However, when looking at cells of this scale, their energy density is around $0.1\frac{Wh}{g}$ [83], [84]. This means that the full power action of 3 Actuators can endure for:

$$t_{fullpower} = \frac{E[\frac{Wh}{g}]}{P[w]} * 3600 = \frac{0.1}{(3 * 0.8)} * 3600 = 150[\frac{s}{g}] \tag{6.5}$$

Next to storing this energy, it should also be generated in a way. This could be done in multiple ways such as harvesting it from the mechanical inputs into the material, charging it conventionally or even using small solar panels [85]. In the Netherlands, the maximum power from a solar panel per area is close to $200\,W/m^2$ [86]. From chapter 3, we know that the design targets result in close to 800 unit cells per m^2 and therefore, $P = N_{units} * P_{Unit} = 800 * 0.8 = 640W$. From this, we can conclude that even when covering the full surface of the material with solar panels, there will not be sufficient power. However, it could be used to charge up energy storage.

An alternative to storing the energy locally is to use an external power source, which could be lighter and less complex. The disadvantage of this method is that now the number of unit cells can no longer be scaled infinitely and even at small numbers of unit cells, there are constraints with wiring. However, due to the number of challenges with the other subsystems and this energy source not having a direct effect on the odd elastic behaviour, the new unit cell will work on external power.

7

Conclusion

By investigating the solutions of each subsystem, the literature review has been concluded. Firstly, the relevance of research into a metamaterial with odd elasticity was explained. It became clear that to achieve odd elasticity, a lattice structure consisting of a periodic pattern of unit cells with non-reciprocal couplings is needed. These couplings can be made with a combination of normal and odd springs in many possible layouts. After this, the current system from Brandenbourger et al. [17] has been analysed. Building on the work of [17], the simulations from [20] show that large lattice structures with odd elasticity show interesting dynamic behaviour which could lead to things such as crawling or rolling on a macroscale.

However, the current setup has its limitations and to allow for future experiments with lattices consisting of many unit cells design improvements are necessary. this resulted in the following research goal:

The design, manufacturing and testing of a mesoscale, 3 DOF unit cell with odd elasticity caused by active closed-loop control and actuation. This unit cell should be as small, strong and light as possible while meeting all other set requirements.

With this goal and accompanying design targets, a targeted literature study was done for finding out the best solutions for achieving the odd elasticity, mechanism design and manufacturing methods and lastly each subsystem.

7.1. Concept choice

Based on the system design targets that have been summarized in table 3.1 solutions were found for all subsystems in the previous chapters and they are combined in table 7.1. This concept will then be transformed into an actual design and finally, a real-life testing platform as explained in Part II and III.

System	Solution
Mechanism	Modular Compliant 3D printed hexagons
Active Unit cell layout	Divided Actuation
Actuator	Voice Coil Actuator
Sensor	Hall effect sensor or self sensing
Control	Custom local control board for each 3 hexagons
Power	External power source

Table 7.1: Table with concept choices for each subsystem

Part II

Design and manufacturing

8

Mechanism

During the literature review, the requirements for the system were defined (table 3.1) and a final concept was chosen (table 7.1). The next step in the design process is to convert these choices and requirements into a working design that can be produced and used to acquire experimental results. In the coming chapter, the design of the unit cell is explained in 3 sections. First, this chapter will explain the Mechanism design, which creates the passive stiffness and acts as the mounting frame for the full system. After this, the design of the actuator that makes the system active is explained. Finally, the control system design is explained, which is a combination of electronics and software.

After further research, it was noticed that the required actuator force of $0.78N$, which would be required for static deformation of $2.5\,mm$ is not possible for a system that weighs only 5g in total. However, the 5 mm stroke is most important during the limit cycle, which occurs at the resonance frequency and therefore could be amplified due to the resonance peak. Taking a Q-factor of the flexure that is close to 4.5, reduces the static deformation to $1.25\,mm$. During the limit cycles, this Q-factor leads to the full $5mm$ (10%) stroke. This requirement change reduces the required peak actuator force of 0.38 N. As will be explained in chapter 11, the final Q-factor was even higher for a single hexagon, meaning that even less force will be required during the limit cycle.

Next to the requirements as defined in table 3.1 and being a mounting frame for the individual components, there are some optimization targets for the mechanism as well:

1. **Low mass**: A lower mechanism mass will allow for a higher mass budget for the actuator and probably a higher force.
2. **Low damping**: The limit cycle will occur at the resonance frequency of the system. Therefore, lower damping (Resulting in a higher Q-factor) will decrease the amount of work needed from the actuator to create a certain cycle amplitude.
3. **Ease of manufacturing**: By scaling down the unit cell, the final goal is to allow for a lattice with many unit cells. Therefore, it should be easy and fast to produce to allow for mass production.
4. **Modularity**: The design should be made modular so that the number of unit cells in the lattice can be varied without changing the design.

8.1. Passive unit cell

By choosing the divided actuation concept, the unit cell consists of 3 hexagons, actuators and a central control board. However, the passive structure of a honeycomb lattice can be divided into much smaller sections. Therefore, this report will specify this smaller section as the Passive unit cell and the larger unit cell will be called the Active Unit Cell.

Whilst it is possible to choose many different unit cells for a honeycomb lattice, it was decided to build up the lattice as shown in figure 8.1. The reason is that in this way, it is possible to create the connection

between unit cells in the rigid links and therefore it is easier to make the flexure joints compliant, which removes friction and allows for 1 piece production.

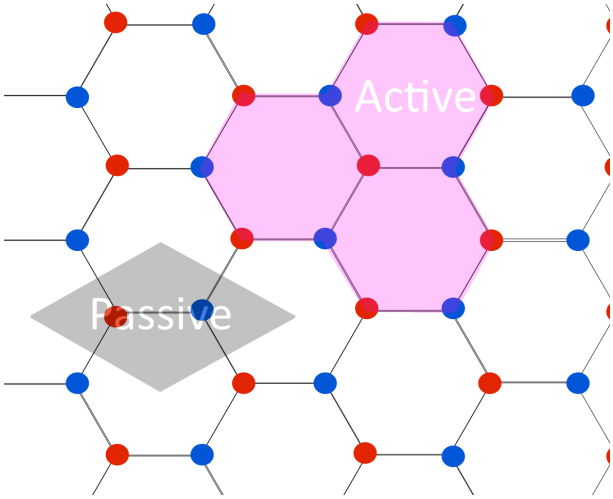

Figure 8.1: Visualization of the passive (Grey) and Active (Pink) Unit cell

8.2. Active unit cell

As explained in the previous section, the active unit cell consists of 3 hexagons with each an actuator and the control board. To clarify the difference between the active and passive unit cell, both are shown in figure 8.1. It is important to note that from a purely theoretical perspective, the unit cell could also be described as shown earlier in this report in figure 4.6. While in simulations this shape can be distributed periodically with great ease, a real-life version would be highly unpractical. Therefore, the 3 hexagons will be described as the active unit cell. When mentioning just unit cell in other text, this also refers to the active unit cell.

The active unit cell layout is explained in the list below. A schematic layout is shown in figure 8.2.

- **Passive unit cell**: Rigidly connected to other passive unit cells.
- **Actuator**: Connected diagonally at 2 sides of the hexagon. Connection should allow for rotation.
- **PCB**: Control electronics board should be mounted rigidly in between 3 hexagons. Through flexible wire connections, it will be possible to control the actuators without the need for a flexible mounting of the board.

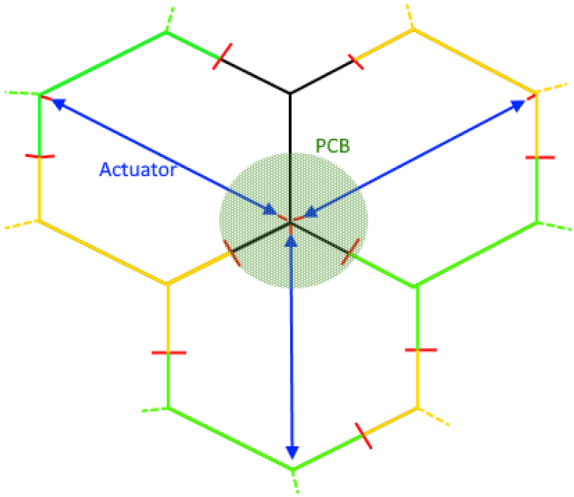

Figure 8.2: Schematic layout of the active unit cell

8.3. Pseudo-Rigid-Body-Modelling

The passive stiffness can be initially calculated with Pseudo-Rigid-Body-Modelling (PRBM) to get an initial estimate. In this method, 2 rigid bodies with a torsional spring in between are used to predict the behaviour of a compliant flexure, which allows for quick calculations to determine the starting point for more in-depth Finite Element simulations. Figure 8.3 shows a comparison between the real flexure and PRBM approximation.

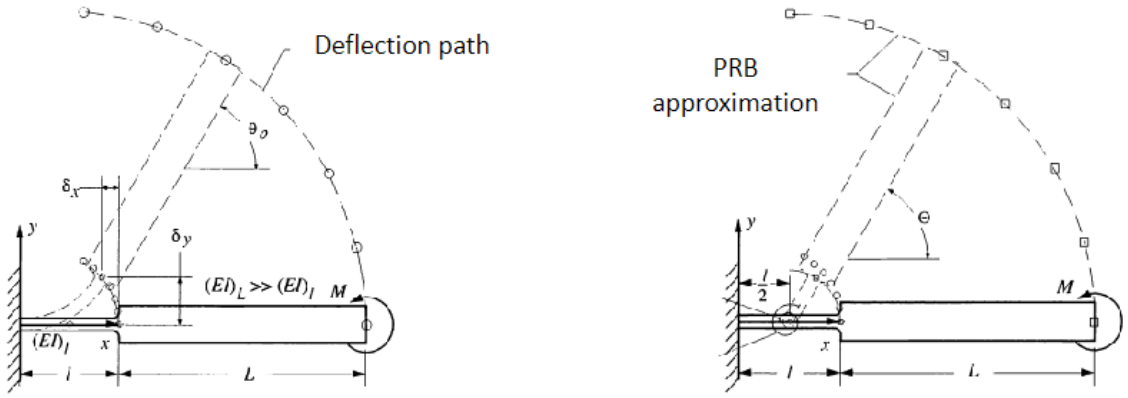

Figure 8.3: PRBM Modelling for small length flexure [87]

For flexures that are significantly shorter than the arm length ($L \gg l$) and a rectangular profile, it suffices to use:

$$k = \frac{EI}{L} = \frac{Ehb^3}{12L}$$

Where $E[Gpa]$ is the youngs modulus of the material, $I[mm^3]$ is the Area moment of inertia of the rectangular profile with a height of $h[mm]$ and a thickness of $b[mm]$ and a flexure length $L[mm]$.

By rewriting this formula and combining it with a flexure thickness of $b = 0.2\,mm$ a height of $h = 10\,mm$ and a flexural modulus of $1.4\,Gpa$, the required flexure length can be calculated:

$$L = \frac{Ehb^3}{12k} = \frac{2.1023e-05}{k} = \frac{1.4153e-05}{5.07\text{e}-3} = 1.84 \text{ mm}$$

These flexure parameters are used as a starting point for the 3D design of the actuator. This 3D Design also contains all other features that will be explained in the next section.

8.4. Detailed Design and simulation

Firstly, this conceptual design was transformed into an actual design as shown in figure 8.4. The rigid connections are done by bonding keyed connections together. For the Actuator connections, a flexure that allows for rotation around the in-plane axis is added between the connection and the passive joint.

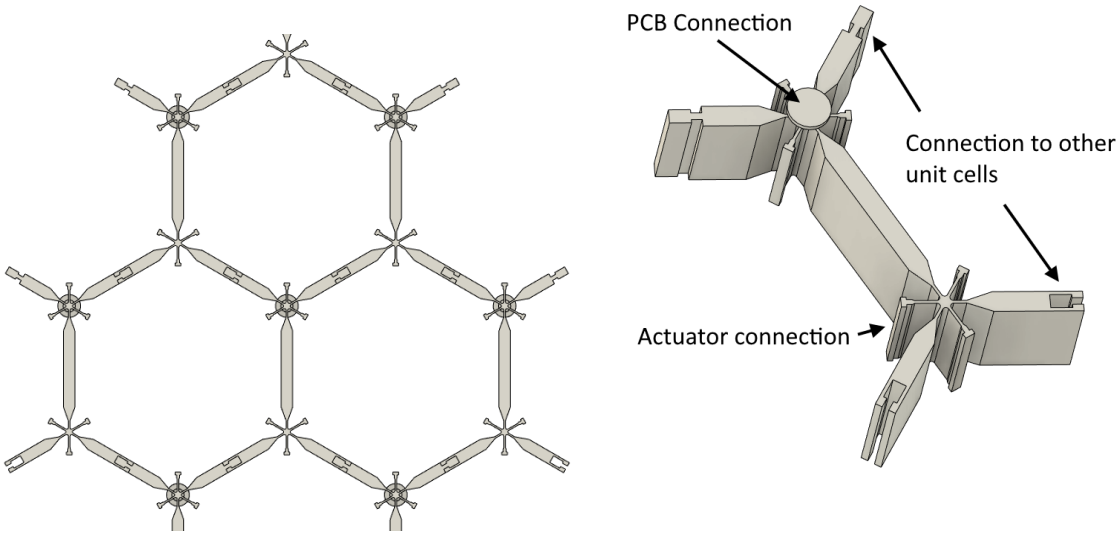

Figure 8.4: Detailed design of passive unit cell [87]

Because of the low stiffness target for the flexure, it was decided to use a Stereolithography (SLA) Printer (Formlabs 3). With this technology, a low stiffness and high strain material can be combined with high accuracy and very small wall thicknesses. The disadvantage of this material is that it has strong viscoelastic effects as will be explained in the next section.

Simulation of the stiffness of the passive hexagons was done with a 2D Finite element simulation in COMSOL as shown in figure 8.5. and this showed a stiffness of only $46\,N/m$ at a maximum stress of $12\,MPa$ (41% of the yield stress). The stiffness is only 60% of the expected value, which can be partially explained by the fact that other parts are not strictly rigid. Since these will also bend slightly, the overall stiffness will decrease. PRBM is also a method used for an initial estimate and might not translate perfectly to this specific problem.

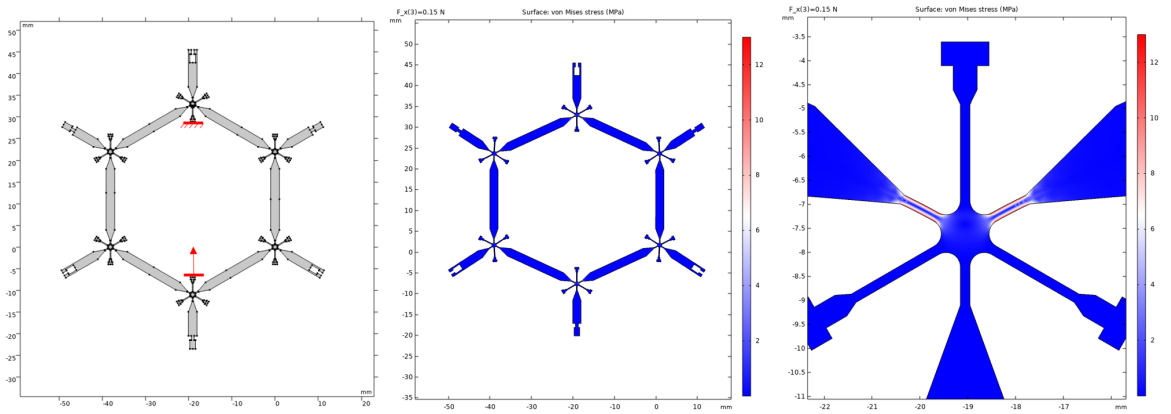

Figure 8.5: COMSOL FEM of passive unit cell consisting of 3 passive unit cells

8.5. Manufacturing

As explained previously, the production of the passive unit cells is done with an SLA printer. This printer uses a laser and a chain of mirrors to control its beam to cure a resin layer by layer. With a minimum wall thickness of 0.2 mm and a positioning accuracy of 25 µm, this production method is ideal for creating the low stiffness passive unit cell at a high level of repeatability. The full building process consists of the following steps as shown in figure 8.6

1. Printing parts.
2. Washing parts with IPA.
3. Post curing parts in UV Light.
4. Post-processing parts and assembly of the active unit cell through bonding

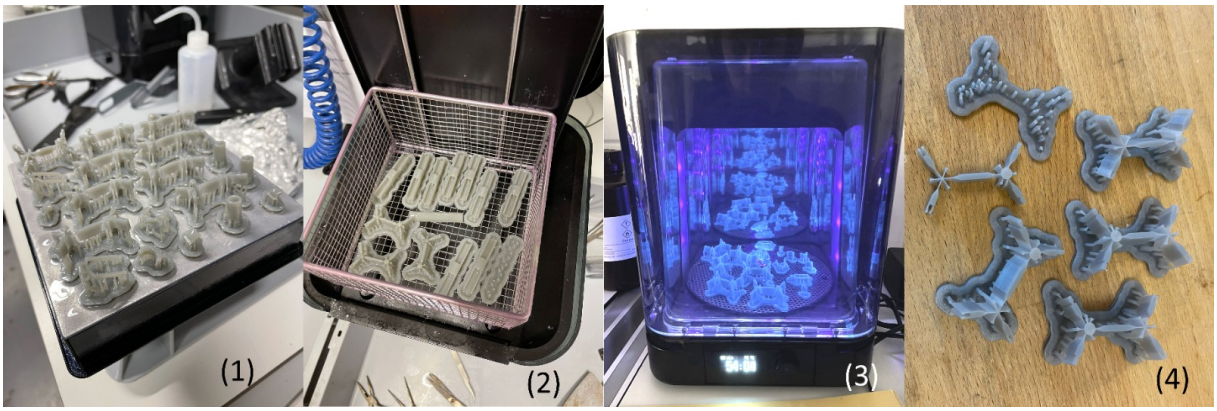

Figure 8.6: Production steps, numbered to match the enumeration above.

8.6. Experimental results

Whilst the PRBM and FEM have provided initial estimates of the flexure stiffness, it was important to validate this stiffness through experimental testing. By using a Tensile tester (Instron 5943) the material was characterised. In order to test the stiffness and damping over the full range, a profile was generated that can generate a full hysteresis curve. Figure 8.7 Shows the tensile testing setup, the response over time and a hysteresis curve. Here, the middle plot shows the force (left Y-axis) and Strain (right Y-axis) over time. Combining the two results in the right-side plot shows the hysteresis due to damping. Both plots show the results for a strain rate of $0.0167\,mm/s$ and $5\,mm/s$.

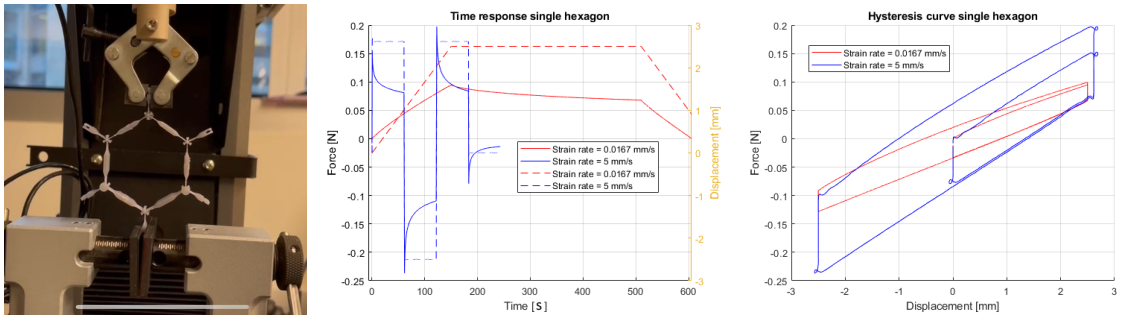

Figure 8.7: Tensile testing; Left a picture of the test setup, centre the time response and on the right the hysteresis curve.

8.6.1. Static response

The average stabilized stiffness is $31.8\,N/m$, which is only slightly below the expected stiffness from the FEM ($46\,N/m$). However, by using a digital microscope, the flexure thickness was measured and found to be close to $0.27\,mm$ instead of $0.2\,mm$. When correcting the FEM Model for this, the expected stiffness would be $88\,N/m$ and the measured stiffness is therefore only 42% of the FEM results.

This stiffness difference can be caused by many factors such as curing errors, not representative Resin data or others. By testing other flexure lengths, it was possible to validate that this 42% offset was consistent and therefore it was decided to change the flexural modulus from $1.4\,GPa$ to $0.58\,GPa$ for any further modelling.

8.6.2. Dynamic response

The hysteresis curve from figure 8.7 shows a significant difference between the material response at very low strain rates and higher strain rates, which is caused by Viscoelasticity. Polymeric materials show both elastic behaviour like a Hookean solid and a viscous response like a fluid, which together is called Viscoelasticity [88].

This strongly non-linear material response is not only strain-rate dependent but also time-dependent as shown in figure 8.7. From $t = 150\,s$, the strain remains constant, but the stress level changes. In an attempt to characterise the stress-relaxation of the material, the hexagon was given a step input of strain. The expression of stress relaxation as shown in equation 8.1 was fitted to the step response, where σ is the stress at time t, σ_0 is the initial stress τ_m is the *Maxwell's Time Constant*.

$$\sigma = \sigma_0 \exp -t/\tau_m \tag{8.1}$$

From this fit, the *Maxwell's Time Constant* is $\tau_m = 3.16\,s$, which is a significantly higher time constant than the period of the expected limit cycle ($T = \frac{1}{f_n} = \frac{1}{19.1} = 0.052s$. It is not clear if the material properties will actually have time to change during the cycle. In order to model the viscoelastic response of a material, various models can be used, which all use a configuration of springs and dampers in series as well as parallel.

Furthermore, there are more complex models that can be used to model the response of a viscoelastic material to an oscillation, which is the sum of both the instantaneous modulus of the elastic response E' and the inelastic viscous dissipation E'', which has a phase delay of $90°$. However, it is very complex to define these material properties from measurement and to predict the frequency response from them in a model.

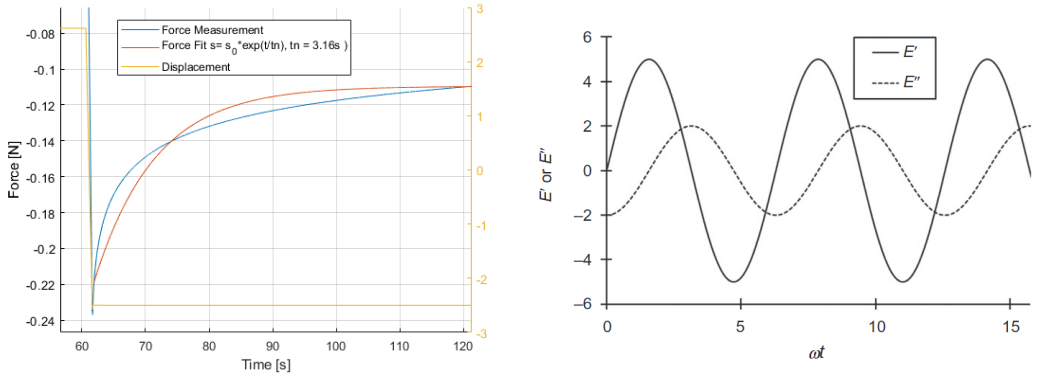

Figure 8.8: Left the stress relaxation and fitted maxwell's time constant. Right, the dynamic visco-elastic material with a phase delay between E' and E''.

Due to time constraints and limited available data, a more practical approach was used by describing the material bulk properties as a function of strain rate based on tensile testing data. These properties are the stiffness $K = f(\dot{x})[N/m]$ and Damping $C = f(\dot{x})[N/m]$. Figure 8.9 shows how the force strain relation gives information about the damping and the varying stiffness. These properties can be used to compare different flexure designs in the early stage of the design. After converging to a final flexure design, the frequency response of a full hexagon and actuator combination was experimentally determined in chapter 11.

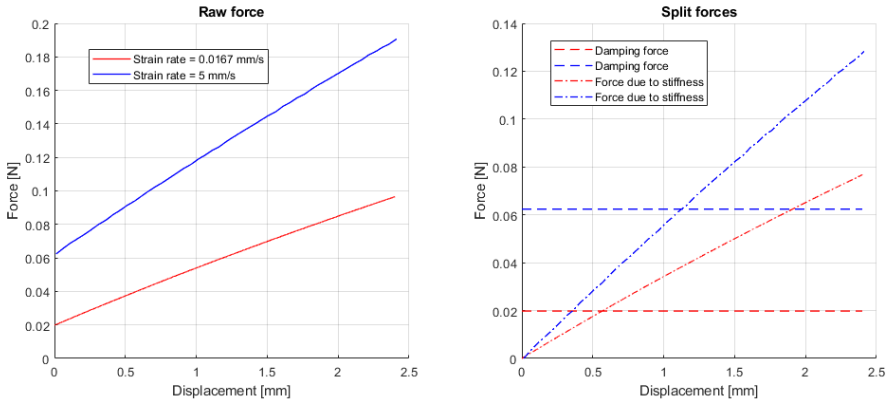

Figure 8.9: Left the raw force in the used data range and right this force split into a damping and stiffness force.

In order to then understand the relation between these properties and the strain rate, a strain rate sweep was done in the range from 0.5 mm/s to 20 mm/s, which was the maximum speed of the tensile test machine (Instron 5943). Figure 8.10 shows the resulting coefficients for this sweep. A fit for $f(\dot{x}) = a{*}v^b$ has been used to create the mathematical expression that then can be used to predict the damping (equation 8.4) and stiffness (equation 8.3) for any strain rate.

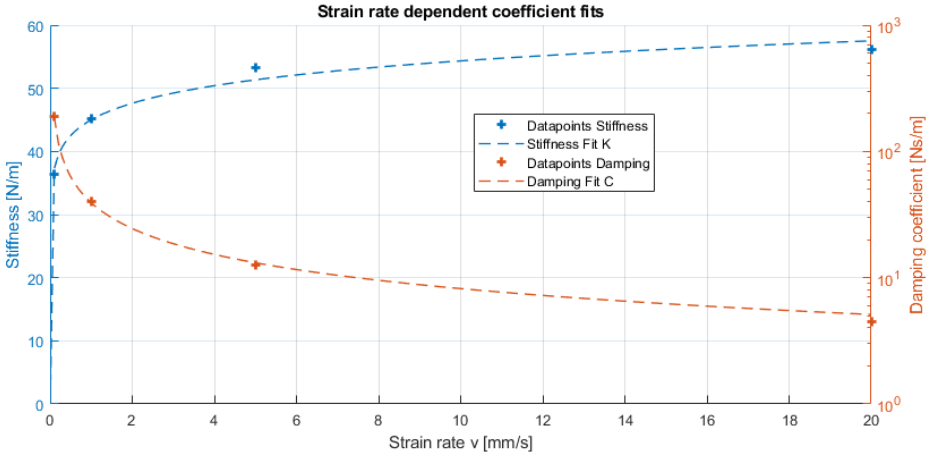

Figure 8.10: Data points with calculated coefficients for varying strain rates and their quadratic fit.

By using this fit, we can also extrapolate and find the expected damping and stiffness for the limit cycle. Since this cycle will have a sinusoidal shape at approximately $20\,Hz(40\pi\,rad/s)$ and a peak-to-peak amplitude of $5\,mm$, the maximum strain rate and the corresponding coefficients can be estimated. By measuring the step response of multiple hexagons, it was found that the most accurate method for estimating the coefficients with the peak strain rate. This was done by calculating the peak strain rate as shown in equation 8.2 and using this in the fitted functions 8.3 and 8.4:

$$x(t) = 2.5e-3 * \sin(40\pi * t) \rightarrow \frac{\delta x(t)}{\delta t} = \dot{x}(t) = 314e-3 * \cos(40\pi * t) \rightarrow \dot{x}_{max} = 314\frac{mm}{s} \tag{8.2}$$

$$K_{strain} = 45\dot{x}^{0.082} = 72.1\,N/m \tag{8.3}$$

$$C_{fit} = 39.25\dot{x}^{-0.68} = 0.79\,Ns/m \tag{8.4}$$

Mass spring damper system
By combining the stiffness and damping of the 6 identical joints, it is possible to simplify the single hexagon into a 1D system consisting of a mass, spring and a damper. Now that we have characterised the stiffness and damping coefficients and we know the mass target, it is possible to have a first estimation of the frequency response of the first mode of the hexagon. Both the resonance frequency and the damping ratio have been calculated through this method:

$$\omega_n = \sqrt{\frac{k}{m}} = \sqrt{\frac{72.1}{5e-3}} = 120\frac{\text{rad}}{\text{s}} = 19.1 \text{ Hz} \tag{8.5}$$

$$\zeta = \frac{c}{C_c} = \frac{c}{2m\omega_n} = \frac{0.79}{1.2} = 0.658 \tag{8.6}$$

The expected resonance frequency matches the design target, but during the limit cycle, the expected amplitude as calculated from equation 11.1 will only be approximately equal to the static deformation. This means that a higher actuator force would be required to reach the maximum amplitude during the limit cycle.

Iteration
A smaller damping ratio will cause a larger wave amplitude for the limit cycle for the same actuator force. Therefore, a smaller damping ratio will enable the design to use a smaller actuator or a higher flexure stiffness, increasing the performance of the system. In order to maximize this, multiple single hexagons were tested with varying flexure thickness and lengths. This converged towards a flexure design with significantly longer flexure joints of $3\,mm$ long, but with a larger flexure thickness of $0.35\,mm$. Whilst the stiffness at $314\,mm/s$ is very similar, this decreased the expected damping ratio to only 0.265, which would result in a 1.95-times higher cycle amplitude compared to the static deformation.

$$\frac{H_{peak}}{H_{static}} = \frac{1}{2\zeta\sqrt{1-\zeta^2}} \tag{8.7}$$

8.7. Final design

In this chapter, the passive unit cell was defined and an initial choice for compliant flexure design was made. After experimental characterisation of this flexure, it was concluded that visco-elasticity has a significant effect on the material properties and changes needed to be made. This resulted in a final design with the following specifications.

Parameter	Value
Printed Flexure thickness (Model)	$0.35\,mm\,(0.2\,mm)$
Flexure length	$3\,mm$
K(v) at 314 mm/s	$49.4v^{0.0687} = 73.3\,N/m$
C(v) at 314 mm/s	$26.1v^{-0.77} = 0.312\,Ns/m$
Flexure mass	$1.87\,g$
Natural frequency	$19.2\,Hz$
Damping ratio	0.265

Table 8.1: Table with the final design specifications of the passive unit cell.

As will be explained in chapter 11, the actual Damping ratio during oscillation was found to be significantly smaller at 0.1 However, the initial estimations have proved to be a useful tool in estimating the performance and optimization of the passive unit cell.

Figure 8.11 Shows the cad design and the produced passive unit cells combined into a honeycomb lattice. The mass of this flexure was higher than initially estimated, but due to time constraints, it was decided to not further optimize the flexure mass. The design has been used as the passive unit cell for all further experiments such as the single hexagon, unit cell and even full lattices.

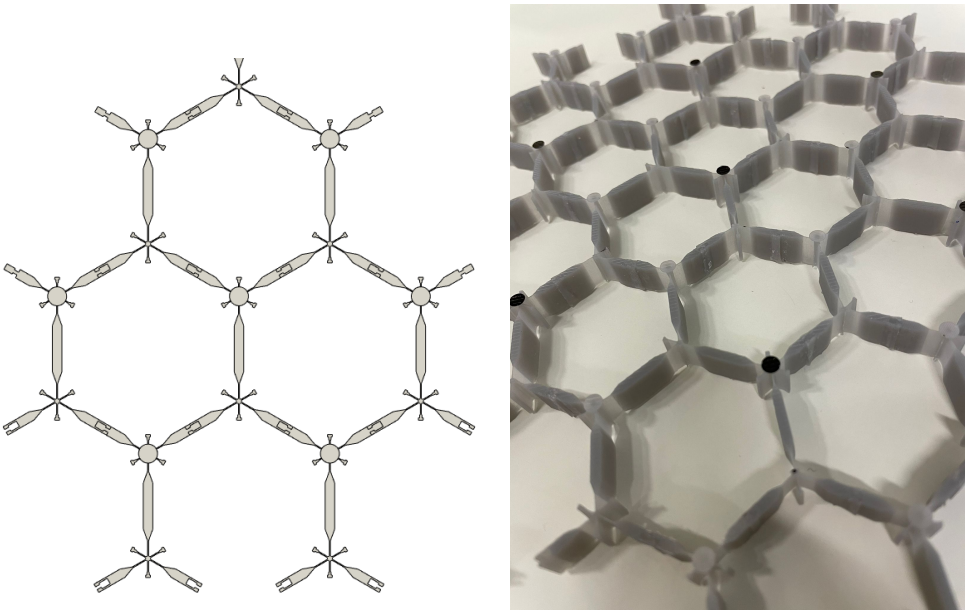

Figure 8.11: The final passive unit cell: Left a top view of the CAD design and right the produced version.

9

Actuator Design

As discussed in chapter 7, a voice coil actuator was chosen as the method for actuation. This chapter aims to explain the full design process for the actuator. First, the reason for making a custom actuator will be explained. After this, the design and production methods will be explained with the following sub-chapters: The electrical circuit, the magnetic circuit and the compliant flexure design. Finally, the experimental characterisation and validation will be discussed.

In chapter 3.4.1, the requirements were summarized in table 3.1. However, as stated in chapter 8, the peak force requirement decreased to $0.38\,N$ due to the expected resonance peak.

9.1. Custom design

The goal of this thesis project is to create an improved unit cell design that is able to achieve odd elasticity. The improvements are making the unit cell smaller, scalable and have an increased strength-to-weight ratio Δ. It is crucial to maximize the force density $[N/Kg]$, in order to maximize Δ. The first step in this process was searching for off-the-shelf actuators that fulfil the actuator requirements. For this, some candidates were found and they are summarized in table 9.1

Requirement	Target value	Thorlabs VC063/M [89]	H2W Technologies NCC02-07-001-1RH [90]	Moticont LVCM-010-013-01 [91]
Force	$0.38\,N$	$0.63\,N$	$.89\,N$	$0.28\,N$
Stroke	$5\,mm$	$6.3\,mm$	$5.1\,mm$	$6.4\,mm$
Mass	$< 5\,g$	$14\,g$	$18\,g$	$6\,g$
Maximum dimension	$< 30\,mm$	$22.6\,mm$	$19.1\,mm$	$20.7\,mm$
Price	$<$ €$30,-$	€$121,12$	Unknown	€116.5

Table 9.1: Table comparing off the shelf voice coil actuators to the design targets.

Of these candidates, the Moticont actuator is closest to the design targets due to its lightweight design. However, looking in further detail at this actuator, the maximum force at the extremes of the stroke drops significantly to 0.17 N, which is significantly below the requirements. Next to this, the price tag of €116.5 is too high for a scalable design that in future research can consist of more than 100 actuators. Important to note is that all of these actuators do not have any built-in linear guidance, which should be integrated and still fit within the hexagon. Since none of the off-the-shelf actuators match the requirements, the decision was made to design a custom actuator and focus on maximizing the specific force $[N/Kg]$

9.2. Coil design

Consisting of only a magnet, a soft iron core and a copper coil, voice coil actuators are not the most complex systems. However, for the actuator design to work correctly, three disciplines have to be perfected:

1. The electrical coil

2. The thermal behaviour
3. The magnetic circuit

In order to reduce the design complexity, the initial plan was to use an off-the-shelf coil as a starting point. This coil had an inner diameter of $D_{C,in} = 8\,mm$, outer diameter of $D_{C,out} = 10\,mm$ and a length of $L_c = 6\,mm$. Based on these coil dimensions, the magnetic circuit was designed.

During a later stage in the design process, it became clear that the selected coil was not available for delivery, requiring a custom coil instead. This was initially solved by manually winding the coils at the TU Delft, but after the first experiments, a large batch of custom-made coils was ordered from JH Coils in China. These coils consist of 150 turns of insulated single strand wire with a diameter of $0.18\,mm$. This wire thickness and number of coils were chosen to achieve a resistance of 3.2Ω. With this resistance, a maximum current output of $1.56\,A$ can be achieved by the control board through its $5V$ Motor drives.

In order to define the maximum current of the coil, the stabilized temperature was defined for a sweep of current magnitudes. Since we know that the resistance of copper increases with $1.00386\Omega/°C$, it is possible to estimate the average temperature rise of the coil. Next to stabilized temperatures, a further experiment was done to define the maximum time for higher continuous currents until a maximum temperature rise of $50°C$ was achieved. Both results are shown in figure 9.1 and from this, it was concluded that a maximum continuous current of $0.44A$ is allowed. For the expected sinusoidal set-points during the limit cycle, this means a peak current of $0.61A$ to achieve $0.44A$ RMS. In the future, this method could be repeated with an improved setup that includes a temperature sensor to validate the results.

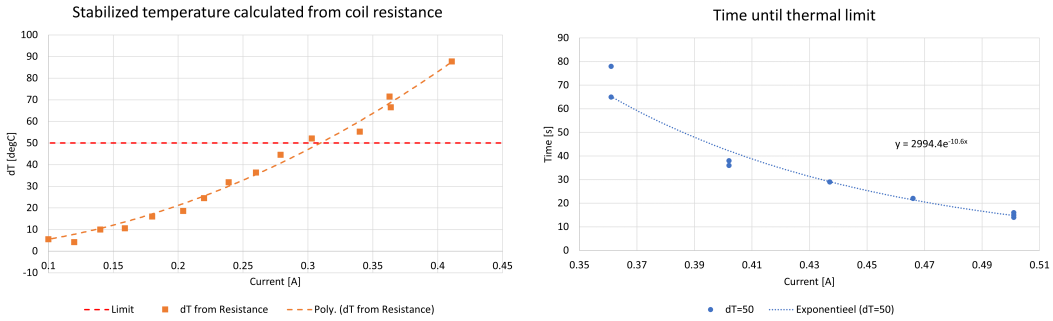

Figure 9.1: Thermal performance of Actuator coil based on coil resistance

9.3. Magnetic circuit design

The next step in the design process was to design the magnetic circuit. For this, first, the magnetic circuits from off-the-shelf actuators were analysed. As shown in figure 9.2, the magnetic circuit consists of a hollow soft iron cylinder with a magnet mounted on the inside. Between the magnet and the cylinder, there is space for the coil to slide in the actuation direction. The placement of the magnet is not always the same, but the goal is always the same; Maximize the amount of magnetic flux through the air gap and therefore through the coil windings. A higher flux density results in a higher Lorentz force and therefore a higher actuator efficiency ($\eta = \frac{F*V}{U*I}$). In order to achieve this, the following things are done:

- **High permeability iron:** Reducing the reluctance and therefore increasing the flux density.
- **Strong radial magnets:** Magnets with the correct field direction and a high remanent flux density.
- **Small air-gap:** Reducing the reluctance of the magnetic circuit and again increasing the flux density.
- **Avoiding magnetic fringing:** Making sure that the intended magnetic flux path is also the path with the lowest overall reluctance. In this way, the leakage flux is minimized and therefore, the flux density increases.

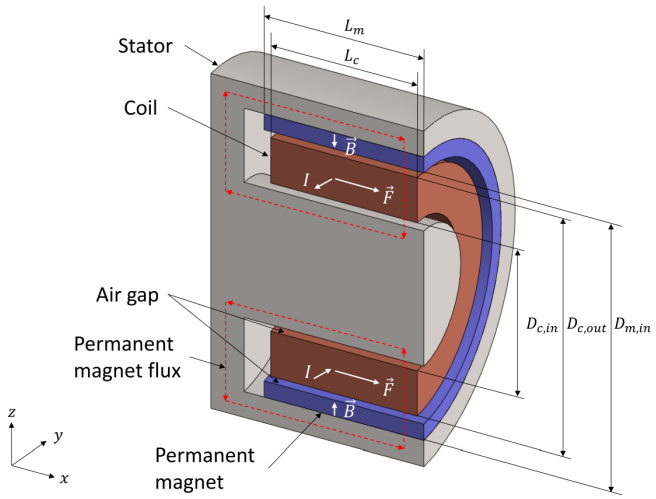

Figure 9.2: Section view of a voice coil actuator, including flux, current and resulting force directions. [92]

9.3.1. Magnetic core

The drawback of maximizing the actuator efficiency is an increased mass. While the electrical coil only has a mass of $1\,g$ and the magnet would have a mass of $2\,g$, a custom core is expected to have a mass of $9\,g$. Next to this, the complexity of machining this component would add significant costs. To compare the specific strength of an actuator with and without a core, a 2D axis-symmetric Comsol model was used as shown in figure 9.3. This simulation model is very simple and does not take into account the magnetic field from the coil, saturation of the magnetic core and any 3-dimensional side effects. However, it is a good initial estimate and due to its fast solving helps with fast design iterations. This model uses a magnetic permeability of 5000, and an air gap of 0.3 mm.

The simulation results as shown in table 9.2, show that even though the field strength and force are much higher for the actuator with core, the specific force is almost identical. This force density was calculated as $F/m = N * I * L_w * B_g = 150 * 0.6 * 0.028 * B_g$, where B_g is the field strength $[T]$ through the coil. Due to the added complexity and volume of the magnetic core, without significant additional actuator force, it was decided to design a largely coreless actuator.

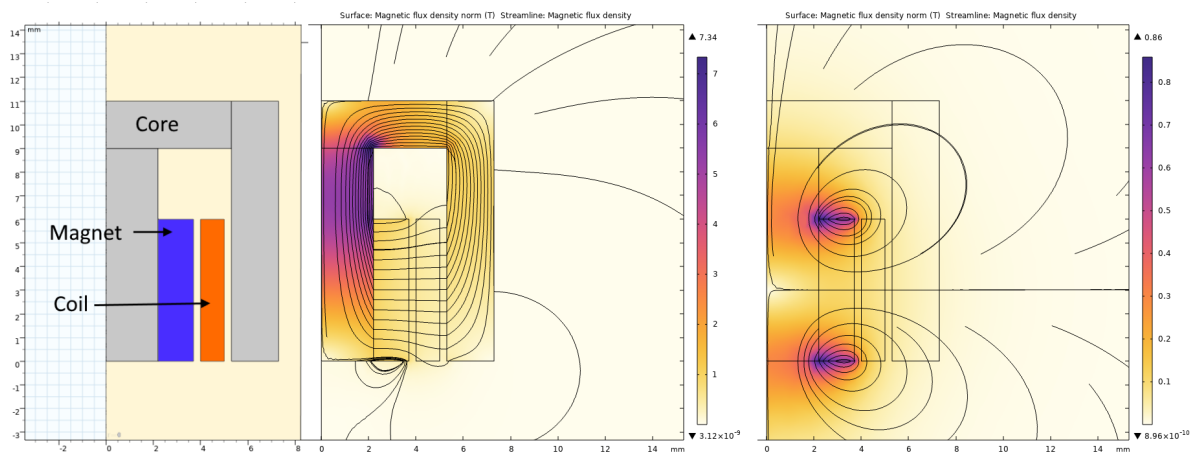

Figure 9.3: Simulation results 2D Axis-symmetric simulation voice coil. From left to right: Simulation setup, Results with Core and Results without core.

	With Core	No Core
Mass	$12\,g$	$3\,g$
Field strength	$0.41\,T$	$0.1\,T$
Peak force	$1.04\,N$	$0.252\,N$
Specific strength	$0.086\,N/g$	$0.084\,N/g$

Table 9.2: Simulation results 2D Axis-symmetric simulation voice coil

9.3.2. Radial magnet

The previous design is based on a radially magnetized cylindrical magnet. However, it was not possible to find such a magnet available for purchase. The best alternative would be using arc magnets [93], but further enquiry highlighted that this would lead to a significant cost increase of around 10 times the price of more conventional magnets. Therefore, a design was made with an array of rectangular magnets, together forming a radial magnetic field. Figure 9.5 shows these 3 possible magnet configurations.

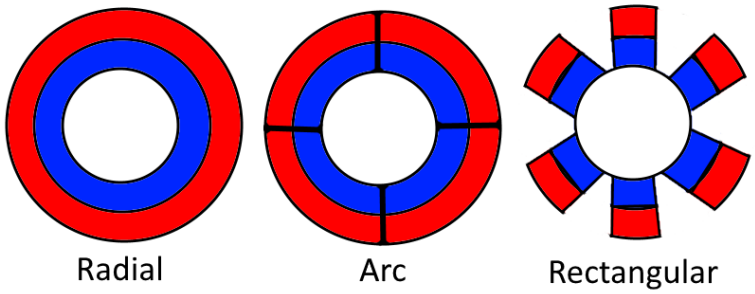

Figure 9.4: 3 different magnet layout concepts

9.3.3. 3D Simulation

Next, a detailed design was made that takes into account production, available magnets and the interface with the linear guidance flexure (Explained in chapter 9.4.1). In order to simulate the effect of the rectangular magnets, a 3D Comsol FEM Model was created. This model is more advanced and takes into account magnetic saturation, the field created by the electrical coil and measures the flux density over the full stroke of the actuator. In Appendix C, the simulation is explained with more detail. Next to a simulation, a first prototype was manufactured and used to measure the actual force over the actuator stroke.

Figure 9.5: From left to right, actuator design, the manufactured prototype with its experimental setup and the measurement and simulation results.

A positive result of this was that there is a very good correlation between the model and the measurement results. However, these results do show that this actuator design has some fundamental issues.

Over the actuator stroke, the delivered force drops significantly towards the extremes of the movement range. This is an issue since the extremes of the stroke require the highest actuator force to overcome the passive stiffness. At a peak current of 0.6A for the actuator coil, a maximum force of $0.042\,N$ was much lower than the initial estimate from the 2D design.

The significantly lower force was found to be caused by a combination of 2 unwanted effects:

1. **Flux leakage**: As shown in the left plot in figure 9.6, there is significant flux leakage on the sides of the magnets. This not only reduces the flux density in the coil but results in an opposing flux direction in certain parts of the coil. This means that in those parts, the resulting force is also opposing and therefore cancelling out a large part of the actuator force. This issue could be resolved by using fully radial magnets or reduced by using arc magnets. Another solution would be to introduce an actuator core, to reduce the reluctance in the required magnetic circuit and thus reduce the flux leakage.
2. **neutral-hung design**: A similar effect happens in the ZY and ZX plane of the actuator as shown in the right plot of figure 9.6. When the coil moves, it is no longer overlapping with the magnet and therefore the amount of flux through the coil is reduced. Even worse is the fact that now, the coil is again partially in the opposing field of the magnetic circuit, again counteracting the force of the actuator. This is a common problem in voice coil design and can be solved by an under-or overhung design, where the magnet is longer than the coil or vice versa. This results in a more constant flux density through the coil and therefore a more constant force-stroke relation.

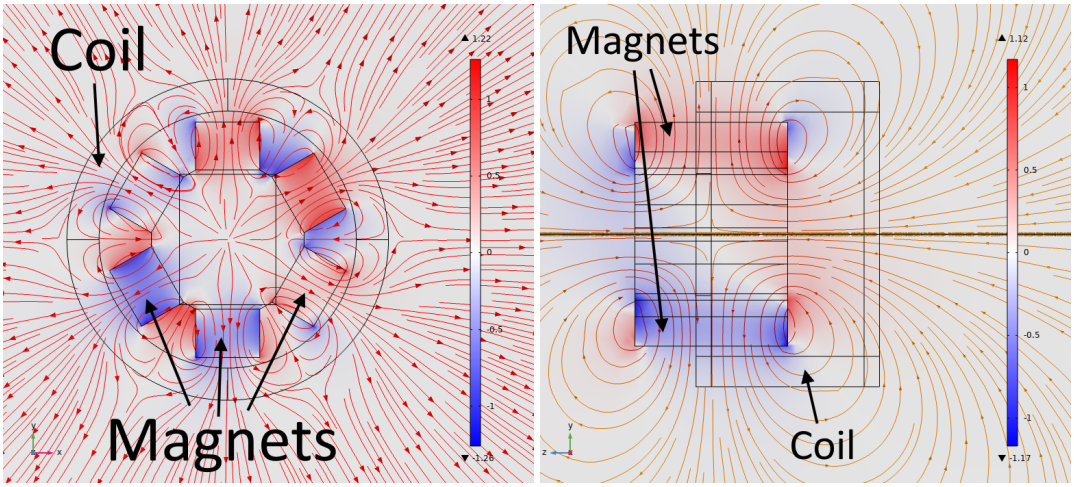

Figure 9.6: Magnetic flux density and field lines for rectangular radially spaced magnet concept.

In order to solve these issues and come to an actuator design that meets the set requirements, many things were tried in simulation such as different magnet dimensions, a longer magnetic core to get an under-hung design, an overhung design and even adding a full soft magnetic core. However, even with the soft iron core, the flux density only increases slightly and the specific force N/kg drops even further. From these simulations, it was concluded that the design with rectangular magnets will not meet the requirements from table 6.1.

In parallel to the cylindrical actuator concept, a planar voice coil design was considered. This design has good potential since it can use conventional rectangular magnets, but also more complex due to the planar coil and therefore, not favoured. Therefore, a new actuator design was needed in order to meet the requirements.

Opposing magnets concept

Finally, a new concept was created which uses axially magnetized disc magnets. This concept uses 2 opposing magnetic fields to create this required radial magnetic field as visualized in figure 9.7.

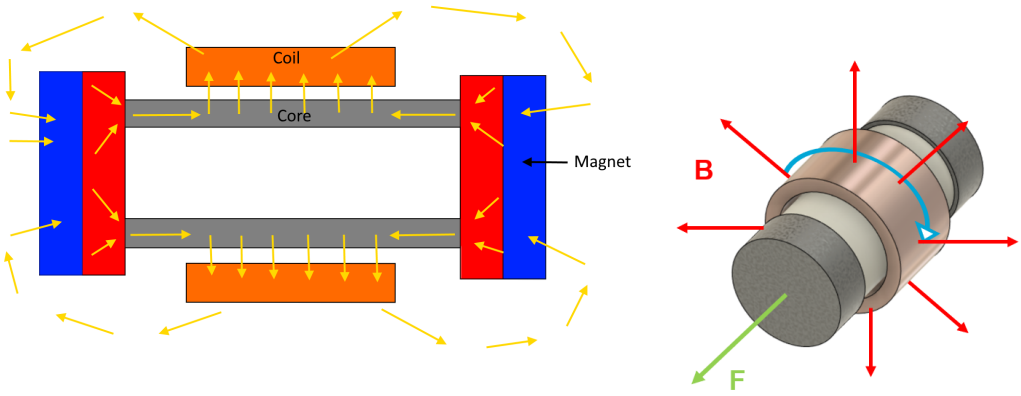

Figure 9.7: Visualization for opposing magnet actuator concept.

Whilst unconventional, this concept showed high potential in simulations with a maximum force of $0.25\,N$. As shown in figure 9.8, optimization of the actuator and adding a cylindrical core made from soft iron further guides the magnetic field and creates a radially homogeneous outwards magnetic field. The magnetic core further increased this peak force to $0.37\,N$ and resulted in a more constant Force-stroke relation, while only increasing the mass with $1\,g$. Another advantage of this core design is that by being a tube, it only requires simple machining steps and was therefore easy to manufacture.

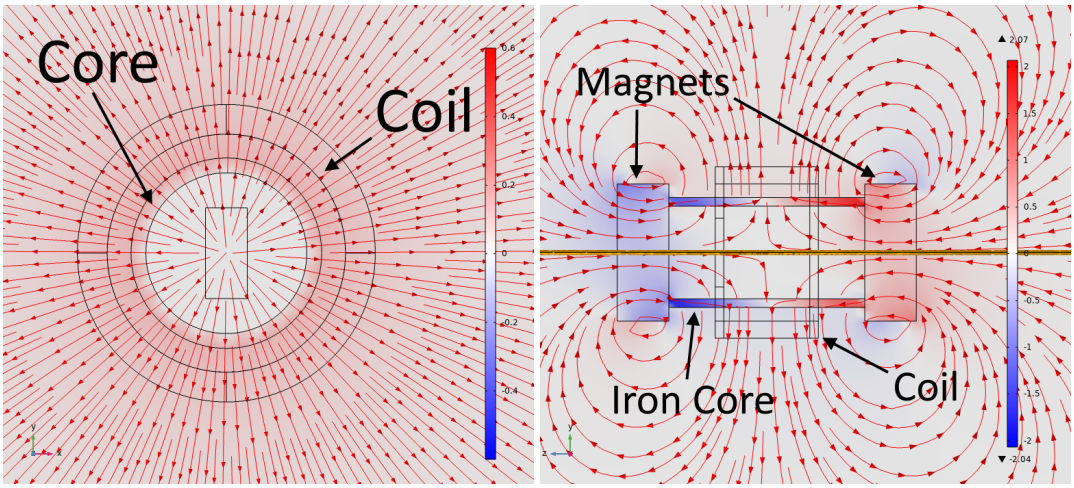

Figure 9.8: Magnetic flux density and field lines for opposing magnet concept.

Also for the new actuator concept, a prototype was made, which correlates well with the simulation results. Figure 9.9 shows the simulated force constant to actuator core position for both the concept with and without core and their corresponding measurements. The decision was made to use the actuator for the final design of the active unit cell. Table 9.3 shows the final design parameters and when comparing the force density of $75\,N/kg$ to the available off-the-shelf components that have a force density close to $50\,N/kg$, a 50% increase in force density was achieved, while at the same time reducing the cost significantly.

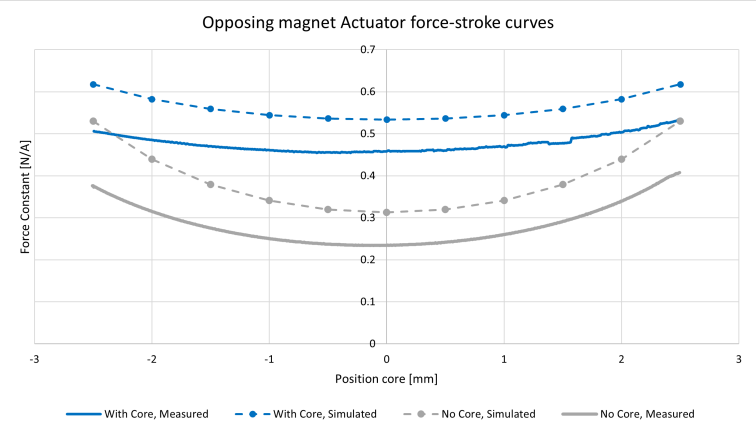

Figure 9.9: Actuator Force constant vs stroke for the opposing magnet concept.

Requirement	Target Value	Opposing magnet Actuator
Force	$0.38\,N$	$0.32\,N$
Stroke	$5\,mm$	$5\,mm$
Mass	$< 5\,g$	$4.23\,g$
Maximum dimension	$< 30\,mm$	$17.4/,mm$
Cost	$<$ €$30,-$	€$8,75$ excluding in house costs
Force Constant	-	0.53 N/A

Table 9.3: Final specifications for Opposing magnet actuator.

9.3.4. Actuator End stops

The dimensions of the coil and magnets are such that the outer diameter of the magnet and the inner diameter of the coil are equal. During the experiments with the first unit cell, it was noticed that this caused an interference fit between both parts, where the coil would partially slide over the magnet and would get stuck. This would not only stop the cycling but also damaged the coil. In order to solve this problem, a physical end stop was designed and glued onto the magnets as shown in figure 9.10.

This stop not only avoids the coil from getting stuck but also makes sure there is no point load on the coil, which could cause damage in the long term. However, in a future design change, this could be solved with for instance different magnets or integrating the end stop into the Actuator flexure.

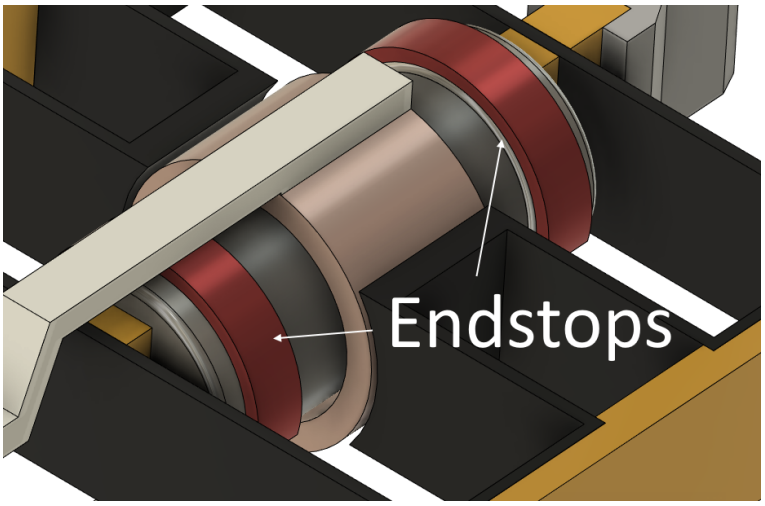

Figure 9.10: The End stops (in red) that were added after initial tests.

9.4. Actuator Flexure

An important advantage of the voice coil actuator is that there is no contact and therefore, friction between the moving parts. This means that less energy is dissipated and there is no hysteresis. However, the disadvantage is that the moving parts are not constrained and will need an additional mechanism to constrain all 5 unwanted degrees of freedom (DOF). To avoid friction from conventional solutions such as linear bearings, the choice was made for a compliant mechanism.

While a conventional bearing has no stiffness, most compliant bearings work by having a significant stiffness difference between the intended and parasitic motion directions. Due to the small scale and scope of the project, it was decided to not investigate more complex mechanisms such as 0 stiffness compliant joints [31]. Instead, a maximum stiffness target in the stroke direction of the actuator was set for only requiring 1% of the maximum actuator force at full stroke.

$$K = 0.01 * \frac{F_{Actuator}}{u_{stroke}} = 1.28\,N/m$$

For the stiffnesses in other directions, a significantly higher value of $100N/m$ was set as a target. During the design process, 2 different solutions were considered.

9.4.1. Membrane flexure

The first solution that was investigated is a flexure-based membrane support bearing, that is already used in other voice coil actuators [94], [95]. By cutting out sections of a circular surface, a set of parallel leaf springs is created. Since these leaf springs are radially spaced out, The advantage of this bearing would be that it could be integrated easily into the system and would allow for using a 2D production method such as laser cutting or water jet cutting. A design was created based on [95] and the dimensions of the actuator coil and core and is shown in figure 9.11.

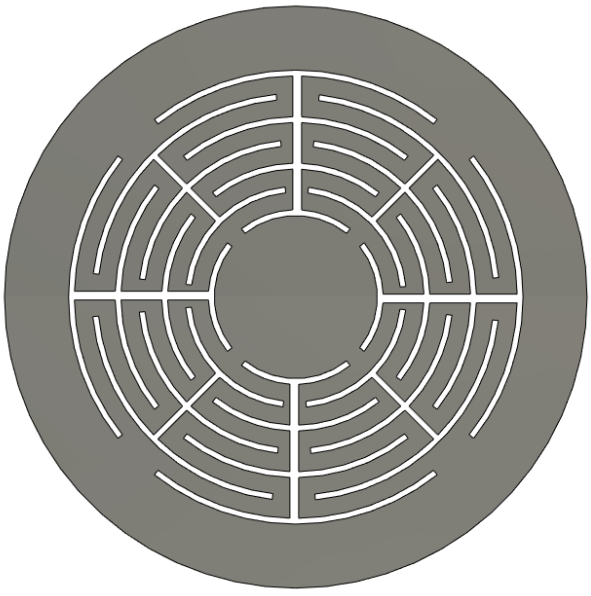

Figure 9.11: Membrane front view.

Due to the low stiffness requirement for the flexure, a material with a low Young's modulus and a very thin membrane thickness is required. For instance, a thin sheet of precision steel with a thickness of $0.025mm$ would result in a stiffness of $150\,N/m$. While a search for a material with a significantly lower stiffness could work out, a further issue is the significantly decreased parasitic stiffness at larger strokes.

To quantify this behaviour, the flexure was simulated in Comsol and the results are shown in figure 9.12. At full actuator stroke, the stiffness in parasitic motion direction is only 5 times higher than in the intended direction, which means the design is not suitable.

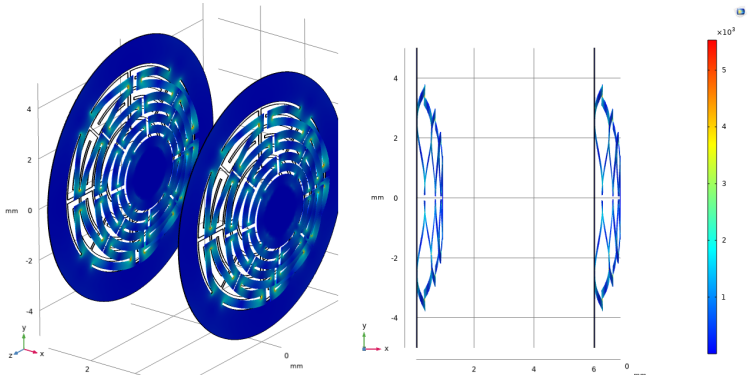

Figure 9.12: Comsol simulation results membrane flexure.

9.4.2. Folded-beam mechanism

Another solution that is used commonly in high precision systems is the folded beam mechanism shown in figure 9.13 [96]. By introducing parallel leaf springs with a rigid intermediate floating body, stiffness is greatly reduced in the stroke direction compared to the parasitic directions. The disadvantage of this solution is that the ratio between the parasitic and intended stiffnesses is dependent on the ratio between the thickness and length of the flexures, which is a challenge in the limited space of the unit cell.

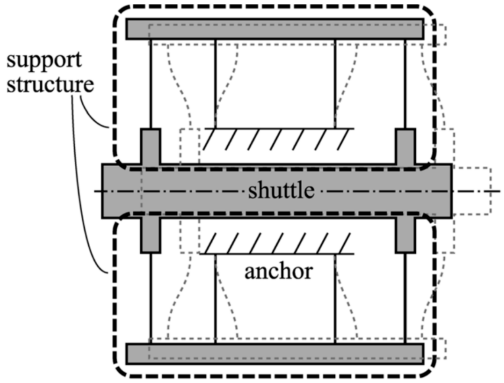

Figure 9.13: Compliant folded-beam mechanism. [96]

Similar to the membrane flexure, the folded-beam mechanism still requires a low stiffness material combined with thin flexures. A suitable material was found with Filaflex 60a pro, which is a Thermoplastic Polyether-Polyurethane elastomer (TPU) that can be printed with an FDM Printer. Due to the FDM printing, a flexure thickness of $0.42\,mm$ is required. In order to maximize the stiffness ratio, the available volume in the hexagon was filled completely as can be seen in the design shown in figure 9.14.

An advantage of the FDM Printing method is that it is possible to print with multiple materials. This was used to make the intermediate bodies and other bodies that are intended to be rigid from a significantly stiffer material, increasing the difference between the intended and parasitic stiffness. Polyethene terephthalate (PETG) was used for this function, due to its higher Young's modulus and the fact that it bonds well with the TPU during the printing process.

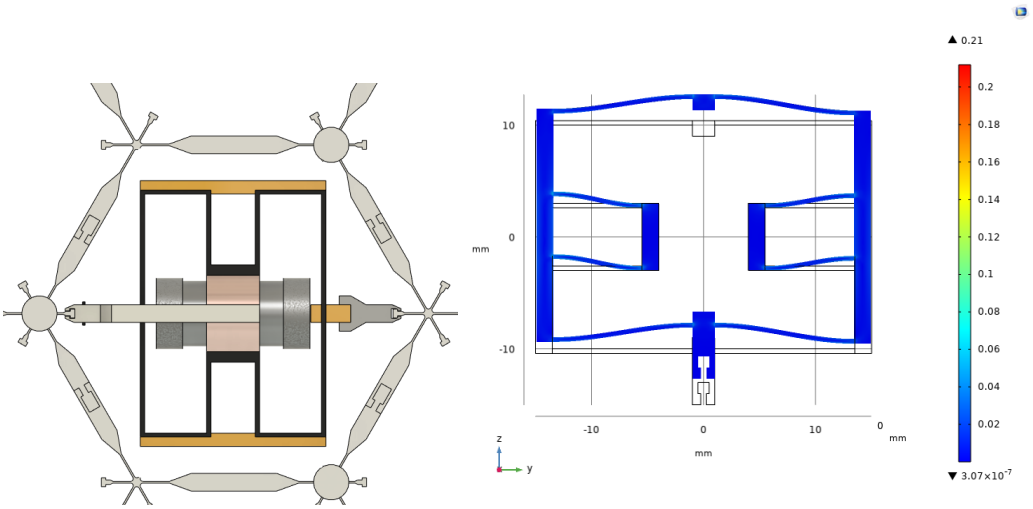

Figure 9.14: Flexure design and the deformation as simulated in Comsol.

Also for this flexure, a structural analysis was done through a Comsol model from which the results can be seen in figure 9.14. This results in a stiffness of $2.6N/m$, which is 2 times higher than the target value. The lowest parasitic stiffness is $131\,N/m$. While the design does not meet all design targets, this was deemed good enough and the flexure was used in the final design of the actuator. The printing of the final design was done with the FELIX Tec 4 3d printer, with a Dual printing head with direct extrusion, which is needed for printing multiple materials and using super flexible filaments such as TPU. Figure 9.15 shows the printing in progress.

By combining the flexure with the copper coil, magnetic core, magnets and some small parts to create the connection to the passive frame, the full actuator design is now complete. Figure 9.15 shows the final actuator assembly.

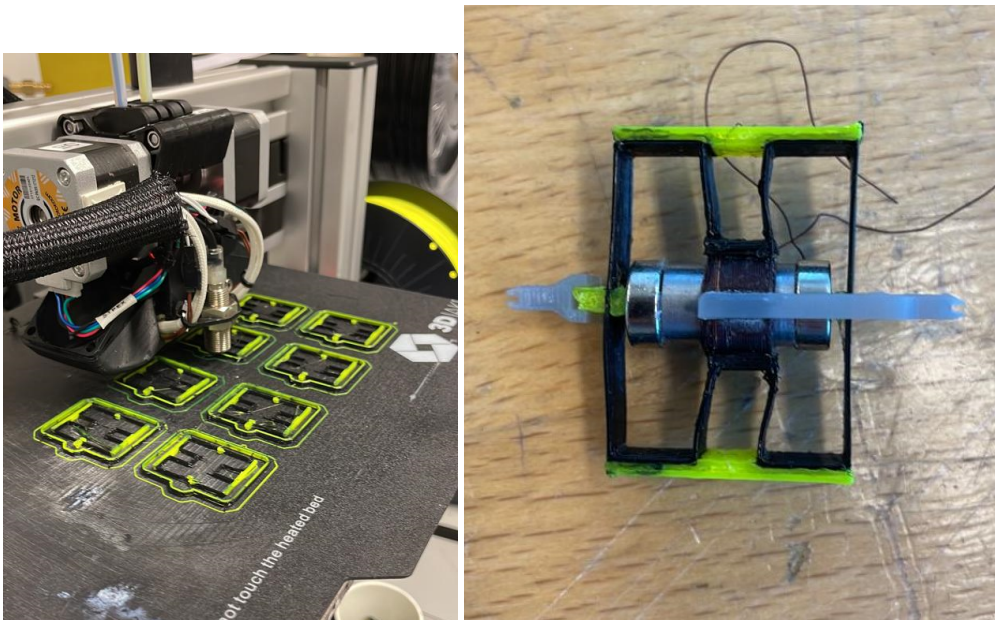

Figure 9.15: Manufacturing process for the actuator Flexure and the final assembly of the actuator.

10

Control design

By combining the actuator and passive unit cells, the active unit cell can be formed. However, in order to achieve any kind of behaviour, a control system is needed. This chapter aims to explain the design of this control system, which consists of a sensor for position measurement and a printed circuit board (PCB) which includes a microcontroller and hardware to support the actuation and measurements. Finally, the software that controls the PCB is explained.

10.1. Sensor

The final concept choice as shown in section 7, specified two possible solutions for the position measurement of the actuator. In this section, both options will be explained and analysed. After choosing the sensing method, the implementation and performance will be explained.

10.1.1. Self sensing

Firstly, the position could be calculated by measuring the induced voltage in the coil due to the change in the current through the coil, combined with the motor constant. Since we know that the coil has an inductance of $161\mu H$ and the maximum acceleration in current is $\frac{dI_a}{dt} = 40\pi * 0.6 = 75A/s$, we can calculate the peak induced voltage due to the change in the current:

$$V_{induced} = -L_i * \frac{dI_a}{dt} = -161e-6 * 75 = -1.127mV$$

While in an ideal system, it would be possible to measure such low voltages, there are many things in the actuator that could cause a significant error in this signal. Examples of things that could cause noise are the increased resistance of the coil due to warming up and the fact that the motor constant is not constant over the actuator stroke range. Therefore, it was decided to incorporate an actual sensor in the system instead.

10.1.2. Hall effect sensor

The best location to place the hall sensor is shown in figure 10.1. In this position, the field direction is in line with the motion of the actuator, which means that the field strength of a static sensor would be able to measure the movement of the magnetic core. The simulation explained in Appendix C was used to predict the field strength measurement as shown in figure 10.1.

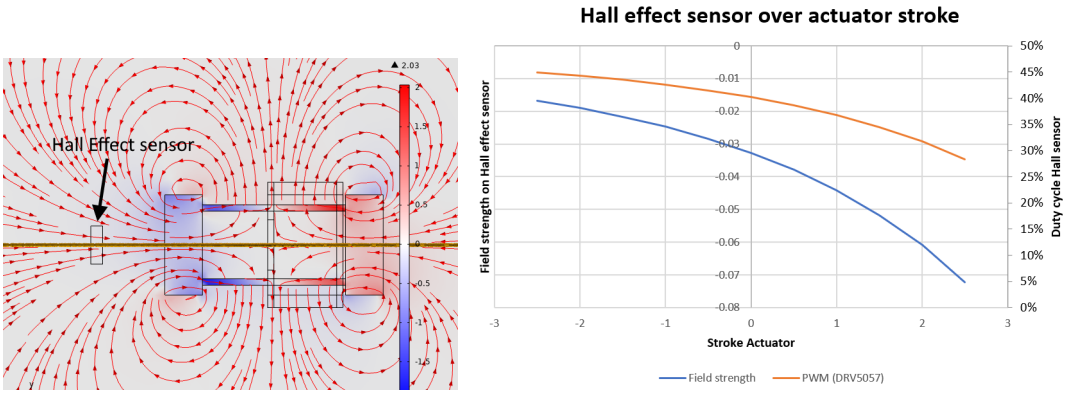

Figure 10.1: Section view of the magnetic field of the actuator, with highlighted the position of the hall sensor and the magnetic field strength over the actuator stroke.

The DRV5057A3 Linear Hall Effect Sensor from Texas instruments [97], was selected to measure this field and has a measurement range of $+-84\,mT$. The position as shown in figure 10.1 was chosen that the field strength is $72\,mT$, which is close to the maximum specified measurement range.

As shown in figure 10.2 The sensor was integrated into the frame of the actuator, so that it is static compared to the coil and the magnetic core can only move in 1 DOF compared to the sensor.

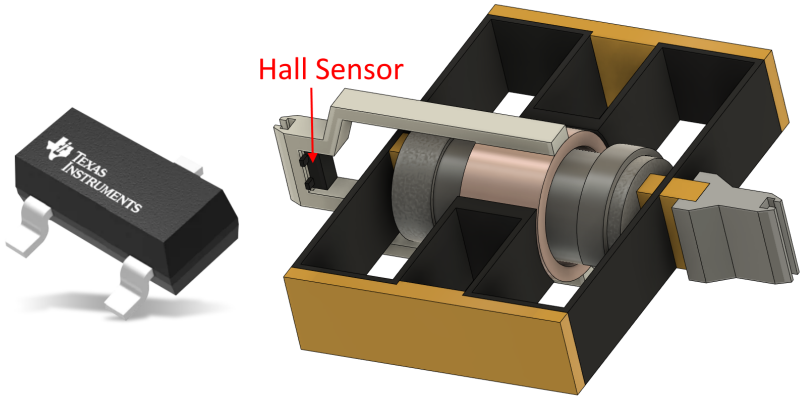

Figure 10.2: The DRV5057 Linear Hall Effect Sensor and how it is integrated into the actuator.

10.1.3. Sensor calibration and performance

The DRV5057 will output its measurement as a duty cycle on a $2KHz$ signal, where a 50% duty cycle is equal to $0mT$ and the gain of the sensor relates the duty cycle back to a measured field strength in mT. It is essential to have a good calibration method for the actuator. Whilst it would be possible to create a lookup table from the Comsol results and in this way convert it back to a displacement measurement, this method would be prone to 2 types of errors:

1. **Different relation between field strength and stroke:** This could be caused by a magnetic field that is different to what the simulations predict, with for example a lower rise in magnetic field strength per mm stroke.
2. **Offset in field strength:** If the initial distance between the magnet and sensor is slightly offset, there will be an offset in the displacement measurement.

In order to try and avoid these errors, multiple actions were taken to calibrate the sensor for each actuator. Firstly, calibration was done by measuring the field strength in the actuator in the controlled environment of the Instron 5943. By measuring the field strength over the full actuator stroke, a data set was created and a 5th order polynomial (P) was fitted to this. The software of the control PCB

uses this polynomial to create a lookup table and use it to calculate the actuator displacement. Next to this, the startup sequence of each PCB consists of a calibration, where the actuator is run against both end-stops. By doing so, the full travel distance of the actuator is known and the displacement will be corrected as shown in equation 10.2.

Further validation of this measurement was done by comparing the calculated displacement to the actual displacement of other actuators and all results are shown in figure 10.3. This shows that there is a good correlation between the simulation and measured data. Furthermore, the hall effect sensor proves to be a reliable and accurate method for measuring the actuator displacement with an accuracy of $2\sigma = 0.122\,mm$.

$$u_{lookup} = P(mT) \tag{10.1}$$

$$u_{corrected} = u_{lookup,i} - \frac{\max(u_{lookup,\mathbb{Z}} + \min(u_{lookup,\mathbb{Z}})}{2} \tag{10.2}$$

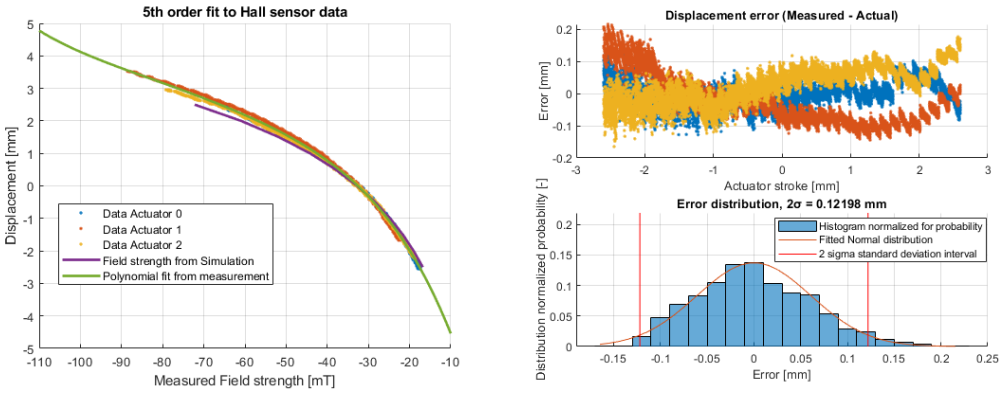

Figure 10.3: 5th order fit to dataset from 3 actuators and the error between fit and actual position.

10.2. Printed Circuit Board

Controlling the three actuators is done with a custom-designed circuit board. Making this board custom was essential for the project since the system requires power delivery with reversible polarity in a very small package. The design of this was done by Tjeerd Weijers, who is an electronics engineer in the team of the Technology Centre of the UVA.

For the PCB, a list of requirements was set up to make sure that it can function as a platform for future large-scale experiments with the unit cell. This not only consists of actuator control but also methods for reprogramming and communication with multiple unit cells at once.

For the project, the SAMD21E18A was selected, which is a very small microcontroller with a 32-bit ARM Cortex M0+ chip. It was selected for its beneficial properties, but also its availability during this period of extremely limited availability of microchips. The PCB shape was designed with cutouts for the actuator arms and grouped connections for the actuators. The full list of specifications is shown in table 10.1 and figure 10.4 shows the final design of the PCB.

Requirement	Solution
Control	SAMD21E18A Microcontroller
Actuator control	Motor control chip for PWM output with dual polarity $[-5V\ -5V]$
Sensor measurement	Timing input measurement on micro controller
Actuator current measurement	Shunt resistor
Reprogramming	JTAG to usb connector
Communication	Infrared sensor for wireless commands to multiple PCB's
Miscellaneous	RGB Led, USB and external power input

Table 10.1: Table with specifications of the custom designed PCB

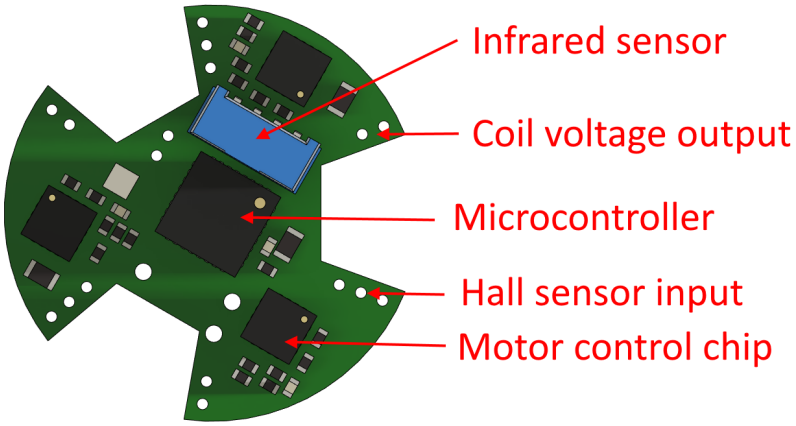

Figure 10.4: The final PCB design and its features

10.3. Control software

The SAMD21E18A was selected for its high calculation power in the small package, but also for its available libraries to allow for running Arduino code. With the help of Kasper van Nieuwland, who is a software engineer in the team of the Technology centre, a code base was created that consists of standard functions to read out the hardware. By doing so, it is now possible to write control software in C with only basic coding knowledge.

The code consists of an initialization run, where all sensors are calibrated as explained with equation 10.2, as well as a validation of the resistance of the actuator coils. By doing so, it is possible to check the state of the hardware without needing a serial connection. The PCB can communicate the result of this experiment through its onboard RGB Led.

Next, the actual software loop that creates the odd elasticity is run, which uses the following functions to control actuators:

- **Disp_Corr:** Input: Duty cycle, Output: Corrected displacement using lookup table and equation 10.2.
- **Perturb:** This function gives the system a controlled perturbation with a step input for actuator 0, which is needed to start off the limit cycle.
- **Serial Output:** For debugging and performance measurements, the microcontroller will output its measurements and power setpoints by writing binary data to the serial port.
- **The Odd function:** For each actuator, the required actuator output is calculated with $pwm_i = (disp_{i+1} - disp_{i-1}) * K_a$

By making use of 32-bit integers, instead of floating points and a lookup table for the 5th order polynomial, the calculation time for each software loop was minimized and the software is running at $600Hz$,

which is more than the intended $10 * f_{cycle}$. The software is written so that making changes and adding functionality without the need for further help from the Technology centre. This allowed for more experimental freedom and opened up opportunities for running other code such as gain sweeps, or other control functions.

11

Validation

In the final chapter of part II, the overall system assembly is explained as well as validated. Now that all sub-components have been explained, this chapter will first focus on the validation of a single hexagon, before finally validating and explaining the specifications of the fully assembled unit cell.

11.1. Single hexagon

In order to validate the specifications of the unit cell, the choice was made to first assemble a single hexagon and validate its properties. Figure 11.1 shows the assembled hexagon which was used. Firstly, the mass of the hexagon was measured to be $8.82\,g$, which is close to the expected mass of $8.1\,g$.

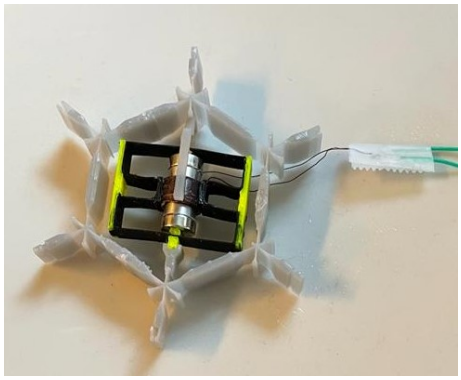

Figure 11.1: The assembled single hexagon.

Similar to how the stiffness of the passive flexure mechanism was determined, the static stiffness of the assembled hexagon was determined. This static stiffness increased from $42\,N/m$ for a hexagon to $46\,N/m$, meaning that the stiffness of the actuator flexure is actually $4\,N/m$, instead of the modelled 2.6 N/m. This is slightly larger, which could be due to printing inaccuracies or material properties being different.

Next to calculating the stiffness, the frequency response of the hexagon was validated. From the measurement data presented in chapter 8, a damping ratio of 0.265 and a resonance frequency of $19.2Hz$ is expected. In order to validate this, a frequency sweep was done for the actuator by controlling it with a function generator and measuring the hall effect sensor output. Figure 11.2 shows the output response over time, as well as the corresponding frequency response. When comparing this to the expected frequency response, it can be noticed that the damping ratio as calculated in equation 11.2 is significantly smaller and the resonance frequency is slightly higher at $20Hz$.

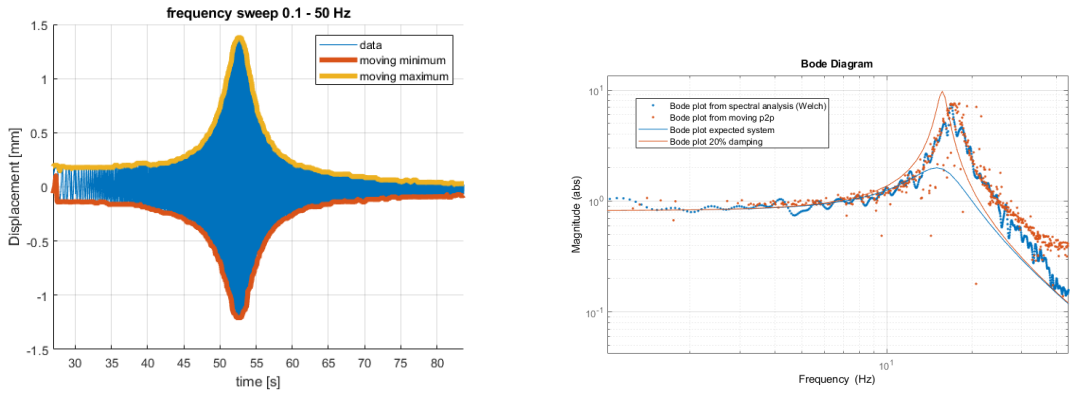

Figure 11.2: Response to chirp signal from 0.1 to 50 Hz and the resulting bode plot versus the expected system.

$$\frac{H_{peak}}{H_{static}} = \frac{1}{2\zeta\sqrt{1-\zeta^2}} \tag{11.1}$$

$$\zeta = \frac{1}{2b} = \frac{1}{2 * 9.3} \approx 0.0537 \tag{11.2}$$

There is a significant difference between the expected and measured damping ratio, with a damping coefficient that is only 20% of the expected coefficient. This could be explained by the methods used. Firstly, the extrapolation from $20\,mm/s$ to $314\,mm/s$ can introduce a large error. and secondly, simulating the frequency response by simplifying the system to a single mass spring damper system might be an oversimplification. In reality, the system consists of multiple flexures and their stiffness and damping are dynamic due to the viscoelasticity. However, by doing this simplification, it was possible to change the design based on predictions without a complex model.

The final damping ratio results in a Q-factor of 9.3, which is more than twice the expected Q-factor. Therefore, it can be concluded that the actuator will be more than strong enough to reach the maximum amplitude during the limit cycle. From equation 11.3 we can conclude that a peak force of $0.02\,N$ is expected to be needed for achieving the maximum cycle amplitude of $2.5\,mm$.

This force matches with the expected force from the chirp signal scaled up from the measured amplitude $1.3\,mm$ to the maximum achievable amplitude of $2.5\,mm$ as shown in equation 11.4. In this equation, the 50Ω internal resistance of the function generator (f) is taken into account

Important to note here is that this frequency response is achieved without any friction, which is not the case in the final testing setup.

$$F_{peak} = K_{lin} * u_{stroke} * 2\zeta\sqrt{1-\zeta^2} = 73.3 * 2.5e-3 * 2 * 0.0537 * \sqrt{1-0.0537^2} = 0.02\,N \tag{11.3}$$

$$F_{chirp} = \frac{U_f R_{coil}}{R_{coil} + R_{fg}} * K_{act} * \frac{u_{max}}{u_{chirp}} = \frac{1.4 * 3.2}{50 + 3.2} * 0.5 * \frac{2.5e-3}{1.4e-3} = 0.023\,N \tag{11.4}$$

Here, U_f is the voltage of the function generator, R_{coil} is the resistance of the coil, R_{fg} is the resistance of the function generator, K_{act} is the actuator constant in N/A.

11.2. Unit Cell

After the characterisation of the hexagon, a full unit cell was assembled and is shown in figure 11.3. Before showing the performance of the unit cell through experiments in part III of this report, there are some other parameters of the unit cell that can already be validated. During the literature review, the design targets were set in section 3.4.1. This section aims to explain the differences between the design targets and the final design and finally summarizes these in table 11.1.

Mass
Firstly, the mass was validated at $22.9g$, which is close to the expected mass of $23.2\,g$, of which the mass distribution is shown in figure 11.3.

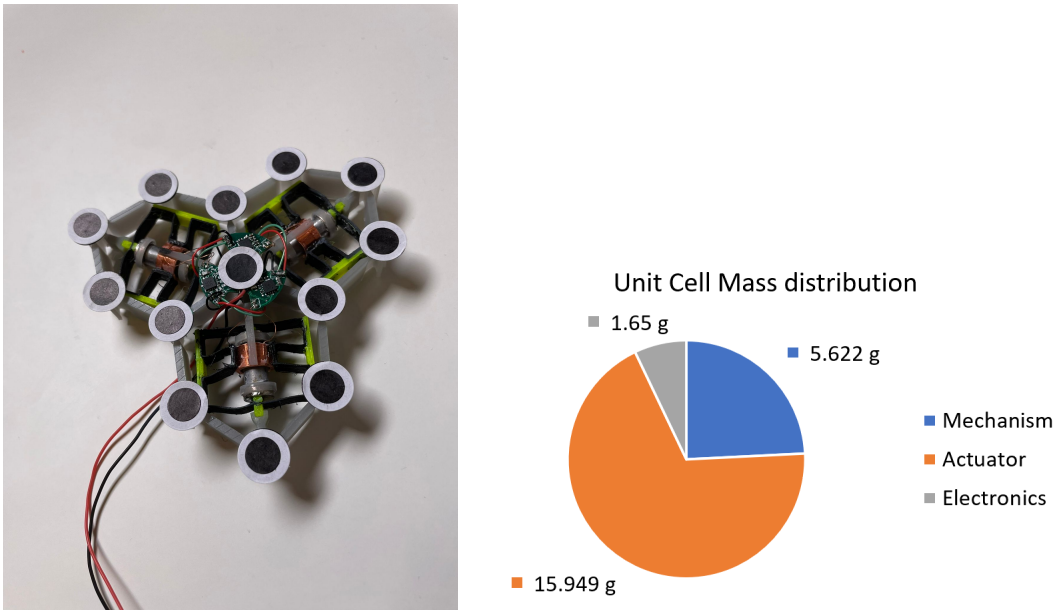

Figure 11.3: The assembled unit cell including tracking dots and its mass distribution.

Scale
Secondly, the scale of the hexagon was reduced by $150/44 = 3.41$, which is slightly more than the initial target. This will allow for experiments with 800 hexagons per m^2, which could lead to setups in which the behaviour starts approaching a continuum behaviour.

Strength to weight ratio
Next, the strength-to-weight ratio, Δ, is a bit lower than expected. From equation 3.4, we can calculate the strength to weight ratio as shown in equation 11.5. However, it is important to note that the real value of Δ will be slightly lower due to the angle of the actuators not aligning with the direction of gravity.

$$\Delta = \frac{F_{Actuator}}{mg} = \frac{0.32}{\frac{23.3e-3*9.81}{3}} = 4.2 \tag{11.5}$$

Stiffness
Another important requirement was the passive stiffness of $5.1\,\frac{mNm}{rad}$ or $77\,N/m$ when converted to compression stiffness. Whilst this target of $77\,N/m$ was met during the limit cycle due to the strain rate hardening effect, the static stiffness is only a fraction of this at $46\,N/m$. This will have an effect on the amount of passive deformation of the hexagon due to gravity.

However, the only change needed for the unit cell to meet the (revised) target stiffness would be a material with lower viscoelastic effects. One of the solutions for this could be using the Rigid 4000 material from Formlabs [98]. This material has a slightly higher Flexural modulus of $3.4\,GPa$, but could be printed with a lower flexure thickness and since it is a glass-filled resin, it is expected to have significantly lower damping. However, due to the time constraints and the fact that this material was not in stock at the UVA, the option was not explored further.

Deformation and stroke
With a designed stroke of $5.4\,mm$, the deformation of the hexagon is $\frac{5.4}{44} = 12\,\%$, which is more than the targeted $10\,\%$ deformation and $5\,mm$ of actuator stroke. Finally, the mass per hexagon is higher than expected at 7.76 per hexagon in a unit cell. This has a further effect on the expected passive

deformation due to gravity, which combined with the static stiffness is much more than the targeted $2.5\,mm$ as calculated in equation 11.6. Next to the deformation, the higher mass and lower stiffness are the cause of the resonance frequency of $20\,Hz$ instead of the initially estimated $27\,Hz$.

$$u_{deform} = \frac{mg * n_{layers}}{K_{static}} = \frac{7.76e-3 * 9.81 * 5}{46} = 0.0083m = 8.3mm \tag{11.6}$$

All of the before-mentioned outcomes are summarized in table 11.1. Whilst not all requirements were met, it should be said that without a design, or even a chosen concept, the design targets are close to the final validated unit cell specifications. With some potential future improvements on the flexure material, a further step could be made towards meeting all requirements.

Requirement	Target Value	Validated Value
Passive stiffness	$73\,N/m$	$73\,N/m$ ($46\,N/m$ Static)
Actuator peak force	$0.78\,N$ (Updated $0.38\,N$)	$0.32\,N$
Hexagon deformation	$> 10\,\%$	$12\,\%$
Hexagon mass	$5\,g$	$7.76\,g$
Natural frequency	$27\,Hz$	$20\,Hz$ (Single hexagon)
Hexagon Size	$< 48\,mm$	$44\,mm$

Table 11.1: Table summarizing the comparison between targeted and validated specifications.

11.3. Scalability

Whilst the dimensional scaling has been achieved, there are some other important metrics that define the scalability of the system. In order to work towards an experimental setup that could approach the continuum behaviour of the material, the system should not only be small but also cheap and easy to manufacture.

Firstly, the material cost of a single unit cell is estimated to be $58,37$€ and the distribution of this price is shown in figure 11.4. Next to this cost for materials, there is a price related to manufacturing and assembly time. The costs for manufacturing are expected to be low, due to using 3D printing techniques, which require very little operation time.

However, the time required for assembly is significant. An estimate for the amount of time it takes for the full production of a unit cell is almost 3 hours, without the assembly time of the PCB. A distribution of this assembly duration for each subsystem can be seen in figure 11.4. This means that the assembly of a large lattice consisting of 100 Unit cells, would take 6 weeks of working full time. Therefore, it would be beneficial to investigate methods that would reduce the assembly time. Examples of this could be a change in design so that it no longer requires glue connections, changing the sensor type to one which includes wiring or even using a flexible PCB.

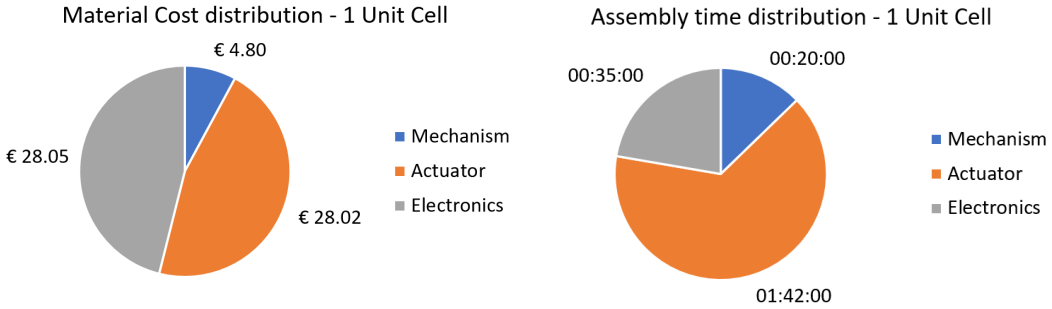

Figure 11.4: Distribution of material costs and assembly time per unit cell.

Part III

Results

12

Unit Cell

After validating the design parameters of the unit cell in chapter 11, the next phase is to acquire experimental data. The goal of these experiments is to characterise the single unit cell by studying the limit cycle behaviour. This chapter aims to explain the hypothesis, experimental setup, methods of data analysis and finally the results of this experiment.

12.1. Hypothesis

Even before starting the design, it was important to verify whether it is possible to achieve a limit cycle (explained in chapter 2.1.3) with the unit cell consisting of 3 hexagons and linear actuators. For this purpose, a Matlab Simscape Multibody simulation was created, which is explained in detail in Appendix D. This model uses the system parameters that have been calculated in part II of this thesis report, to make sure it is as close to the measured data as possible. The unit cell will always use the same control loop for achieving the odd coupling as shown in equation 12.1. Here dL is the displacement of the actuator and K_a is the gain or odd stiffness in N/m.

$$F_i = (dL_{i+1} - dL_{i-1}) * K_a \tag{12.1}$$

The first experiment will focus on the emergence of the limit cycle. Similar to what is shown in the work from Brandenbourger et al. [17], it is expected that for low gains, the damping will overcome the active behaviour and the equilibrium will be static. At a certain point, the gain will be high enough for a limit cycle of finite-amplitude to emerge, which is called the Hopf Bifurcation Point [99]. As explained in chapter 2, the limit cycle amplitude is determined by a non-linearity, which in the case of the new unit cell is hitting the end stops of the actuators.

Just like in chapter 2, dimensionless parameter ξ, as shown in equation 12.2, describes the ratio between the drive (K_a and Inertia (I), to the dissipation (Γ) and restoring forces (k). When $|\xi| < 1$, the dissipation and restoring forces are too big and the limit cycle will terminate. However, $|\xi| > 1$ a limit cycle will exist with a finite amplitude determined by non-linear limits such as the end stops, actuator saturation and others. Here, $|\xi| = 1$ is the Hopf Bifurcation point.

$$\xi = k_a/\Gamma\sqrt{I/k} \tag{12.2}$$

From this point onwards, a higher gain will result in a higher wave amplitude, up to the limit of the system, which in this case is the travel range from the actuator. Based on equation 12.2, equation 12.3 shows that based on the system parameters, a bifurcation point at a gain of $K_a = 0.0076N/mm$ is expected. Here, the inertia I is equal to the moving mass of the actuator in kg, Γ is the damping coefficient in Ns/m, which is estimated from the chirp response data and k is the linear stiffness of each hexagon in N/m.

To back up the prediction of this bifurcation point, a simulation sweep for a range of gains was done with the multibody simulation from appendix D and as can be seen in figure 12.1, this clearly shows the Hopf bifurcation point at $K_a = 0.0086 N/mm$.

$$\xi = 1 \rightarrow k_a = \frac{\xi * \Gamma}{\sqrt{I/k}} = \frac{1 * 0.0624}{\sqrt{5e-3/73.3}} = 7.6\, N/m = 0.0076\, N/mm \tag{12.3}$$

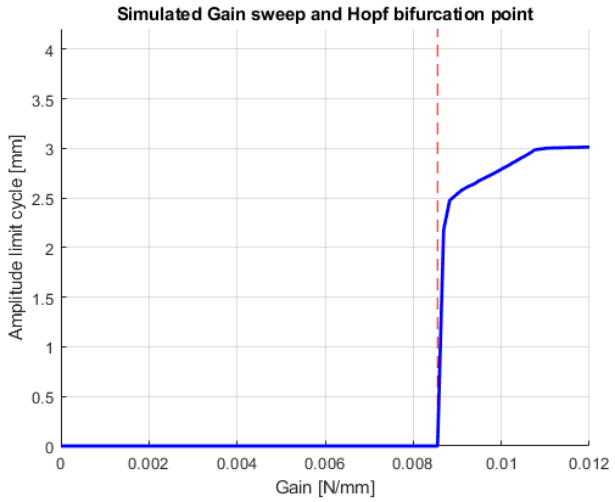

Figure 12.1: Simulation results with the fitted Hopf bifurcation point at $K_a = 0.0086 N/mm$. The bifurcation is almost discrete, until an amplitude of $2.5\, mm$, where the non-linearity of the end stops starts interfering.

From this simulation, similar behaviour is expected for the unit cell in an experimental setup. However, the bifurcation point might be different due to the presence of friction, nonlinearities and other differences between the model and reality.

12.2. Experimental setup

With the hypothesis of having a limit cycle emerge when $|\xi| > 1$, it is necessary to be able to measure the amplitude of a limit cycle. For this, a setup was made with a Teflon surface for the unit cell to rest on to limit the amount of surface friction. Next to this, the unit cell is connected to a $5\, V$ power supply with flexible wires that should not influence or constrain the movement of the unit cell.

It is possible to communicate with the unit cell with a USB serial port connection. By using the program PuTTY, which uses this serial port, the measurements and output of the PCB can be logged [100]. However, the cable needed for this communication constrains the movement of the unit cell and increases the surface friction. While it was tried to minimize the effect of the USB cable, the required gain for achieving maximum limit cycle amplitude was measured to be $K_a = 0.07\, N/mm$, which is more than 2 times higher than without the cable. Therefore, another method for measuring the wave amplitude of the unit cell is needed and this is done by tracking dots on a video recorded with a high-speed camera. By using a Basler aca640-750um, a 480x640 pixel video is recorded at 500 frames per second, which is approximately 20 frames per cycle.

As can be seen in figure 12.2, the unit cell has been fitted with tracking dots on each corner and is placed onto the white Teflon surface. By combining a back-light and a ring light around the camera, the image is adjusted so that the dots are easy to track for tracking algorithms. By creating a transparent boundary box, the unit cell is also constrained to only move within the field of view of the camera. The setup is shown in figure 12.2.

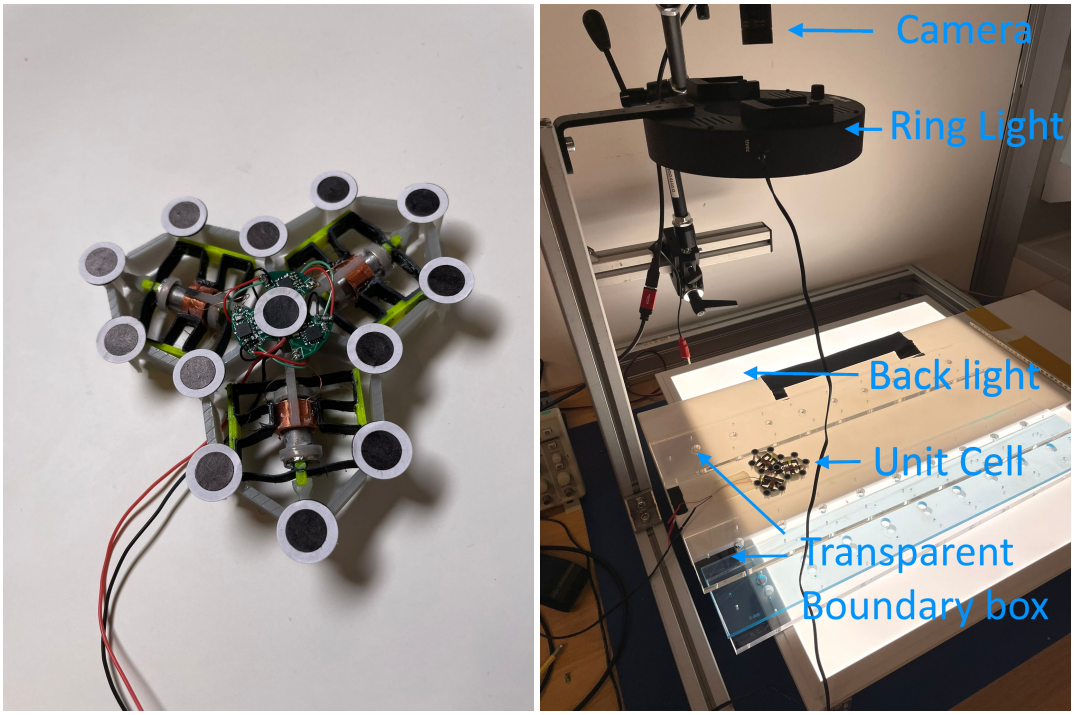

Figure 12.2: Unit cell fitted with tracking dots and the full experimental setup. By combining the ring light and the back light, the resulting image shows the tracking dots clearly and the boundary box is invisible.

The code on the PCB was written so that when powered, the unit cell will sweep through cycles of 1-second duration for a sweep of gains in the relevant range from 0 to reaching the amplitude limit due to the end stops of the actuator. For the duration of this sweep, the camera records the image and writes this to a series of .Tiff images.

12.3. Data Analysis

After collecting a series of images, data processing is needed before it is possible to quantify the state of the unit cell. Firstly, the series of images is converted into a video file, to match the extension type used by a script written by Jonas Veenstra using the python package OpenCV. This script takes the individual frames of a video, searches for tracking dots and outputs the positions of these dots into a .CSV file with a spatial resolution of $0.22\,mm$.

The dataset is then used for further analysis with a Matlab script, which is shown in appendix E. This script takes the tracked dots and recognizes which part of the unit cell they belong to (centre point, joint with an actuator etc). With this information, the actuator length can be calculated and converted to a signal over time. By then analysing each cycle of the parameter sweep, a stabilized wave amplitude can be calculated. An example of an image with the tracked hexagon and the time-series data that is generated from this is shown in figure 12.3. The data analysis process can be summarized in three steps:

1. Convert images to a single video file
2. Track for each frame of the video, the positions of the tracking dots and store them
3. Use these positions to reconstruct the unit cell digitally and analyse the actuator stroke over time.

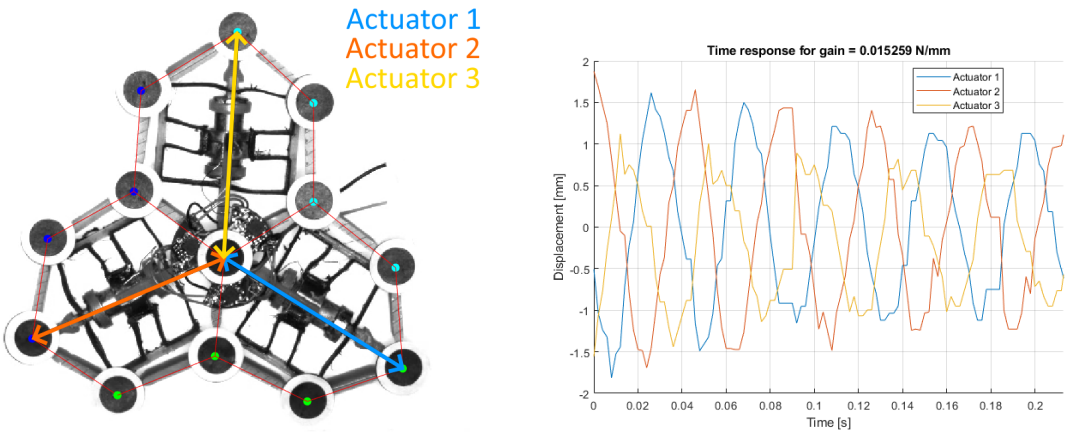

Figure 12.3: Frame from video of unit cell with the fitted unit cell frame and the time series response of one of the gain sweep setpoints, which shows the phase delay of $\frac{2\pi}{3}$ between each actuator and a decaying amplitude. With the colored arrows, the left figure shows the actuator lengths displayed in the right figure.

12.4. Results

With the actuator strokes, the stabilized limit cycle was found and compared to the gain K_a for each sweep as shown in figure 12.4. From these results, we can see a Hopf Bifurcation point around $0.01\,N/mm$, which is slightly higher than for the simulated cycles. This was expected and can be explained by the surface friction of the Teflon, which will increase the dissipation and therefore increase the ratio ξ as explained earlier in equation 12.2. This effect of the surface friction was also validated by experimenting with other higher friction surfaces and indeed there, the bifurcation only happened at even higher gain values.

Whilst for the simulated results, the bifurcation was at a very discrete point, the data of this gain sweep shows a much smoother transition towards a limit cycle. Firstly, this was expected to be caused by the relatively short measurement windows and the limit cycle potentially not having fully reached a steady state. However, by specifically testing the low gain values for a longer time, it was found that indeed these limit cycles were stable, but just very low in amplitude. This non-discrete behaviour could be caused by the effect of the visco-elastic response of the material or other factors.

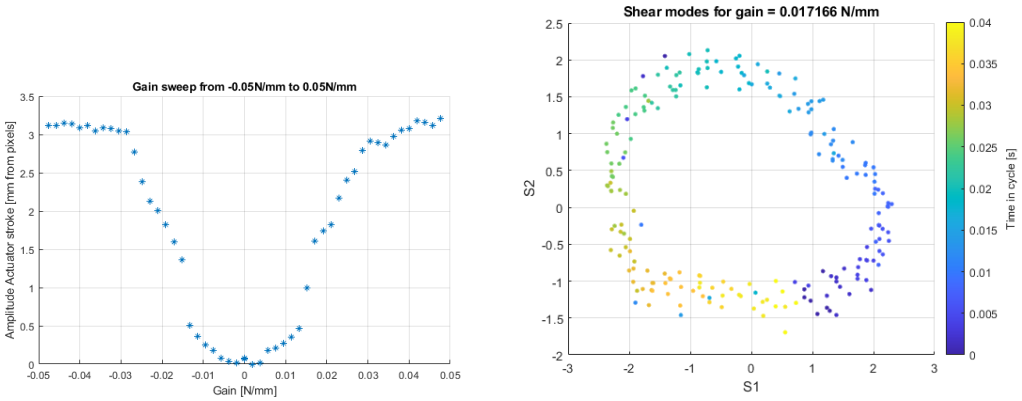

Figure 12.4: Stabilized limit cycle amplitude for varying gain on the left, with a smooth transition towards the maximum limit cycle amplitude. On the right, the cycle between modes S1 and S2 is shown. Here, it is clear that the system switches between both modes and there is no overlap. The colours represent the time in each cycle, which shows the direction of the limit cycle.

Next to the bifurcation point, it is interesting to note that the limit cycle frequency is approximately $24\,Hz$, which is a slightly higher frequency than the resonance frequency of a single hexagon. This could be explained by the mechanical coupling between the hexagons. This suggests that potentially, the damping of the unit cell is also different to the single unit cell, which would significantly influence

the bifurcation point due to a change in Γ. However, no frequency response analysis was completed for the unit cell.

During the cycle, the unit cell sweeps through different modes, which can also be seen in simulation. These modes are similar to the unit cell of Brandenbourger et al. with 2 shear modes, S1 and S2 and 1 breathing mode B. Figure 12.5 shows what these modes look like and to predict these mode shapes, a 2D Comsol eigenmode analysis was completed, which results in the following modes:

1. **The rigid body mode.** Where the full body can move rigidly in all 3 degrees of freedom for a 2D system.
2. **Shear mode S1**, in this mode, Actuator 1 and 2 are opposing each other's travel and Actuator 3 will be in a neutral position.
3. **Shear mode S2**, in this mode, Actuators 1 and 2 are equal in travel, but opposite to the length of actuator 3.
4. **Breathing mode B**, in this mode all actuators move in phase. As seen from the Comsol simulations, this mode also only occurs at a higher frequency ($40\,Hz$) and will require more energy. This is the reason that this mode does not occur in the limit cycle or in the anti-damping sweep which is explained later in this section.

They can also be parameterised in a similar way to [17]. Because the mode shapes are slightly different, the lengths of the actuators are used as inputs instead of angles and based on the mode shapes from figure 12.5. By parameterizing them, it is possible to quantify the magnitude of a mode for each frame of the data set.

$$S1 = \frac{1}{\sqrt{2}}(dL_1 - dL_2) \tag{12.4}$$

$$S2 = \frac{1}{\sqrt{5}}(dL_1 + dL_2 - 2dL_3) \tag{12.5}$$

$$B = \frac{1}{\sqrt{3}}(dL_1 + dL_2 + (dL_3) \tag{12.6}$$

When looking at the response data for a specific gain. It can be found that indeed the system stabilizes with a limit cycle in the space of S1 and S2, for which the direction is indicated by the direction of the odd couplings and the amplitude by the Gain value. Figure 12.5 shows these modes and their direction as a function of time.

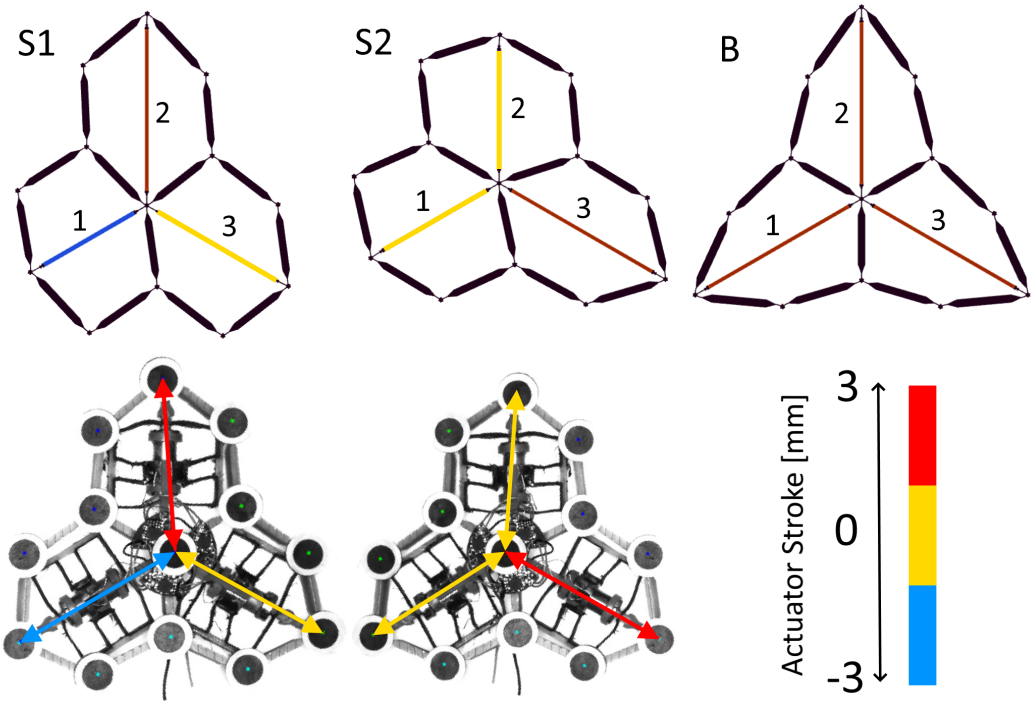

Figure 12.5: Mode shapes from Comsol compared to limit cycle data.

12.4.1. Anti-damping

The odd couplings between the actuators are a control strategy that allows for emergent behaviour compared to for instance a time-modulated system for which the control input is known beforehand. However, there is still a programmed coupling between each actuator and therefore an expected cycle with direction based on gain K_a. A further step towards even less control input could be made by removing this coupling and controlling the actuators individually towards instability and therefore a cycle. For this, a new control function was introduced which is shown in equation 12.7. By amplifying the velocity of the system, Anti-damping, the dissipation Γ of the mechanism is overcome resulting in an unstable system.

$$F_{i,t} = K * v_{i,t} = K * \frac{xi,t - xi,t-1}{t - t - 1} \tag{12.7}$$

Due to the mechanical coupling between each actuator, it is expected that the actuators might synchronize for first-order modes S1 and S2. However, in this case, there is no defined direction of the cycle and it is not sure if there will be a cycle between both modes, or if S1 or S2 will be dominant. In order to characterise the behaviour during this anti-damping, a gain sweep was done for 0 to $7.63e{-}04\,Ns/m$.

As can be seen in figure 12.7, mode S1 is dominant in the lower gain region and towards higher gains, a limit cycle between mode S1 and S2 emerges again. By measuring the amplitude of each mode, it is possible to quantify the presence of each mode for each gain, which is shown in the final plot. Again, mode B is not occurring, which can be explained by the fact that it is a higher-order mode.

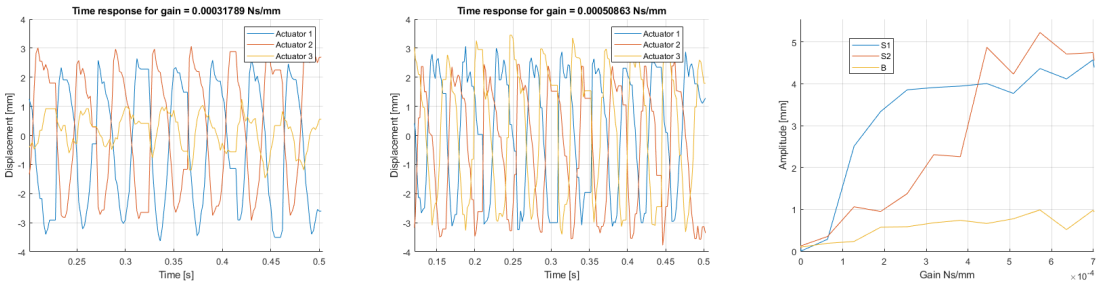

Figure 12.6: Time response for both the lower and higher gain showing and the amplitudes of each mode versus the gain.

It is not clear why mode S1 dominates at lower gain values and more research could be done to find out why. Whilst it could be possible that mode S1 simply requires less energy and therefore is the preferred mode, it could also be caused by one of the actuators under-performing compared to the others. This behaviour could be explained further by simulation and testing different methods of perturbation in an attempt to make other actuators dominated, which would prove it is not caused by actuator performance.

By comparing the shear modes, it becomes clear that indeed, the direction of the cycle is not defined by this antidamping and both directions were present as shown in figure **??**. The magnitude of the gain or imperfections in the system may determine the direction for specific gain values, but this can not be determined with the current dataset.

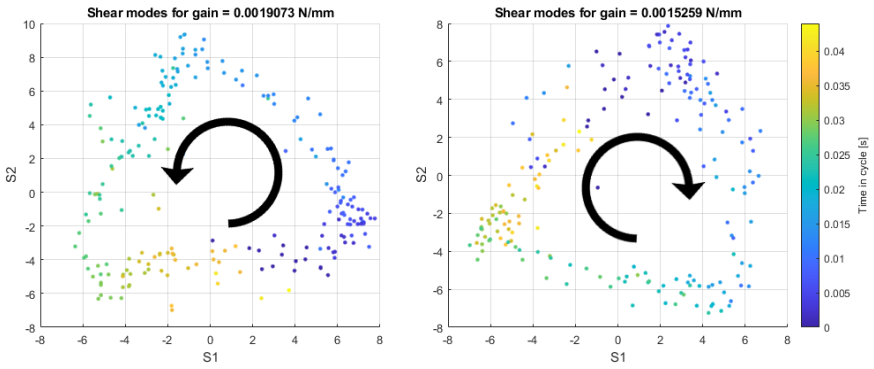

Figure 12.7: Here, the cycles between modes S1 and S2 are shown for two different setpoints. Again, it is clear that the system switches between both modes and there is no overlap. The colours represent the time in each cycle, which shows that both cycles are in opposite directions.

Other things that could be tested to find out the performance of the unit cell are frequency sweeps to find the frequency response for a hexagon and how it is affected by other hexagons. For example, when looking at modes S1, S2 and B, it is expected to have a different frequency response for hexagons depending on if they are oscillating in phase, or with a phase difference of $\frac{2\pi}{3}$. However, the end goal is to use this unit cell in a larger lattice, where again a different frequency response is expected and many more mode shapes are possible.

13

Locomotion

As shown in the work from Brandenbourger et al [17], unit cells with a limit cycle where there is switching between 2 modes can lead to locomotion. In the case of Brandenbourger, the locomotion is achieved with a hexagon or ring with even more vertices which act as an odd wheel. By switching between the modes S1 and S2, repetitive contact with a perpendicular vector is achieved, which results in a rolling motion of the ring. Due to this rolling, the full system starts locomoting in an autonomous way that has been proved to be robust against inclinations and even obstacles. A unique and novel characteristic of this locomotion is that it is robust and achieved fully autonomous without complex control or knowledge about the environment [18].

In the case of the unit cell designed in this thesis project, a similar repetitive contact with a perpendicular force vector is expected. However, due to the triangular shape of the 3 combined hexagons of the unit cell, it is not expected that this will result in a rolling motion. Other methods of locomotion, such as hopping could be present though and therefore, an experiment was completed.

13.1. Experiments

A testing setup was created where a single unit cell is placed vertically onto a rubber surface to maximize friction. The unit cell is slightly leaning backwards, to prevent it from falling over. As shown in figure 13.1, this setup allows the unit cell to freely move horizontally. Figure 13.1 also shows what happens with the overlay of 2 still images of the start and end point and a plot of the path taken by the centre of the unit cell.

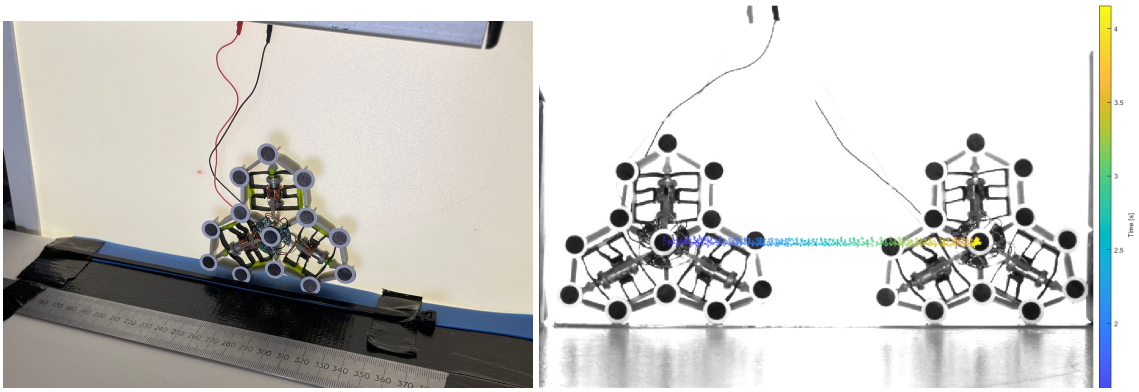

Figure 13.1: Experimental setup for locomotion and a frame from the video used to analyse the motion

By using the odd coupling between each actuator and sweeping the gain from $K_a = -0.0447\,N/mm$ to $0.0447\,N/mm$, it was found that at higher gains, the unit cell indeed starts to locomote by hopping in a direction which is controlled with the sign of the gain. Figure 13.2 shows the velocity of the unit cell

for each gain. Additionally, it is clear that modes S1 and S2 are dominant similar to the experiments in chapter 12. The unit cell was able to walk on inclinations up to an angle of $7.5°$ after which it became friction limited.

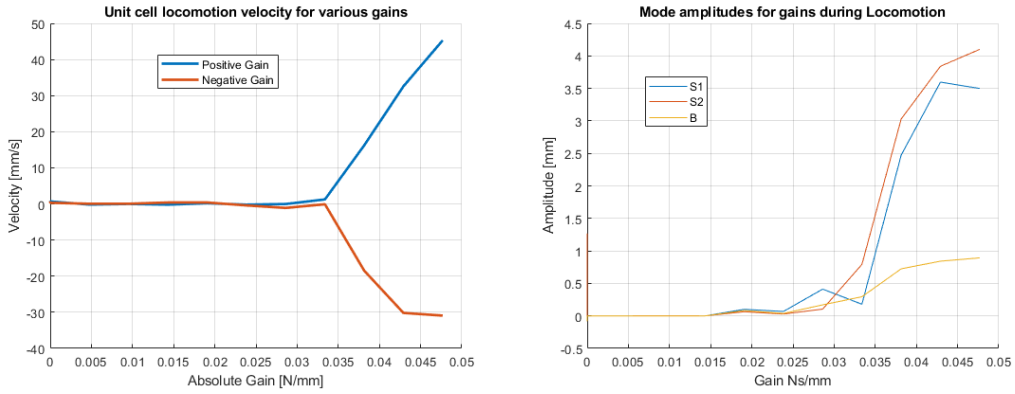

Figure 13.2: Locomotion speeds and the amplitude of each mode during locomotion.

13.2. Rolling

At a maximum achieved speed of $50\,mm/s\,(0.18km/h)$, the system is not able to locomote very fast. Due to the triangle shape of the unit cell and the limited stroke of the actuators, there is not enough momentum for the unit cell to start rolling. However, a design could be made to encapsulate the unit cell into a cylindrical shape reducing the effort needed for the system to start rolling. An attempt for this was done unsuccessfully by adding variable length feet to each joint combined with a flexible rubber "Tire" as shown in figure 13.3.

However, the designed feet were not stiff enough to support the weight of the unit cell and as seen in the figure they collapsed. Because of this design issue, the feet reduced the locomotion performance compared to the unit cell and removed the direction change due to a change of sign for the gain. Due to the high strain caused by the collapsed feet, one of the compliant joints of the hexagon eventually failed. Interestingly though, while it is expected that the stiffness of the broken hexagon changed significantly, the limit cycle did not stop, which supports the argument that the limit cycle is robust.

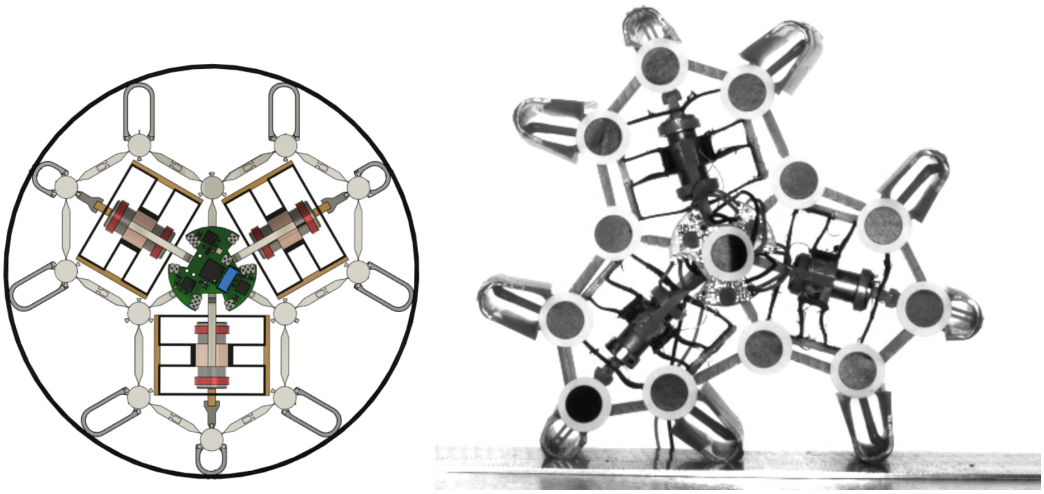

Figure 13.3: The design and manufactured assembly to attempt rolling.

While the initial experiments did not succeed, improvements that incorporate stronger feet or even a completely new design could enable the unit cell to locomote by rolling and possibly increase the

locomotion speed. Another option could be to combine many more unit cells into a cylindrical shape. As explained in chapter 14, simulations of setups with many unit cells show a similar tendency to cycle as a whole and therefore locomote. To conclude, the current unit cell can locomote by hopping, but other methods such as rolling could be much faster and possible achieved by a change in design or lattices with many unit cells.

14

Lattice

Recalling from chapter 2, odd elasticity is the asymmetric elastic response of a material as a bulk. This means that in order to actually achieve odd elasticity, a material needs to be made consisting of many unit cells. As explained in chapter 11, the newly designed unit cell allows for up to 800 hexagons or 260 unit cells per m^2, which would be an enormous step towards approaching continuum behaviour. However, building such a setup would take almost 5 months for a single person, which is impossible in a thesis project.

In order to showcase how a lattice would behave within the available time frame, a small lattice was built. Chapter 4 already explained that according to the work from Guido Baardink, the current unit cell is expected to have an odd modulus of $K^0 = -\frac{\sqrt{(3)}}{8}K_a$ [32]. Based on the proposed lattice layout in this work, a lattice design was created as shown in figure 14.1, consisting of 7 unit cells and therefore 21 hexagons.

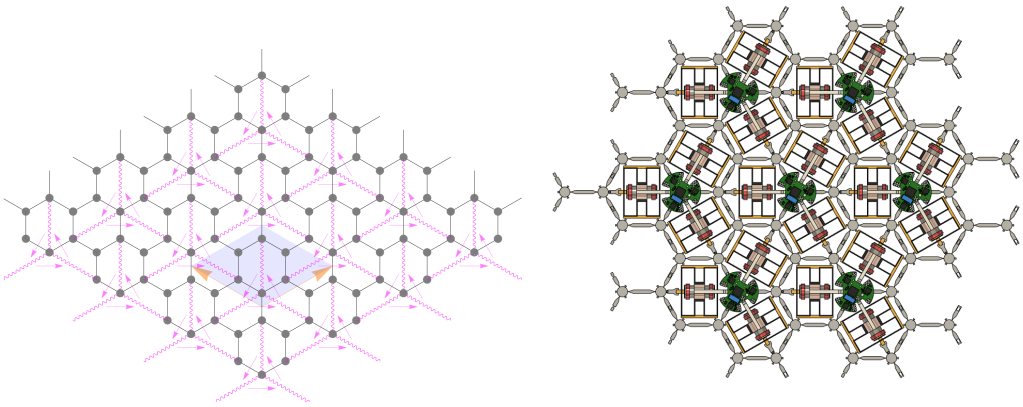

Figure 14.1: Lattice configuration from Guido Baardink [32] and the corresponding lattice design with 7 unit cells

14.1. Lattice manufacturing

The bigger lattice was assembled similarly to the single unit cell. In order to limit the amount of wiring in the lattice, it could be possible to daisy chain the unit cells. However, this means that the first section of wiring will have to carry the total current of the system and this could lead to thermal issues. Furthermore, by daisy-chaining the system it is more complex to remove power from individual unit cells and therefore it would be very hard to experiment for instance measuring the effect of imperfections in the system by turning off unit cells.

Therefore, it was decided to connect all unit cells individually to a central point of power. This was

achieved with a terminal block with screw connections for both the positive and negative terminals. In this way, it is very easy to remove the power from specific unit cells.

Also for the lattice, a gain sweep was completed where for each gain, the unit cell cycles for a duration of 10 seconds and pauses for 1 second in between. Currently, the timing of this sweep is aligned by powering on all unit cells simultaneously and from there controlling the duration of each process with the internal clock of the microcontroller. Since this still does not work perfectly, more work on this is required. In a future setup, the infra-red sensors could be used to trigger the start of each sweep simultaneously for all unit cells.

14.2. Dynamic response

As explained in chapter 2, odd elasticity is a linear theory and properties such as the odd ratio of the material can be achieved with an over-damped system. However, simulations from Jonas Veenstra show very interesting behaviour of a lattice with many unit cells during a limit cycle [19]. The system starts in a state where each individual unit cell has a limit cycle, but there is no synchronization between them and as a whole, the system is disordered. However, as time progresses, the unit cells start synchronizing and the material starts showing mode shapes as a whole and at a lower frequency. Figure 14.2 shows a simulation of a lattice with 50x51 hexagons (850 unit cells) and as shown here, the system synchronizes over time towards the first mode of a 2D square.

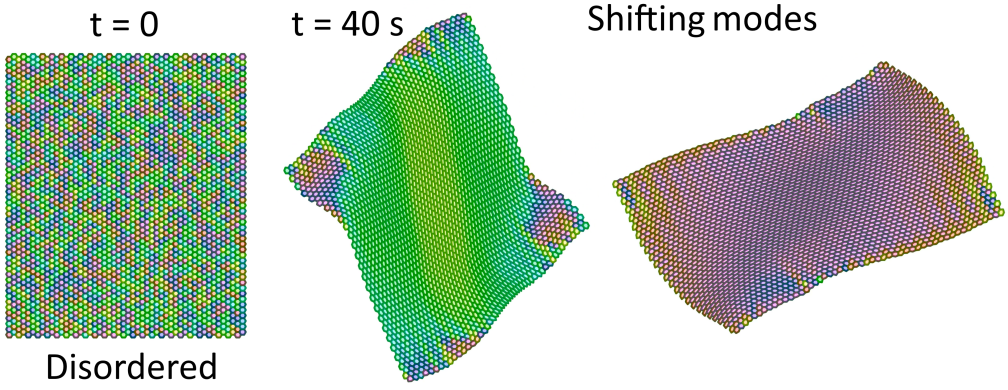

Figure 14.2: Simulation of a 50x51 Lattice of a unit cell with the divided actuation concept. At t=0, there is chaos, but the system synchronizes towards the lowest mode for a square. [19]

The synchronisation of individual unit cells towards a general mode shape could be very interesting as other shapes could lead to things such as rolling and crawling. Indeed, simulations from Veenstra show that a large lattice in a cylindrical shape has a tendency to roll and in this way could locomote in a similar way to the ring from the work of Brandenbourger et al. [17]. It is not sure if a lattice with only 7 unit cells will show similar synchronisation towards a lower order mode. When looking at the modes in figure14.2, the edges still show some chaos and when decreasing the number of unit cells, this effect becomes more persistent.

14.3. Testing setup

For the first experiments, it was decided to focus on the limit cycle behaviour of the lattice. The measurement setup for this is very similar to the setup used for the single unit cell and is shown in figure 14.3. As can be seen in the figure, wire constraints were added that allow the unit cell to move freely, but avoid the wires blocking the view of the tracking dots.

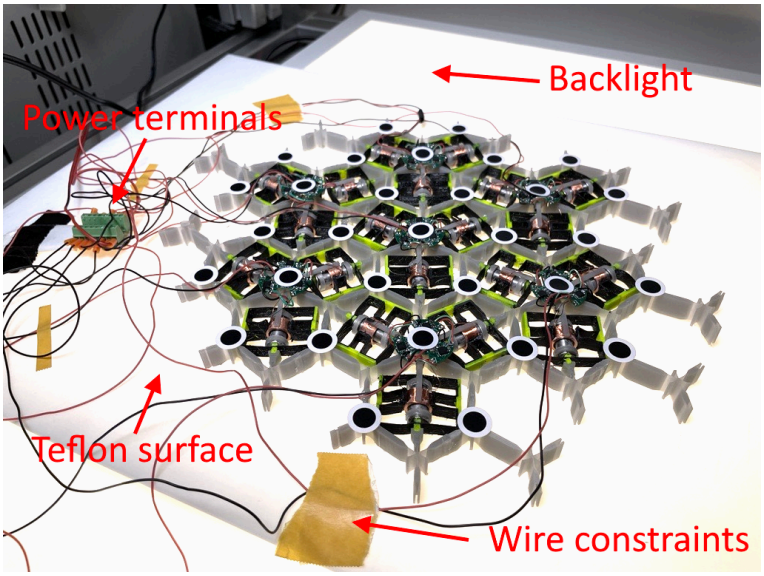

Figure 14.3: Experimental setup for the lattice.

Like with the previous experiments, the Basler aca640750um was used to capture the material response with a 480x640 pixel video at 500 frames per second. However, in order to fit the full lattice into the frame, the spatial resolution was reduced from $0.22\,mm/pixel$ to $0.47\,mm/pixel$, which is only 47% of the original accuracy. Additionally, a NIKON D780 was used to capture the response at 1920x1080 pixels and 120 frames per second. This allows for higher accuracy in position tracking, but now there are only 5 samples per limit cycle. This results in two videos with different qualities and their first frames are shown in figure 14.4.

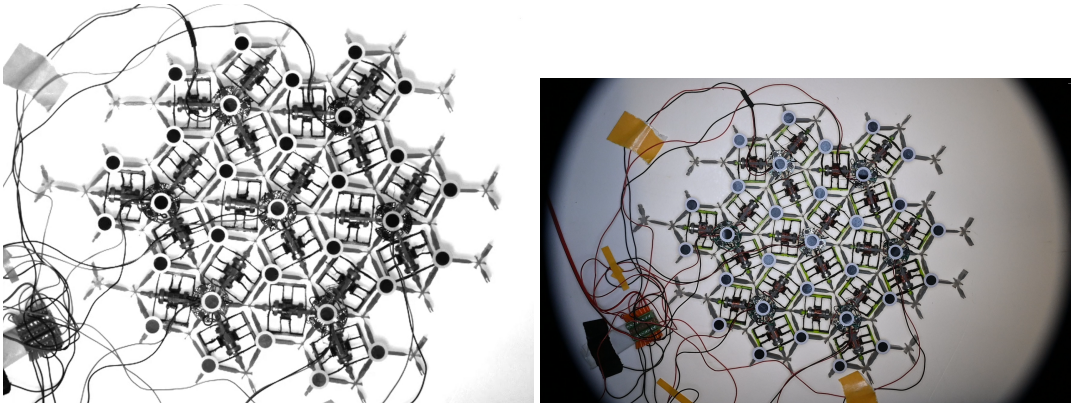

Figure 14.4: First frames from the Basler (Left) and the Nikon (Right) video's.

14.4. Results

As expected, the full lattice also has a clear perturbation point where with values below this perturbation, the dissipation is larger than the action and there will be no limit cycle. Where for the individual unit cell, there was a gradual increase in amplitude from a low gain towards the maximum amplitude at higher gains, this response is much more discrete for the lattice. Here, nothing happens until a gain of $K_a = 0.0286\,N/mm$, where a limit cycle occurs that is limited by the end stops of the actuators. Figure 14.5 shows that this difference in bifurcation is only different to the shape, but not the actual point of reaching maximum amplitude.

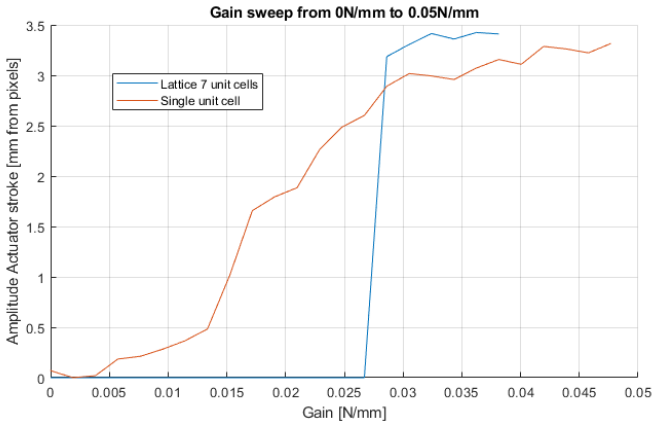

Figure 14.5: Limit cycle amplitudes for various gains comparing the single unit cell and lattice

While this is interesting, the most important thing is whether there is any form of synchronisation between the unit cells. From the video footage, it is immediately clear that the system showed a clear tendency to synchronise towards a single mode. Figure 14.6 Shows a still image from the experiment, where the colours show the position of the actuator; Compressed, in tension, or in their neutral position. Here, it is clear that apart from some imperfections the unit cells are synchronised in their limit cycle.

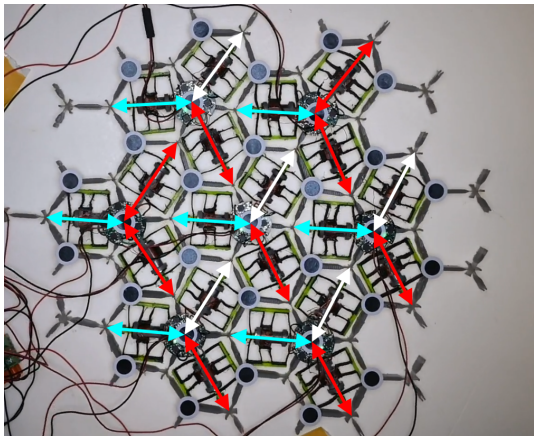

Figure 14.6: Image during the synchronised limit cycle with arrows showing the actuator lengths (red compressed, white neutral and blue expanded)

Also for the lattice, modes S1 and S2 can be expressed. However, in this case, they are expressed for each individual hexagon for both shear modes similar to the work from Brandenbourger et al. as shown in figure 3.3 [17]. Figure 14.7 shows how these modes are also synchronized where the colors are for $arg(S1 + iS2)$.

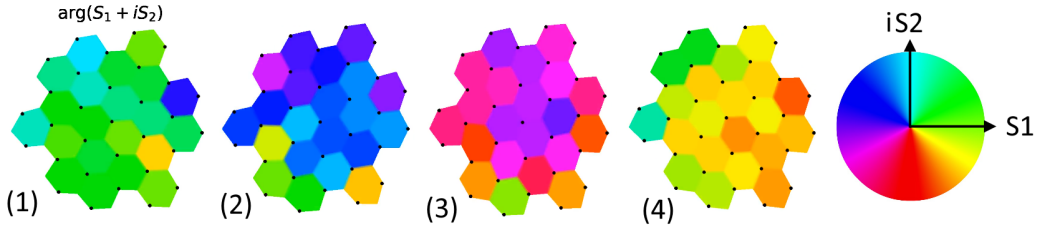

Figure 14.7: Limit cycle of the full lattice colored for the argument of S1 and S2.

The synchronisation of the lattice shows that there is a lower order mode than the eigenmode that exists in the single hexagon. A lower-order mode is preferred because the stiffness is lower and it will require less energy. As already shown in the simulations from Veenstra, these lower-order modes also exist for large lattices and here the frequency of them is significantly lower than the eigenfrequency of the individual unit cells. Also for the lattice in the experiment, the frequency decreases significantly for a synchronized system as shown in figure 14.8. Before synchronization, the dominant frequency is identical to the eigenfrequency of a single unit cell ($24\,Hz$), but once synchronized the frequency drops to $12\,Hz$.

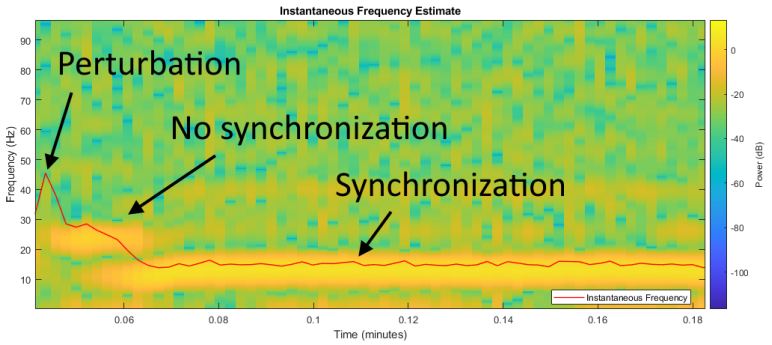

Figure 14.8: Power spectrogram and overlay the instantaneous frequency for the first setpoint of the gain sweep.

It is important to note that for this analysis, not each hexagon joint was tracked due to constraints with attaching the tracking dots. A lot of data interpolation was needed to calculate the positions of the missing joints which decreases the accuracy of the data analysis. For future research, there are many further things that could be analysed. A list of potential experiments is shown below:

- Repeat experiment with better time alignment of each PCB and correct tracking dots
- Measuring the robustness against imperfections by disabling actuators.
- Static deformation tests to measure the odd moduli K^0 and v^0.
- Other lattice shapes such as a line of unit cells
- Diluted unit cells with passive hexagons in between

15

Conclusion

By using local control and non-reciprocal couplings between actuators, an asymmetric elastic response is achieved. Due to the non-conservative nature of the coupling, the system has a tendency to cycle. A literature study, analysis of the system from Brandenbourger et al. [17] and simulations from Veenstra [19], [20] show that in large lattices of an odd elastic material these limit cycles synchronize towards lower-order mode shapes that could lead to autonomous locomotion by crawling or rolling in complex terrains.

A new unit cell was designed with the end goal of providing a new testing platform for lattices with a higher number of unit cells. The (active) unit cell consists of 3 hexagonal mechanisms with compliant joints, which are assembled from smaller passive unit cells in order to increase the modularity of the system. The hexagon has a size of $44\,mm$, stiffness of 73 N/m and a damping ratio of 0.1 However, due to the strongly non-linear viscoelastic material properties, the static stiffness is lower than intended ($46\,N/m$). In chapter 11, an alternative, more linear material is proposed which could increase the static stiffness and potentially decrease the damping ratio.

To achieve odd elasticity, energy conservation must be broken, which requires an actuator. By distributing linear actuators over multiple hexagons, a novel method that maximises the force to weight ratio Δ was used. While this method shows a lower potential odd ratio than [17] at $-\frac{sqrt(3)}{8}K_a$, a significantly higher odd modulus K^0 will be achieved due to the increased actuator force and stiffness of the system.

With its' large stroke, low friction and linear force response, a voice coil is the ideal actuator for an odd elastic metamaterial. The custom actuator uses a novel magnetic circuit with opposing magnets, to achieve a peak force of $0.32N$ in its full stroke range of 5.4. Compared to off-the-shelf actuators, the actuator is class-leading with its high force density ($75N/kg$) and low cost (9.32€). By using the magnetic circuit of the actuator, an integrated hall effect sensor is able to measure the position of the actuator with an accuracy of 0.122. Future improvements to the actuator design could be made to decrease the assembly time and complexity, allowing for faster production of lattices with a large number of unit cells.

Through acquired experimental data, the performance of the single unit cell was validated and characterized. At the Hopf bifurcation point of $K_a = 0.01\,N/m$, the ratio between driving and dissipating forces $|\xi| > 1$ and a limit cycle of finite-amplitude emerges. During this cycle with an amplitude of $5.4\,mm$ and a frequency of $24\,Hz$, the unit cell switches between modes S1 and S2. Consequently, the cycling between modes S1 and S2 was used to show that the single unit cell can locomote horizontally by hopping at a speed of up to $50\,mm/s$ in a direction decided by the sign of gain K_a.

To analyse how during the limit cycles all unit cells synchronise towards a single, lower-order mode a lattice of 7 unit cells was built. During the experiment, A cycle between shear modes S1 and S2 occurs for all hexagons with a synchronised phase. Additionally, the cycle frequency decreased from $24\,Hz$ for a disordered system to $12\,Hz$ for the synchronized system, which is expected for a lower order mode.

To conclude, by using a novel actuator design and engineering principles such as compliant mechanisms, a scalable unit cell design is achieved with a low cost, 10 times smaller scale per area and 15 times higher strength-to-weight ratio compared to the state-of-the-art. The performance of the lattice with 7 Unit cells (21 Hexagons) proves that the new design provides a platform that can be used to build lattices with many more unit cells. These lattices could autonomously locomote by crawling or rolling in complex terrain. Further understanding and development of this type of robotic material are still needed and a step towards 3D lattices could open up many opportunities for meta devices with odd elasticity.

References

[1] C. M. Soukoulis and M. Wegener, *Past achievements and future challenges in the development of three-dimensional photonic metamaterials*, Optics, Sep. 2011. DOI: 10.1038/nphoton.2011.154.

[2] S. A. Cummer, J. Christensen, and A. Alù, *Controlling sound with acoustic metamaterials*, Acoustics, Feb. 2016. DOI: 10.1038/natrevmats.2016.1.

[3] S. R. Sklan and B. Li, "Thermal metamaterials: Functions and prospects," 2018. [Online]. Available: https://academic.oup.com/nsr/article/5/2/138/4803969.

[4] J. B. Pendry, "Ci, 42.30.wb, 73.20.mf, 78," 2000.

[5] D. Chen and X. Zheng, "Multi-material additive manufacturing of metamaterials with giant, tailorable negative poisson's ratios," *Scientific Reports*, vol. 8, 1 Dec. 2018, ISSN: 20452322. DOI: 10.1038/s41598-018-26980-7.

[6] C. Scheibner, A. Souslov, D. Banerjee, P. Surówka, W. T. Irvine, and V. Vitelli, "Odd elasticity," *Nature Physics*, vol. 16, pp. 475–480, 4 Apr. 2020, ISSN: 17452481. DOI: 10.1038/s41567-020-0795-y.

[7] S. Ornes and s. Quanta Magazine moderates comments tonbsp;facilitate an informed, *A new theory for systems that defy newton's third law*, Nov. 2021. [Online]. Available: https://www.quantamagazine.org/a-new-theory-for-systems-that-defy-newtons-third-law-20211111/.

[8] R. J. Potton, "Reciprocity in optics," *Reports on Progress in Physics*, vol. 67, pp. 717–754, 5 May 2004, ISSN: 00344885. DOI: 10.1088/0034-4885/67/5/R03.

[9] Y. Hadad, J. C. Soric, and A. Alu, "Breaking temporal symmetries for emission and absorption," *Proceedings of the National Academy of Sciences of the United States of America*, vol. 113, pp. 3471–3475, 13 Mar. 2016, 15, interesting concept of allowing to absorb without the necessety of emitting or the other way around. The physical approach does not make sense for my research, ISSN: 10916490. DOI: 10.1073/pnas.1517363113.

[10] D. L. Sounas and A. Alù, *Non-reciprocal photonics based on time modulation*, 3, focussed on photonics, but is the source for a good explanation about reciprocity, Dec. 2017. DOI: 10.1038/s41566-017-0051-x.

[11] R. Fleury, D. Sounas, M. R. Haberman, and A. Alù, "Nonreciprocal acoustics new nonreciprocal acoustic devices put sound on a one-way street," 2015, pp. 14–21.

[12] Y. Wang, B. Yousefzadeh, H. Chen, H. Nassar, G. Huang, and C. Daraio, "Observation of nonreciprocal wave propagation in a dynamic phononic lattice," 2018, 17, Unidirectional wave guide that works with magnetic repelling/attracting properties that of a coil that can be controlled with a coil.

[13] M. Brandenbourger, X. Locsin, E. Lerner, and C. Coulais, "Non-reciprocal robotic metamaterials," *Nature Communications*, vol. 10, 1 Dec. 2019, ISSN: 20411723. DOI: 10.1038/s41467-019-12599-3.

[14] C. Coulais, D. Sounas, and A. Alù, "Static non-reciprocity in mechanical metamaterials," *Nature*, vol. 542, pp. 461–464, 7642 Feb. 2017, ISSN: 14764687. DOI: 10.1038/nature21044.

[15] L. M. Nash, D. Kleckner, A. Read, V. Vitelli, A. M. Turner, and W. T. Irvine, "Topological mechanics of gyroscopic metamaterials," *Proceedings of the National Academy of Sciences of the United States of America*, vol. 112, pp. 14 495–14 500, 47 Nov. 2015, 12, more focussed on non time-reversal symmetry and quite physics heavy. The main working method is the gyroscope/spring which is created with a motor sprinning a mass and magnets creating an attracting/repelling force between each gyroscope in a spring like (linear force/distance behaviour)., ISSN: 10916490. DOI: 10.1073/pnas.1507413112.

[16] S. P. Wallen, M. R. Haberman, Z. Lu, A. Norris, T. Wiest, and C. C. Seepersad, “Static and dynamic non-reciprocity in bi-linear structures,” vol. 34, Acoustical Society of America, 2018. DOI: 10.1121/2.0000861.

[17] M. Brandenbourger, C. Scheibner, J. Veenstra, V. Vitelli, and C. Coulais, “Active impact and locomotion in robotic matter with nonlinear work cycles,” Aug. 2021. [Online]. Available: http://arxiv.org/abs/2108.08837.

[18] B. Brubaker, *Wheel made of ‘odd matter’ spontaneously rolls uphill | quanta magazine*, Jun. 2022. [Online]. Available: https://www.quantamagazine.org/wheel-made-of-odd-matter-spontaneously-rolls-uphill-20220615/.

[19] J. Veenstra, “Trihex - 50x51 pattern fmax = 0.4551-ani,” unpublished, 2022.

[20] ——, “Rolling3 - g = 0.26666666666666666-ani,” unpublished, 2022.

[21] B. L, *Metamaterial world*, 2013.

[22] M. R., *A look at real-world metamaterial applications: A practioner’s viewpoint*, 2010.

[23] G. Yoon, I. Kim, and J. Rho, *Challenges in fabrication towards realization of practical metamaterials*, Sep. 2016. DOI: 10.1016/j.mee.2016.05.005.

[24] C. Coulais, *Robotic mechanical metamaterials*, Apr. 2020. [Online]. Available: https://wiki.uva.nl/amep/index.php/Robotic_Mechanical_Metamaterials.

[25] M. Z. Miskin, K. J. Dorsey, B. Bircan, Y. Han, D. A. Muller, P. L. McEuen, and I. Cohen, “Graphene-based bimorphs for micron-sized, tautonomous origami machines,” *Proceedings of the National Academy of Sciences of the United States of America*, vol. 115, pp. 466–470, 3 Jan. 2018, ISSN: 10916490. DOI: 10.1073/pnas.1712889115.

[26] S. Huber, *Mechanical metamaterials spring semester 2018*, 2018. [Online]. Available: http://www.cmt-qo.phys.ethz.ch.

[27] J. Bauer, A. Schroer, R. Schwaiger, and O. Kraft, “Approaching theoretical strength in glassy carbon nanolattices,” *Nature Materials*, vol. 15, pp. 438–443, 4 Apr. 2016, ISSN: 14764660. DOI: 10.1038/nmat4561.

[28] J. Bauer, L. R. Meza, T. A. Schaedler, R. Schwaiger, X. Zheng, and L. Valdevit, *Nanolattices: An emerging class of mechanical metamaterials*, Oct. 2017. DOI: 10.1002/adma.201701850.

[29] K. Dermitzakis, J. P. Carbajal, and J. H. Marden, “Scaling laws in robotics,” vol. 7, Elsevier B.V., 2011, pp. 250–252. DOI: 10.1016/j.procs.2011.09.038.

[30] V. Arakelian, “Gravity compensation in robotics,” *Advanced Robotics*, vol. 30, pp. 79–96, 2 Jan. 2016, ISSN: 15685535. DOI: 10.1080/01691864.2015.1090334.

[31] F. M. Morsch and J. L. Herder, “Design of a generic zero stiffness compliant joint,” vol. 2, 2010, pp. 427–435, ISBN: 9780791844106. DOI: 10.1115/DETC2010-28351.

[32] G. Baardink, “Equations for odd ratio v^0 for various unit cell concepts,” unpublished, 2022.

[33] K. Bertoldi, V. Vitelli, J. Christensen, and M. V. Hecke, *Flexible mechanical metamaterials*, Really nice overview of the types of metamaterials, Oct. 2017. DOI: 10.1038/natrevmats.2017.66.

[34] H. Wang, Y. Zhang, W. Lin, and Q. H. Qin, “A novel two-dimensional mechanical metamaterial with negative poisson’s ratio,” *Computational Materials Science*, vol. 171, Jan. 2020, ISSN: 09270256. DOI: 10.1016/j.commatsci.2019.109232.

[35] J. N. Grima and K. E. Evans, *Auxetic behavior from rotating squares*, 2000.

[36] M. K, *Method of packaging and deployment of large membranes in space*, 1985.

[37] M. Schenk and S. D. Guest, “Geometry of miura-folded metamaterials,” *Proceedings of the National Academy of Sciences of the United States of America*, vol. 110, pp. 3276–3281, 9 Feb. 2013, ISSN: 00278424. DOI: 10.1073/pnas.1217998110.

[38] Z. Li, Q. Yang, R. Fang, W. Chen, and H. Hao, “Origami metamaterial with two-stage programmable compressive strength under quasi-static loading,” *International Journal of Mechanical Sciences*, vol. 189, Jan. 2021, ISSN: 00207403. DOI: 10.1016/j.ijmecsci.2020.105987.

[39] Z. Song, X. Wang, C. Lv, Y. An, M. Liang, T. Ma, D. He, Y. J. Zheng, S. Q. Huang, H. Yu, and H. Jiang, "Kirigami-based stretchable lithium-ion batteries," *Scientific Reports*, vol. 5, Jun. 2015, ISSN: 20452322. DOI: 10.1038/srep10988.

[40] A. Rafsanjani and K. Bertoldi, "Buckling-induced kirigami," *Physical Review Letters*, vol. 118, 8 Feb. 2017, ISSN: 10797114. DOI: 10.1103/PhysRevLett.118.084301.

[41] D. M. Sussman, Y. Cho, T. Castle, X. Gong, E. Jung, S. Yang, and R. D. Kamien, "Algorithmic lattice kirigami: A route to pluripotent materials," *Proceedings of the National Academy of Sciences of the United States of America*, vol. 112, pp. 7449–7453, 24 Jun. 2015, ISSN: 10916490. DOI: 10.1073/pnas.1506048112.

[42] M. Pishvar and R. L. Harne, *Foundations for soft, smart matter by active mechanical metamaterials*, Start is very usefull, but it is very much focussed on SOFT and our material is not necessary soft, Sep. 2020. DOI: 10.1002/advs.202001384.

[43] L. Ionov, "Biomimetic hydrogel-based actuating systems," *Advanced Functional Materials*, vol. 23, pp. 4555–4570, 36 Sep. 2013, ISSN: 1616301X. DOI: 10.1002/adfm.201203692.

[44] M. Behl, K. Kratz, J. Zotzmann, U. Nöchel, and A. Lendlein, "Reversible bidirectional shape-memory polymers," *Advanced Materials*, vol. 25, pp. 4466–4469, 32 Aug. 2013, ISSN: 09359648. DOI: 10.1002/adma.201300880.

[45] W. L. Lee and H. Y. Low, "Geometry-and length scale-dependent deformation and recovery on micro-and nanopatterned shape memory polymer surfaces," *Scientific Reports*, vol. 6, Mar. 2016, ISSN: 20452322. DOI: 10.1038/srep23686.

[46] W. Anigbogu, H. Bardaweel, H. Bardaweel, and H. Bardaweel, "A metamaterial-inspired structure for simultaneous vibration attenuation and energy harvesting," *Shock and Vibration*, vol. 2020, 2020, ISSN: 10709622. DOI: 10.1155/2020/4063025.

[47] H. Liu, Q. Zhang, K. Zhang, G. Hu, and H. Duan, "Designing 3d digital metamaterial for elastic waves: From elastic wave polarizer to vibration control," *Advanced Science*, vol. 6, 16 Aug. 2019, ISSN: 21983844. DOI: 10.1002/advs.201900401.

[48] Q. Pan, S. T. Chen, F. F. Chen, and X. Y. Zhu, "Programmable soft bending actuators with auxetic metamaterials," *Science China Technological Sciences*, vol. 63, pp. 2518–2526, 12 Dec. 2020, ISSN: 1862281X. DOI: 10.1007/s11431-020-1741-2.

[49] C. Luo, Y. Song, C. Zhao, S. Thirumalai, I. Ladner, M. A. Cullinan, and J. B. Hopkins, "Design and fabrication of a three-dimensional meso-sized robotic metamaterial with actively controlled properties," *Materials Horizons*, vol. 7, pp. 229–235, 1 Jan. 2020, About a specific example of a 3D shape changing material that has a small chip on board that can control 6 different actuators, ISSN: 20516355. DOI: 10.1039/c9mh01368g.

[50] D. V. Isakov, Q. Lei, F. Castles, C. J. Stevens, C. R. Grovenor, and P. S. Grant, "3d printed anisotropic dielectric composite with meta-material features," *Materials and Design*, vol. 93, pp. 423–430, Mar. 2016, ISSN: 18734197. DOI: 10.1016/j.matdes.2015.12.176.

[51] H. Yang, S. Yang, X. Chi, and J. R. Evans, "Fine ceramic lattices prepared by extrusion freeforming," *Journal of Biomedical Materials Research - Part B Applied Biomaterials*, vol. 79, pp. 116–121, 1 Oct. 2006, ISSN: 00219304. DOI: 10.1002/jbm.b.30520.

[52] S. Kirihara, "Additive manufacturing of micro functional structures through diameter variable laser stereolithography and precursor sintering heat treatments," *Ceramic Transactions Series Additive Manufacturing and Strategic Technologies in Advanced Ceramics*, pp. 1–10, 2016. DOI: 10.1002/9781119236016.ch1.

[53] *Form 3: Industrial-quality desktop sla 3d printer*, Apr. 2022. [Online]. Available: https://formlabs.com/3d-printers/form-3/.

[54] K. S. Lee, R. H. Kim, D. Y. Yang, and S. H. Park, *Advances in 3d nano/microfabrication using two-photon initiated polymerization*, Jun. 2008. DOI: 10.1016/j.progpolymsci.2008.01.001.

[55] M. Askari, D. A. Hutchins, P. J. Thomas, L. Astolfi, R. L. Watson, M. Abdi, M. Ricci, S. Laureti, L. Nie, S. Freear, R. Wildman, C. Tuck, M. Clarke, E. Woods, and A. T. Clare, "Additive manufacturing of metamaterials: A review," *Additive Manufacturing*, vol. 36, Dec. 2020, ISSN: 22148604. DOI: 10.1016/j.addma.2020.101562.

[56] I. Fassi and D. Shipley, *Micro-Manufacturing Technologies and Their Applications*. Springer International Publishing, 2017. [Online]. Available: http://www.springer.com/series/11693.

[57] *Micro motor a-297-15*, Jun. 2022. [Online]. Available: https://www.budgetronics.eu/nl/motors/micro-motor/a-297-15.

[58] *Hk-5320 ultra-micro digital servo 1,7 g / 0.05sec / 0.075kg*, Jun. 2022. [Online]. Available: https://hobbyking.com/nl_nl/hk-5320-ultra-micro-digital-servo-1-7g-0-05sec-0-075kg.html.

[59] *Linear solenoids*, Jul. 2022. [Online]. Available: https://www.actronic-solutions.de/linear-solenoids.html.

[60] *Linear voice coil actuators*, Jun. 2022. [Online]. Available: https://www.thorlabs.com/newgrouppage9.cfm?objectgroup_id=14116.

[61] *Cedrat technologies, innovation in mechatronics*. [Online]. Available: https://www.cedrat-technologies.com/en/products/product/APA30uXS.html.

[62] H. Mcclintock, †. Fatma, Z. Temel, N. Doshi, J.-S. Koh, and R. J. Wood, "The millidelta: A high-bandwidth, high-precision, millimeter-scale delta robot," 2018. [Online]. Available: https://www.science.org.

[63] K. Jayaram, J. Shum, S. Castellanos, E. F. Helbling, and R. J. Wood, "Scaling down an insect-size microrobot, hamr-vi into hamr-jr; scaling down an insect-size microrobot, hamr-vi into hamr-jr," 2020. DOI: 10.0/Linux-x86_64.

[64] R. Legtenberg, A. W. Groeneveld, and M. Elwenspoek, "Comb-drive actuators for large displacements," 1996, pp. 320–329.

[65] *Jun 10 class: The dc motor and induction*, Jun. 2013. [Online]. Available: http://sph3u1-0.blogspot.com/2013/06/jun-10-class-dc-motor-and-induction.html.

[66] Bart, D. Nedelkovski, Anand, Dejan, Sabith, and M. Suyi, *How servo motor works amp; how to control servos using arduino*, Oct. 2021. [Online]. Available: https://howtomechatronics.com/how-it-works/how-servo-motors-work-how-to-control-servos-using-arduino/.

[67] *Transmission control solenoid: Working principle and function*, Oct. 2014. [Online]. Available: https://wheelzine.com/transmission-control-solenoid-working-principle-function.

[68] E. Moya-Lasheras and C. Sagues, "Run-to-run control with bayesian optimization for soft landing of short-stroke reluctance actuators," *IEEE/ASME Transactions on Mechatronics*, vol. 25, no. 6, pp. 2645–2656, Dec. 2020. DOI: 10.1109/tmech.2020.2987942. [Online]. Available: https://doi.org/10.1109/tmech.2020.2987942.

[69] D. Collins, *How do rotary voice coil actuators work?* Jun. 2022. [Online]. Available: https://www.motioncontroltips.com/how-do-rotary-voice-coil-actuators-work/.

[70] P. Zhang, "Sensors and actuators for industrial control," *Industrial Control Technology*, pp. 1–186, 2008. DOI: 10.1016/B978-081551571-5.50002-5.

[71] M. Bao, "Electrostatic actuation," *Analysis and Design Principles of MEMS Devices*, pp. 175–212, 2005. DOI: 10.1016/B978-044451616-9/50005-9.

[72] *Ss41 - hall effect sensor, position, digital, bipolar, ss40 series, sink output, 0.15 v out, 4.5 to 24 vdc*, Jun. 2022. [Online]. Available: https://nl.farnell.com/honeywell/ss41/sensor-hall-effect-sink-4-5-24v/dp/1470593.

[73] M. Ren, "Uc san diego uc san diego electronic theses and dissertations title a voice coil based vibration platform for micro robots application," 2019. [Online]. Available: https://escholarship.org/uc/item/7kf940mz.

[74] J. Jezný and M. Čurilla, "Position measurement with hall effect sensors," *American Journal of Mechanical Engineering*, vol. 1, pp. 231–235, 7 2013. DOI: 10.12691/ajme-1-7-16. [Online]. Available: http://pubs.sciepub.com/ajme/1/7/16.

[75] *Linear inductive encoder kit id1102l*, Jun. 2022. [Online]. Available: https://www.posic.com/EN/linear-encoder-id1102l.html.

[76] *Rlb miniature incremental magnetic encoder module*, Jun. 2022. [Online]. Available: https://www.rls.si/eng/rlb-linear-and-rotary-component-magnetic-encoder-system.

[77] *Essential electronics: Sensors, power, connectivity manufacturing solutions*, Dec. 2021. [Online]. Available: https://www.ttelectronics.com/products/categories/potentiometers/potentiometers/psm050s-05/.

[78] J. Gong, O. Seow, C. Honnet, J. Forman, and S. Mueller, "Metasense: Integrating sensing capabilities into mechanical metamaterial," Association for Computing Machinery, Inc, Oct. 2021, pp. 1063–1073, ISBN: 9781450386357. DOI: 10.1145/3472749.3474806.

[79] *Pca: Micro-measurements*, Jun. 2022. [Online]. Available: https://micro-measurements.com/pca/detail/060sl.

[80] M. S. Shewale, A. Razban, S. P. Deshmukh, S. S. Mulik, and H. B. Zambare, "Design and implementation of position estimator algorithm on voice coil motor," Institute of Electrical and Electronics Engineers Inc., Nov. 2018, ISBN: 9781538642733. DOI: 10.1109/I2CT.2018.8529546.

[81] H. Guckel, T. Earles, D. Zook, and T. Ohnstein, "Electromagnetic linear actuators with inductive position sensing," 1996, pp. 386–391.

[82] B. Hanson and M. Levesley, "Self-sensing applications for electromagnetic actuators," *Sensors and Actuators, A: Physical*, vol. 116, pp. 345–351, 2 Oct. 2004, ISSN: 09244247. DOI: 10.1016/j.sna.2004.05.003.

[83] S. Caldwell, *3.0 power*, Oct. 2021. [Online]. Available: https://www.nasa.gov/smallsat-institute/sst-soa/power.

[84] *5.0us : Micro indoor vliegtuig diy batterij 30mah 15c gewicht 0.84g: Parts amp; accessories: - aliexpress*. [Online]. Available: https://nl.aliexpress.com/item/1005001648889208.html?gatewayAdapt=glo2nld&spm=a2g0o.detail.0.0.ed395443Kycdmn&gps-id=pcDetailBottomMoreThisSeller&scm=1007.13339.169870.0&scm_id=1007.13339.169870.0&scm-url=1007.13339.169870.0&pvid=3e4ddccb-78ed-4137-ae6c-47e1703f7cef&_t=gps-id%5C%3ApcDetailBottomMoreThisSeller%5C%2Cscm-url%5C%3A1007.13339.169870.0%5C%2Cpvid%5C%3A3e4ddccb-78ed-4137-ae6c-47e1703f7cef%5C%2Ctpp_buckets%5C%3A668%5C%232846%5C%238116%5C%232002&pdp_ext_f=%5C%7B%5C%22sceneId%5C%22%5C%3A%5C%223339%5C%22%5C%2C%5C%22sku_id%5C%22%5C%3A%5C%2212000016975706578%5C%22%5C%7D.

[85] K. Breuer, "Flight of the robobee," *Nature*, vol. 570, pp. 448–449, 2019.

[86] Vattenfall, *Vermogen zonnepanelen/*, Apr. 2021. [Online]. Available: https://www.vattenfall.nl/kennis/vermogen-zonnepanelen/.

[87] N. Tolou, *Course slides: Compliant mechanisms, prbm*, Sep. 2019.

[88] B. Chakraborty and D. Ratna, *Viscoelasticity*, 2020. DOI: 10.1016/B978-0-12-819252-8.00003-3. [Online]. Available: https://linkinghub.elsevier.com/retrieve/pii/B9780128192528000033.

[89] *Vc063/m - voice coil actuator, 6.3 mm travel*, Jun. 2022. [Online]. Available: https://www.thorlabs.com/thorproduct.cfm?partnumber=VC063/M.

[90] *Non-comm dc voice coil linear actuator - ncc02-07-001-1rh*, Jun. 2022. [Online]. Available: https://www.h2wtech.com/product/voice-coil-actuators/NCC02-07-001-1RH.

[91] *Linear voice coil motor actuator lvcm-010-013-01*, Jun. 2022. [Online]. Available: https://www.moticont.com/lvcm-010-013-01.htm.

[92] F. Cigarini, S. Ito, S. Troppmair, and G. Schitter, *Comparative finite element analysis of a voice coil actuator and a hybrid reluctance actuator*, Mar. 2019. [Online]. Available: https://doi.org/10.1541/ieejjia.8.192.

[93] *Rr0060n*, Jun. 2022. [Online]. Available: https://supermagnetman.com/collections/neo-radial-rings/products/rr0060n.

[94] T. J. Teo, G. Yang, and I. M. Chen, “A flexure-based electromagnetic nanopositioning actuator with predictable and re-configurable open-loop positioning resolution,” *Precision Engineering*, vol. 40, pp. 249–260, Apr. 2015, ISSN: 01416359. DOI: 10.1016/j.precisioneng.2014.12.006.

[95] S. Awtar and A. H. Slocum, “Parasitic error-free symmetric diaphragm flexure, and a set of precision compliant mechanisms based it: Three and five dof flexible torque couplings, five dof motion stage, single dof linear/axial bearing. inventors,” 2006.

[96] A. B. MacKay, D. G. Smith, S. P. Magleby, B. D. Jensen, and L. L. Howell, “Metrics for evaluation and design of large-displacement linear-motion compliant mechanisms,” *Journal of Mechanical Design, Transactions of the ASME*, vol. 134, 1 2012, ISSN: 10500472. DOI: 10.1115/1.4004191.

[97] T. Instruments, *Drv5057 datasheet*, Nov. 2018. [Online]. Available: https://www.ti.com/lit/ds/symlink/drv5057.pdf.

[98] Formlabs, *Rigid 4000 material properties data*, Oct. 2020. [Online]. Available: https://formlabs-media.formlabs.com/datasheets/1801088-TDS-ENUS-0.pdf.

[99] Y. Kuznetsov, “Andronov-hopf bifurcation,” *Scholarpedia*, vol. 1, no. 10, p. 1858, 2006. DOI: 10.4249/scholarpedia.1858. [Online]. Available: https://doi.org/10.4249/scholarpedia.1858.

[100] S. Tatham, *Putty is an ssh and telnet client*, May 2022. [Online]. Available: https://www.putty.org/.

A

Actuator Calculations

For the actuator choice, an off-the-shelf example has been found and mentioned for each option, except for the Reluctance actuator. Because the Reluctance and Voice Coil Actuator are extra interesting respectively due to their high force density and constant force/stroke relation, a script has been written that calculates an actuator design of similar size. Values such as the field strength in the gap and the peak current in the coils are based on an assumption and therefore not accurate. However, where possible, the assumptions have been aligned between both concepts and therefore it should still provide an accurate comparison.

A.1. Voice Coil Actuator

Firstly, a Voice Coil Actuator is designed according to the following design:

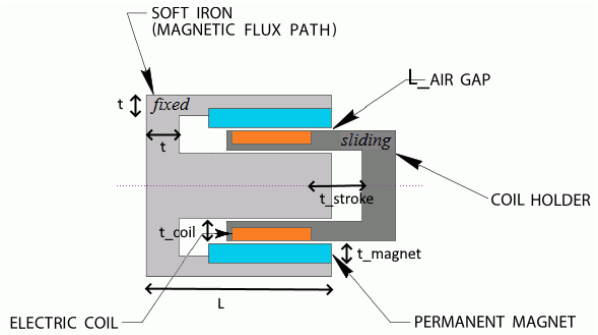

Figure A.1: Overview of working principle and the dimensions of the voice Coil Actuator.

The force in this actuator is calculated with the Lorentz force:

$$F = nIB_g l_w \tag{A.1}$$

Where n is the number of turns in the Coil, I is the current $[A]$ in Ampere, B_g is the magnetic flux $[T]$ in the air gap and l_w is the length of the conductor through the magnetic flux. The magnetic flux has been calculated with:

$$B_g = \frac{\lambda B_r}{\frac{A_g}{Am} + \frac{l_g}{lm}} \tag{A.2}$$

Where λ is a fringe factor of the field, estimated to be 0.75. B_r is the magnetic strength of the magnet, which is assumed to be 1.3 Tesla. A_g and A_m are the surface area's $[m^2]$ of respectively the air gap and the magnetic circuit and l_g and l_m are the lengths of the path through again respectively the air gap and the magnet.

The dimensions of the Actuator are calculated to meet the following requirements:

1. **Max voltage < 30V**, based on the coil resistance
2. **Actuator length 15 mm**
3. **Minimum stroke of 7 mm**
4. **Max current of 0.7 Ampere, through an AWG 43 wire**
5. **Flux density through the magnetic iron core < 0.8 Tesla**

If a planar coil design would be used, the delivered force would significantly decrease because part of the coil is not in the magnetic field, but still has a resistance.

A.2. Reluctance Actuator

For the Reluctance Actuator, a similar method is used, with the following layout:

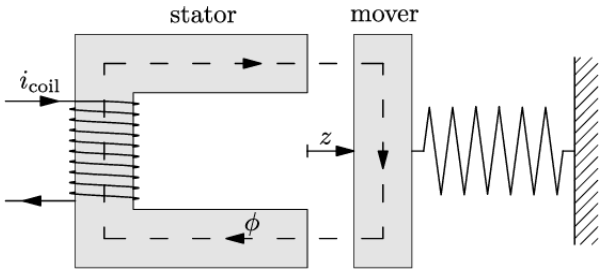

Figure A.2: Overview of working principle of the Reluctance Actuator [68]

In the design of an actual reluctance actuator, a spring that causes the mover to return to its natural position would not be necessary, due to the already existing passive stiffness of the unit cell. The force of this actuator can be calculated with:

$$F = \left(\frac{nI}{l_g}\right)^2 \frac{\mu_0 A_g}{4} \tag{A.3}$$

Where again n is the number of turns, A_g is the area m^2 of the air gap and I is the current $[A]$. lg is the gap $[m]$ between the mover and stator and $\mu_0 = 4\pi e - 7$ is the permeability of free space. Also for this actuator there was a set of requirements:

1. **Max voltage < 30V**, based on the coil resistance
2. **Actuator length 15 mm**
3. **Minimum stroke of 7 mm**
4. **Max current of 0.7 Ampere, through an AWG 43 wire**
5. **Flux density through the magnetic iron core < 0.8 Tesla**
6. **Volume of actuator equal to the Voice Coil Actuator**

A.3. Solenoid

For the solenoid, a more empirical approach was chosen and the values were based on an existing actuator from Actronic solutions [59]. This company has a list of available actuators and their data sheets. Specifically, the open frame solenoid RD-A420 was selected, due to its small body with a range of 7 mm. The values from the force vs stroke curve were taken from the datasheet and compared to the designed actuators. It is important to note that this solenoid is significantly bigger, but this could be due to being an off-the-shelf product, including mounting points etc. The electrical power usage is similar and therefore it was deemed a fair comparison.

B

Design Targets Calculator

As explained in chapter 3, there is a clear relation between the available maximum actuator force and the desired stiffness. For this, a model was written that uses the following inputs:

1. L_{unit}, Unit cell size $[mm]$
2. m, Mass $[g]$
3. u_{stroke}, Desired stroke $[mm]$
4. N_{Layers}, Number of vertically stacked hexagons $[-]$
5. $u_{collapse}$, Allowed deformation due to gravity $[mm]$

By using these parameters, it is possible to calculate the required stiffness to match the desired maximum deformation:

$$K_{lin} = \frac{(N_{Layers} - 1) * mg}{u_{collapse}} \tag{B.1}$$

Where it is assumed that the hexagon does not need to support its own weight. So if 5 layers are stacked, the lowest hexagon needs to support 4 layers. Then from this stiffness, it is now possible to calculate the required force from the actuator. This is a sum of the force needed to compensate for the gravity and the force needed to compress or stretch the spring to have the desired stroke:

$$F = (N_{Layers} - 1) * mg + K_{lin} * u_{stroke} \tag{B.2}$$

To now design the 6 individual flexures of the hexagon, it is necessary to convert the linear stiffness to angular stiffness. For this, the arm length is defined as $L_{arm} = L_{unit}/2$.

$$K_{rad} = \frac{K_{Lin} * L_{arm}^2 * sin(\frac{2*\pi}{3})}{6} \tag{B.3}$$

Whilst this is a good initial estimate, it should be noted that the angle of the hexagon is varying over the stroke of the actuator and therefore, this radial stiffness will vary over the stroke.

A full Simscape model was set up to validate these calculations and indeed the values closely resulted in the targeted amount of deformation due to gravity and full stroke.

C

Actuator FEM simulation

In order to simulate the magnetic field through the coil of the actuator, a 3D Comsol Multiphysics Simulation was set up. The first model was a simple magnetic circuit in a 2D, Axis-symmetric simulation with a magnetic core, A magnet, a Coil and a large volume of Air surrounding it all. The advantage of this simulation is that it is easy to set up, modify and finally, fast to solve. However, it lacks in simulating the magnetic field in 3-dimensional space, which proved crucial in the voice coil setup.

Therefore, a 3D simulation was created instead. For this simulation, the *Magnetic and Electric Fields* toolbox was used, which combines magnetic fields with electrical systems. This allows the user to for instance simulate electromagnets and in this case, it was used to simulate the effect of the electromagnetic field from the coil on the overall static magnetic field from the permanent magnets. Next to this, Comsol can directly calculate the expected force on a component due to the Lorentz force and this was a potential method for calculating the force of the actuator.

C.1. Model layout

Figure C.1 shows the 3D model that was used for the simulations, which is very similar to the 2D simulation by consisting of a magnet, a magnetic core, a coil and everything is placed into a large solid which represents the air space in which the magnetic field can be. The size of the surrounding air solid was decided through iteration as a compromise between simulation accuracy and solving time. The 3D model of the actuator was partially imported as a .Step file, but many components have been remodelled in Comsol to allow for parametric sweeps such as the thickness of the magnets.

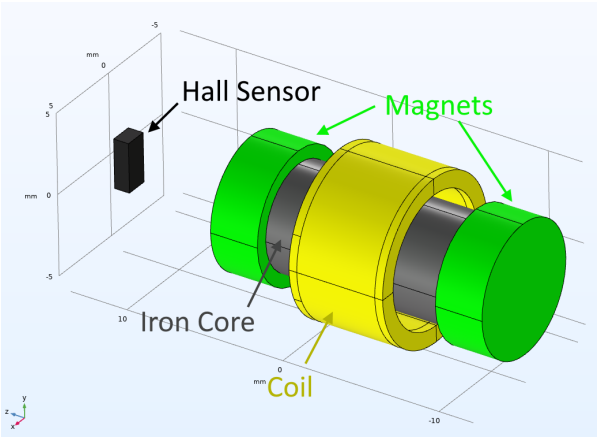

Figure C.1: Components of the 3D simulation. The solid that represents the air space around it is hidden for visibility.

C.2. Parameters

Next to parameters to define the size of the components, there are some other parameters as listed below. By using these parameters, it is possible to find the performance of the actuator in a certain operating window such as the stroke range, or the current through the coil. Next to that, it was used as a simple way to optimize the force density of the actuator.

- **T_Magnet**: The magnetization of the permanent magnets.
- **I_Coil**: Defining the maximum current through the coil
- **u_magnets**: A parameter that will move the magnet assembly (Magnets and core) relative to the coil and hall sensor, similar to how it moves in real life. This is used to simulate different positions over the stroke of the actuator.
- **mu_iron**: The relative permeability of the iron. For the final simulations, this constant permeability became redundant due to the introduction of the BH-Curve of the material allowing for magnetic saturation.
- **t_magnet**: The thickness of the magnet, to simulate various available magnets and compare the force density of the actuator.
- **D_core**: The outer diameter of the magnetic core. This was used to investigate the effect of a smaller inner core, to avoid friction between the core and the magnetic core.

The material properties for the soft iron are based on the datasheet that was provided by the supplier. Initially, a relative permeability for the core was used, to allow for fast iteration due to the fast solving. However, in an attempt to increase the accuracy of the simulation, the BH-Curve of the soft iron was taken from the material datasheet and used instead. This will allow for core saturation and help with estimating the minimum allowable thickness of the hollow magnetic core.

C.3. Visualization

After solving the simulation, there are some plot groups for showing a section view of the magnetic flow field. Section views were chosen since they give a good indication of the direction of the flow and for the final design, the flow is expected to be identical for each section view along the Z-axis of the mode. A combination of the flux density (For some normalized and for some a resultant of the density in each direction) and red streamline arrows to show the direction of the fieldlines were found to be the best way to visualize the magnetic field.

Next to plots, there are some boundary and domain probes to measure the following outputs:

- Magnetic flux orthogonal to the coil surface in multiple spots.
- Magnetic flux orthogonal to the hall sensor surface
- Calculated force on the coil due to the Lorentz force.

The calculated force from the coil was removed during the final simulations due to the fact that it gave some inconsistent and unexpected outcomes. Calculating the expected force with $F = N * I * B_g * L_w$ showed a better correlation to the measurement results and was therefore used instead.

Altogether, this 3D Simulation has proven to be an important and quite accurate tool to predict the performance of the actuator and the measurement of the Hall effect sensor. This made it possible to iterate the design and have a quantitative prediction of the effect of those changes on the final performance of the actuator. The model can be found on the research drive: `https://uva.data.surfsara.nl/index.php/s/d7OkNMRrlDXdU9m` Password: Actuator_Comsol123

D

Unit cell Multi-body analysis

To predict the behaviour of the unit cell, a model was created with Matlab Simscape Multibody. First, this model was used to simulate various methods of achieving odd elasticity in a single hexagon. Later, the model was expanded towards 3 hexagons to simulate the unit cell with divided actuation. Whilst hand-calculations are crucial in the design process, this multibody model was essential to simulate the dynamic behaviour which cannot be captured in simple calculations. As shown in chapter 12, the model correlates well with the behaviour of the unit cell in real life.

D.1. Model Setup

In order to simulate a multibody system, Simscape multibody allows the user to build up a system consisting of bodies (Rigid or even deforming) that can be coupled with Joints. These joints can have varying degrees of freedom and in the case of the unit cell rotational and translational joints are used. The distance between these joints is for this model defined with a *rigid transform*. Figure D.2 shows the layout of 3 hexagons that are coupled, 1 of these hexagons and finally the actuator.

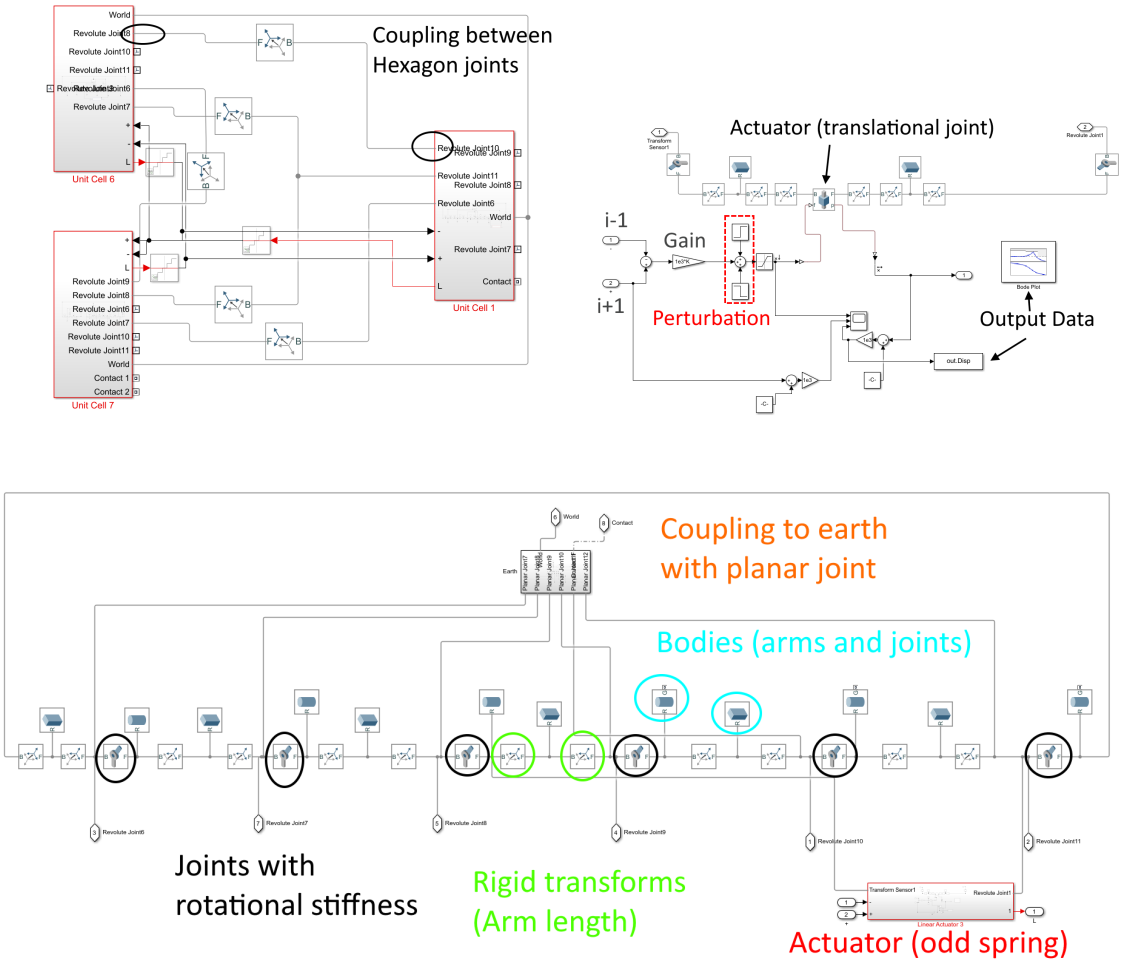

Figure D.1: The simulink model layout with first the overall layout, then the model of an actuator acting as odd spring and finally the overview of a single hexagon.

D.2. Model initialization

A Matlab script is used to call the Simulink model and define all parameters. This is done with a list of parameters such as the arm length and mass of each component. For the stiffness and damping coefficient of the system, an initial parameter is defined as well. However, to match these coefficients better with the actual measurement results, these values are iteratively tuned before running the actual simulation. For instance, for the stiffness, a while loop is used to measure the linear displacement for a set force, which is then compared to the required linear stiffness. If the stiffness is too low, the rotational stiffness of each joint is increased and the simulation is repeated. This cycle of simulation and changing the parameters is repeated until the target and result match up.

When all parameters are known, the actual simulation is done. Parameter sweeps can be done by simulating an array of parameters, of which the results can then be compared. For instance, the odd Gain can be swept from 0 to 1, with steps of 0.1 and the cycle amplitude can be compared after the simulations. The output of the model does not only consist of the arrays of data that are outputted to the Matlab workspace, but also of a video of the response of the system over time. Modes S1 and s2 during the limit cycle but then in the model are shown in figure **??**

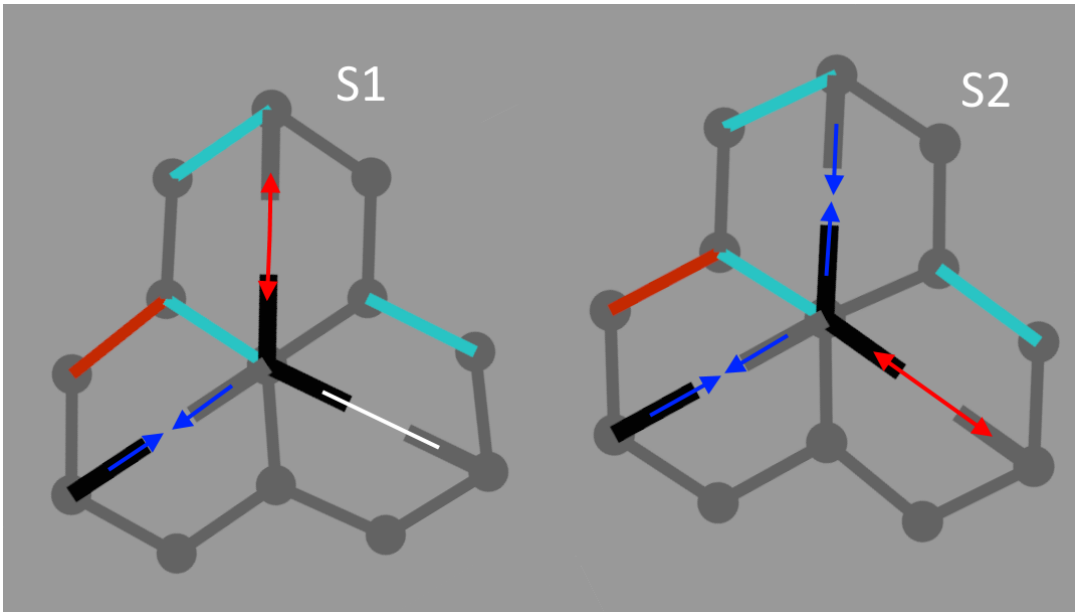

Figure D.2: Mode S1 and S2 in the simulink model. The red arrows mean that the actuator is in tension, blue is compression and white is in the neutral position.

The simulation can be found at `https://uva.data.surfsara.nl/index.php/s/jjCTzeXyparnQWI` with password: Actuator_Comsol123.

E

Video data analysis

After recording videos of the moving unit cell or the full lattice, a lot of post-processing is done, in order to finally calculate things such as the actuator length. For this process, there is the following workflow:

1. Record video in individual.Tiff images
2. Combine images into a single .mp4 file by using a custom Matlab FFmpeg toolbox
3. Load this .mp4 into a circle tracking software written by Jonas Veenstra. As shown in figure E.1, this script verifies the amount of dots to track for the first frame and after potential setting changes outputs the position of each dot as pixel positions over time.
4. Run the video data analysis script, which is explained in more detail below

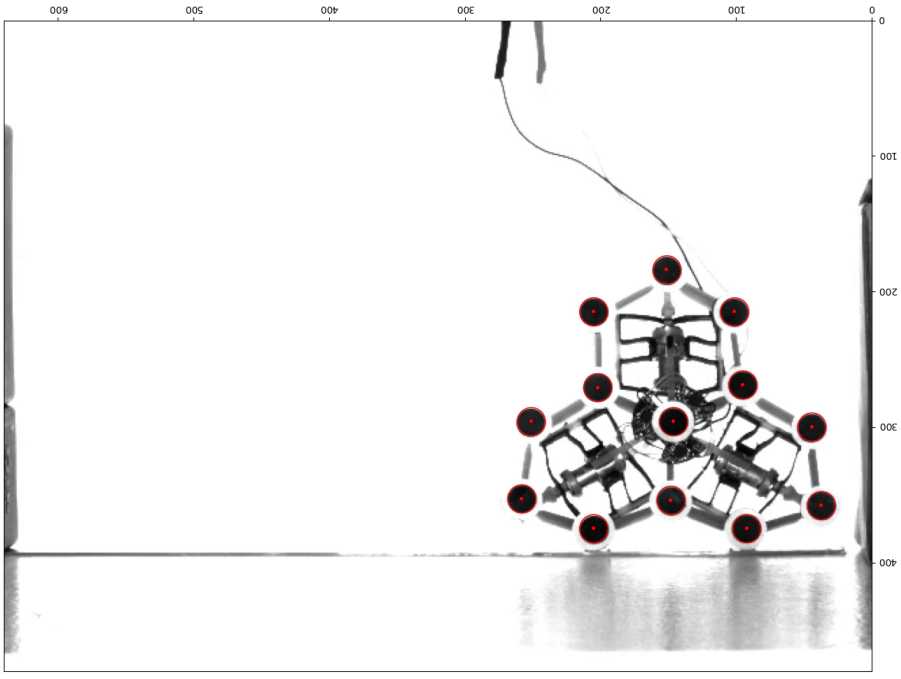

Figure E.1: First image of video's with the tracked dots highlighted.

E.1. Unit cell recognition

After collecting a dataset with the positions of a certain amount of dots over time, the first step is identifying how these dots combine into a unit cell. All distances are found by calculating the Euclidean distance between 2 points. The identification is done in the following order:

1. Find the centre, mid_Point, by finding the point closest to the average position
2. Find the 3 joints closest to the mid_Point, close_Link A, B and C. These points are easy to identify due to their direct connection to the midpoint, meaning that the distance is always close to the arm length of $22\,mm$. These 3 joints are all the start of a collection of points belonging to one of the 3 hexagons.
3. Next, for each close_Link, find the nearest 2 points (that are not the mid_Point,). These are the side_Links.
4. Finally, the side_Link with a clockwise rotation compared to the corresponding close_Link is selected. The point closest to this side_Link (where the close_Link is excluded) is the actuator_Link. The name indeed comes from the fact that the actuator is placed between this point and the mid_Point.

Figure E.2 shows a single frame with the identified dots and how they form a hexagon. This means that now we have everything to calculate things such as the actuator length, but also each angle of the hexagon.

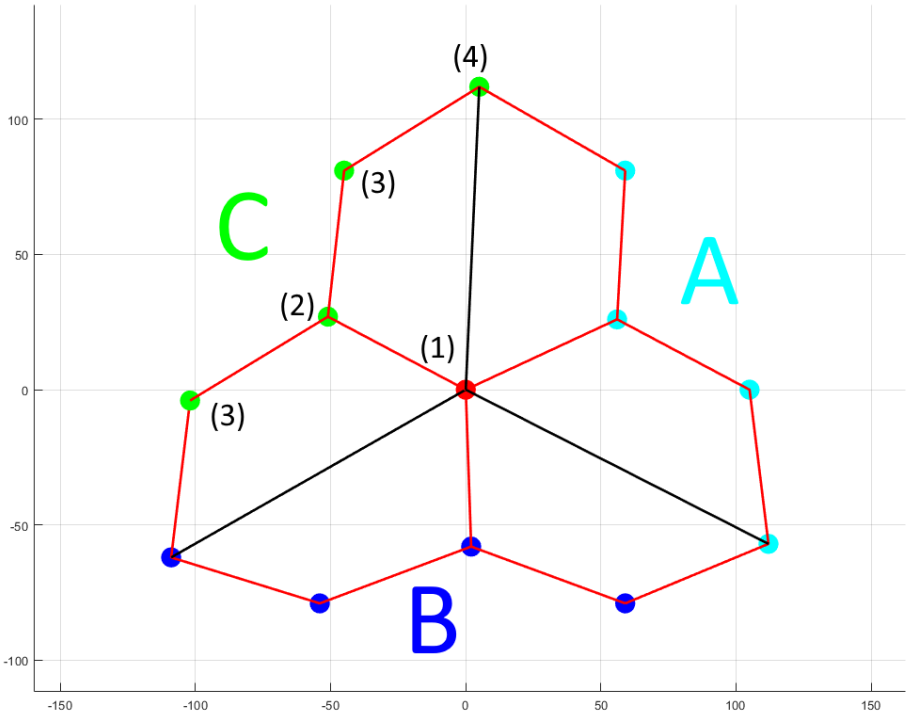

Figure E.2: First image of video's with the tracked dots highlighted. The numbers for side C Correspond to the steps in the identification.

E.2. Analysis

Now all positions are known, various things can be analysed. The script currently analyses the actuator length over time and even converts this to a δL which is corrected to be centred around 0. There is also a function that detects perturbations, to separate the response of the hexagon for each Gain sweep. By knowing the data sections for each gain and the actuator lengths, it is possible to calculate the values of modes S1, S2 and B. These modes are also visualized using scatter plots.

The full analysis script can be found at: `https://uva.data.surfsara.nl/index.php/s/HOxiUmNjrdjknsv` with password: Actuator_Comsol123.